Lava Tube System at Gunjale, Western Deccan Volcanic Province, India

A Thesis

submitted to

Indian Institute of Science Education and Research Pune in partial fulfilment of the requirements for the BS-MS Dual Degree Programme

by

Punya Pratyusha Sethi

Indian Institute of Science Education and Research Pune
Dr. Homi Bhabha Road,
Pashan, Pune 411008, INDIA.

October, 2024

Supervisor: Dr Raymond A. Duraiswami
Savitribai Phule Pune University

Certificate

This is to certify that this dissertation entitled Lava Tube System in Gunjale, Deccan Volcanic Province, India towards the partial fulfilment of the BS-MS dual degree programme at the Indian Institute of Science Education and Research, Pune represents study/work carried out by Punya Pratyusha Sethi at Savitribai Phule Pune University and Indian Institute of Science Education and Research under the supervision of Dr. Raymond A. Duraiswami, Professor, Department of Environmental Science, SPPU, during the academic year 2023-2024.

Dr. Raymond A. Duraiswami

Committee:

Dr. Raymond A. Duraiswami

Dr. Shreyas Managave

This Thesis is dedicated to everyone I have learnt to love.
(particularly Bakul and Weachy)
This Thesis is dedicated to everyone I will learn to love.

Declaration

I hereby declare that the matter embodied in the report entitled “Lava Tube System in Gunjale, Deccan Volcanic Province” are the results of the work carried out by me at the Department of Environmental Science, Savitribai Phule Pune University and Department of Earth Sciences, Indian Institute of Science Education & Research (IISER), Pune under the supervision of Dr. Raymond A. Duraiswami, and the same has not been submitted elsewhere for any other degree. Wherever others contribute, every effort is made to indicate this clearly, with due reference to the literature and acknowledgement of collaborative research and discussions.

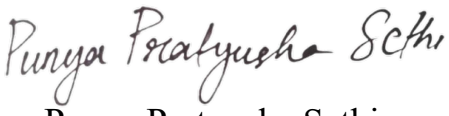

Punya Pratyusha Sethi

20191162

Table of Contents

Abstract 6

Acknowledgement 7

Chapter 1: Introduction 8
- 1.1 Preamble 8
- 1.2 Stratigraphy of the Basaltic Lavas 10
- 1.3 Tumulus Troubles 12
- 1.4 Lava Tubes 12
- 1.5 Objectives of the Present Study 14
- 1.6 Methodology 14
- 1.7 Study Area 15

Chapter 2: Materials and Methods 19
- 2.1 Field Mapping 19
- 2.2 Processing Preparation of Powders and Thin Sections 22
- 2.3 Microscopy 22
- 2.4 Modal Composition Measurement 22
- 2.5 XRF 22
- 2.6 EPMA 23

Chapter 3: Results and Discussion 24
- 3.1 Physical Volcanology and Structure of the Gunjale Lava Tube 24
- 3.2 Thin Section Analysis 25
- 3.3 Backscattered Electron Imagery 35
- 3.4 Mineral Chemistry 40
- 3.5 Temperature of Crystallisation 52
- 3.6 Whole Rock Geochemistry 53

Conclusions 57

References 60

Supplementary 66

List of Tables

Table 1: Geochemical stratigraphy in the western parts of the Deccan Traps 11
Table 2: Basaltic lava flow stratigraphy exposed in the area around Gunjale 17
Table 3: Descriptions and locations of the collected samples 21
Table 4: Modal percentage (%) of each minerals 35

List of Figures

Figure 1: Map of the Deccan Traps showing major tectonic zones 8
Figure 2: Schematic representation of previous proposed models for CFB architecture. 10
Figure 3: Graphic depicting stages in the formation of a lava tube 13
Figure 4: Google Earth Pro satellite image of the Gunjale area 16
Figure 5: Geological map of the Gunjale area showing the disposition of lava tube 18
Figure 6a, b, c: Sampling locations on the lava tube 20
Figure 7: Field photographs of the northern levee. 26
Figure 8: Field photographs of the dynamited section along the northern levee 27
Figure 9: Field photographs of the core of the lava tube 28
Figure 10: Field photographs of the right levee of the lava tube 29
Figure 11: Photomicrographs from the northern leeve 31
Figure 12: Photomicrographs from the southern leeve 32
Figure 13: Photomicrographs from the tube core. 33
Figure 14: Photomicrographs of cognates from the lava tube core 34
Figure 15: Backscattered Electron image of basalt from N. levee (GUN 1.1) 37
Figure 16: Backscattered Electron image of basalt from S. levee (GUN 6) 38
Figure 17: Backscattered Electron image of basalt from the core (GUN 2) 39
Figure 18: Backscattered Electron image of the cognates from core (GUN C1) 40
Figure 19: N. levee (GUN 1.1) plotted on the Hess's triangle for pyroxene 42
Figure 20: S. levee (GUN 6) plotted on the Hess's triangle for pyroxene 43
Figure 21: Core (GUN 2) plotted on the Hess's triangle for pyroxene 44
Figure 22: Cognate (GUN C1) plotted on the Hess's triangle for pyroxene 45
Figure 23: N. levee (GUN 1.1) plotted on plagioclase ternary diagram 47
Figure 24: S. Levee (GUN 6) plotted on the plagioclase ternary diagram 48
Figure 25: Core (GUN 2) plotted on plagioclase ternary diagram 49
Figure 26: Cognate (GUN C1) plotted on plagioclase ternary diagram 50
Figure 27: All samples plotted on a TiO_2-Fe_2O_3-FeO diagram for spinel and ilmenites 52
Figure 28: Total Alkali Silica diagram for samples across the tube 54
Figure 29: AFM diagram for samples across the tube 55
Figure 30: Trends of various major oxides versus Mg# for samples across the lava tube 56

Abstract

Lava tubes are common in pāhoehoe lavas and are important in understanding the emplacement of large volumes of lava, and their transportation over long distances in Continental Flood Basalt provinces of the world. The Deccan Volcanic Province is one of the largest continental flood basalt provinces in the world, with an aerial coverage of nearly 500,000 $km^{2.}$ Given the very large spatial distribution of lava flows over a relatively small timescale in the Deccan Traps, the sinuous structure at Gunjale, Ahmednagar (Ahilya Nagar), Maharashtra holds special interest regarding its genesis and role in the geology of the area. Following field work done in August 2022 at Gunjale, we discovered it is a lava tube hosted within compound pāhoehoe flows characterised by prominent levees formed by accreditation of breccias and lava lobes. We carried out petrography, modal composition measurements, XRF and EPMA to build a comprehensive emplacement and cooling history of the tube.

The northern levee is the preserved remnant of the lava flow composed of pāhoehoe sheets and lobes, and hence primarily microporphyritic. It displays highly oxidised characteristics suggesting subaerial emplacement and deuteric alteration. In contrast, the southern levee displays an accretion vesicular crust and breccia.The texture is exceptionally microporphyritic with large lanceolate opaque suggesting under cooling. The core of the tube consists of massive basalt and contains spherical to elongated plagioclase- clinopyroxene cognates. These cognates are extremely coarse grained, which implies they crystallised in a magma chamber elsewhere and then deposited via the magmatic plumbing system. Based on the clinopyroxene compositions, the northern levee record the primary emplacement temperatures of the lava tube and crystallisation at a higher temperature (800 to 1300 °C) compared to the southern levee (~500 to 1000 °C). The core underwent cooling induced fractional crystallisation and recorded a lower temperature (~700 to 1100 °C). The cognate also records similar temperatures of ~900 to 1100 °C suggesting a similar thermal regime as that of the core. The plagioclase compositions from the northern levee are more calcic and have higher temperature (~750 to 900 °C) in comparison to the southern levee (650 to 900 °C). The plagioclase from the lava tube core and cognate record significantly lower temperatures (650 to 750 °C). Magnetites form the core and cognates record a high temperature of 1500 to 1550 °C while the ilmenites form the core and cognates record slightly lower temperature of 1400 °C. It appears that the two leeve and the tube interior have different thermal regions and cooling histories.The tube formed initially as a preferred conduit within the lava flow field.

Keywords: Deccan Volcanic Province, Basalt, Lava tube, Levee, EPMA, XRF, Petrography, Cognate

Acknowledgements

I am indebted to my supervisor Dr Raymond Duraiswami for his immense patience as he has guided me through the project. I entered the field a nervous, inexperienced student, and I find myself now a slightly more experienced, still nervous student- and this would not have been possible without his push.

Immense gratitude is due to the Environmental Science Department, SPPU, Earth & Climate Sciences department, IISER Pune, and Geology Department, SPPU for letting me use the department resources as and when required. Thanks are due to Dr Shreyas Managave for his support. I am also grateful to Dr Gyana Ranjan Tripathy and Dr Neena Joseph Mani who have very kindly allowed me to complete this project on a staggered timeline. All the teachers I have met (professors or otherwise) on this 5 ½ year journey have, in one way or another, cemented my desire to remain ever curious about Nature and her wiles. I would like to thank faculty at Institut de Physique du Globe de Paris, particularly Dr Cyril Aubaud, Dr Helen Carton, and Dr Vincent Busigny who have been very understanding amidst this frenzy. I am also thankful for Bibliotheques Université Paris Cité.

Special thanks to Hemant Pednekar for his invaluable expertise during and after the field visit and EPMA, especially helping with the ternary diagrams. Thanks are due to Apoorva Chordia for helping me with the dissolution of samples and Aristle Monteiro for recording field data during the second field visit. A significant amount of work for this project was done at the National EPMA facility in the Department of Earth Science, Indian Institute of Technology, Bombay and I am grateful. I would also like to thank the support staff at both SPPU and IISER Pune for being the backbone of all research.

Standing on the shoulders of giants is an overused phrase in acknowledgments, but it has never been more true than for someone like me. I acknowledge the immense amount of luck that has led me to experience a life like this, and I can’t wait to explore more, learn more, and help more.

Bakul, Weachy, Triangle, Cookie and so many more have remained steadfast in both their friendship and dog-ness. I am thankful to my father for never saying no. I am indebted to my mother for keeping me hungry and ambitious. Finally, I am perpetually obliged to my best friend, Pallav, for reminding me I am human after all.

Chapter 1: Introduction

1.1 Preamble

The Deccan Volcanic Province is a prominent feature of the Indian subcontinent, covering an area of approximately 500,000 km^2 of Western and Central India in extensive basaltic lava flows about 65 million years ago (Jay and Widdowson, 2008; Schoene et al., 2019; Sprain et al., 2019). This volcanic province primarily consists of tholeiitic flood basalts, with an approximate volume of about 1,000,000 km^3 making it one of the largest flood basalts in the world, only superseded by the Ontong-Java plateau, North Atlantic Igneous Province, the Siberian traps, and Caribbean Large Igneous Province in terms of volume. Deccan volcanism primarily covered an area of possibly 1.5 million km^2 in the western, central, and southern Indian subcontinent peninsula (e.g., Krishnamurthy 2020, Kale et al., 2020), a large part is found submerged below the Arabian Sea and significant volume was lost due to rapid erosion and tectonic processes (Sheth et al., 2004). The DVP mainly spans most of Maharashtra and parts of Gujarat, Karnataka, Madhya Pradesh and Telangana (Fig.1).

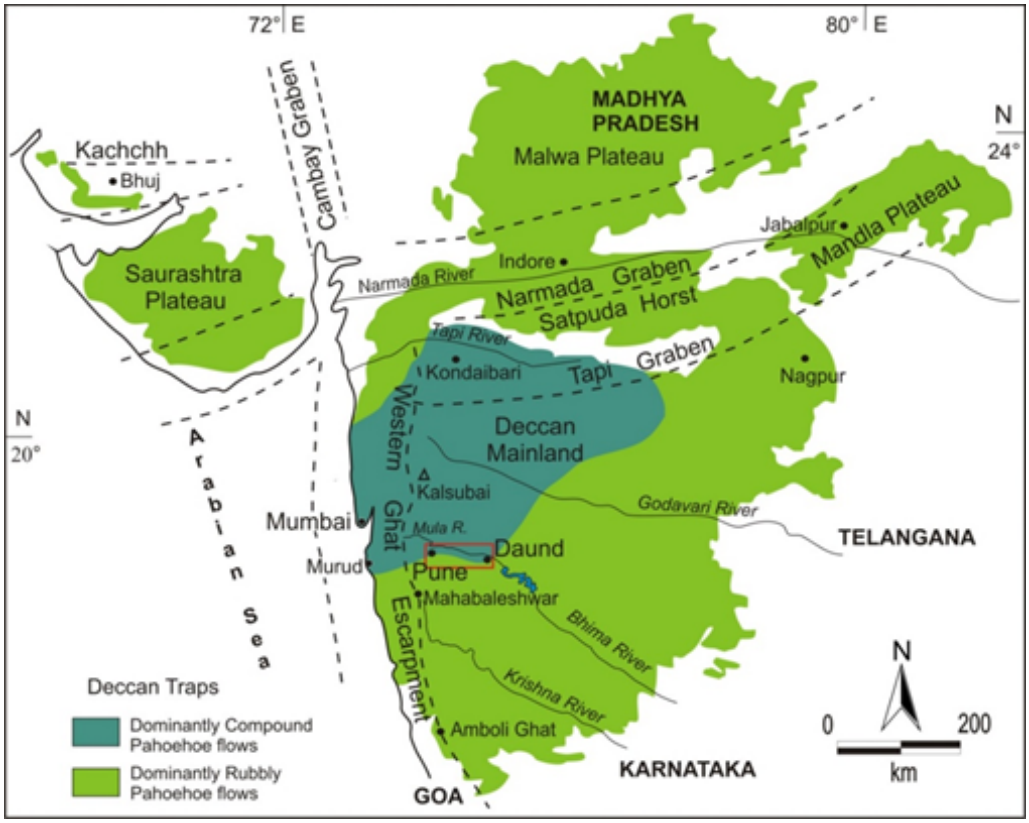

Fig. 1: Map of the Deccan Traps showing major tectonic zones (after Deshmukh, 1988, Gadpallu, 2021).

Emplacement of such large volumes of lava is also accompanied by degassing of volcanic gases such as CO_2 and S_2O during eruption. These gases led to a major impact on the atmosphere, and it could have potentially contributed to "volcanic winters" or a global climate change event that preceded the mass extinction at the Cretaceous-Paleogene boundary (Callegaro, 2023). This may have caused the extinction of dinosaurs, one of the most enduring scientific mysteries in popular culture. However, Sprain et al., 2019 posit that <90% of the deccan volume erupted in less than a million years, with nearly 75% being emplaced after the Cretaceous-Paleogene boundary. This rapid rate of emplacement implies a series of closely spaced volcanic eruptions that led to massive outpouring of lava across the region (Schoene et al., 2015).

The DVP formed about 65 Ma as the Indian plate over the Reunion hotspot (e.g., Cox and Hawkesworth; 1985, Beane et al., 1986; Courtillot et al., 1986; Morgan 1972). However, (Sheth, 2005) suggests a "passive" non-plume model, such as rifting and related mantle convection, for explaining the formation of Deccan Volcanic Province. The Deccan Traps are mainly tholeiitic basaltic lava flows and are stacked on top of each other- almost horizontal. Doleritic dykes intrude into the basaltic flows at several locations, which are speculated to represent feeder vents. Kachchh and Saurashtra also have some instances of alkaline and acidic intrusions.

Primitive Deccan magma may have been of picritic origin as a large plume formed under the subcontinent as a result of interaction with the Reunion hotspot. (Pakulla et al. 2020). Picritic magmas are characterised by high MgO content and are typically derived from deep mantle sources, associated with a significant amount of partial melting. Kumar et al. (2017) posit that Deccan picritic basalts were generated from 1–20% melting of the mantle whereas Sen (2001) proposes it to be 15-30% melting of a Fe-rich lherzolitic source at ~ 3-2 GPa. The rapid eruption rates may be influenced in part by the higher buoyancy and lower viscosity of picrite melts. These picritic magmas gradually evolved into tholeiitic compositions due to magmatic evolution.

Mittal et al. (2021) describe the magmatic architecture of the Deccan Traps as a complex magmatic plumbing system of dykes, sills, and layered intrusions by which hot material was efficiently transported to the surface and then emplaced by fissures (Fig. 2). They propose a system consisting of magma chambers of varying sizes at multiple depths, ranging from 5 - 15 km below the surface. These chambers allow for storage and evolution of magmas, which can lead to diverse compositions across the province. Although some work on the magma chambers and their plumbing systems (Vanderklusen, 2011; Saha et al., 2023; Ragini Kumari, 2024) have been done, meagre work has been done on the mode or conduits of of transport of the lavas that have travelled occasionally for more than 100 km (Bondre et al., 2004; Duraiswami et al., 2014). This study tries to address this gap in Deccan literature and tries to study and document the occurrence of a basaltic lava tube which is a potential transportation conduit (feeder?) for lavas in the region.

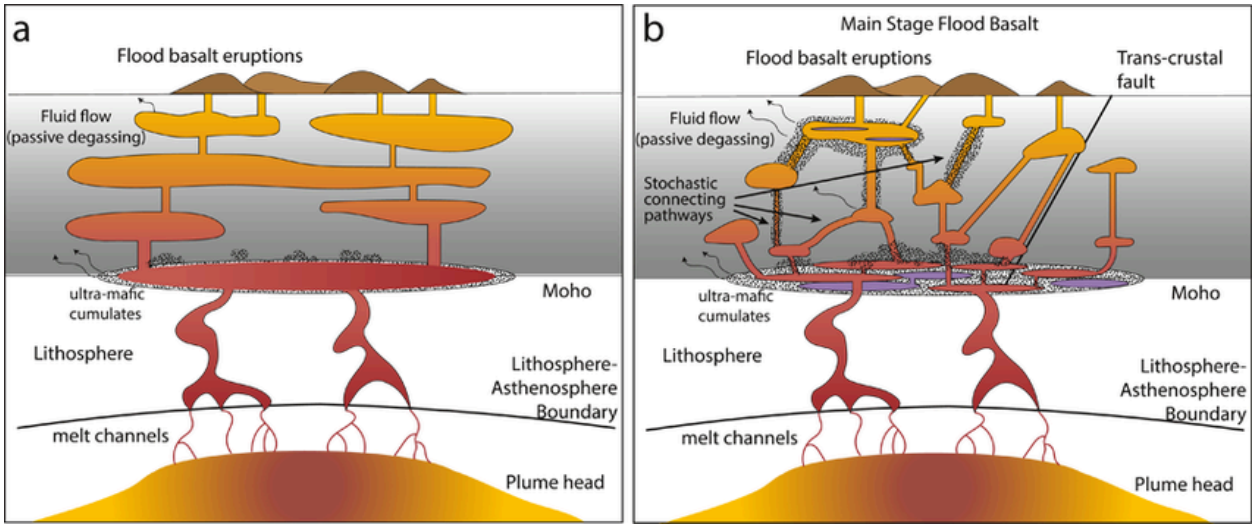

Fig. 2: Schematic representation of previous proposed models for CFB architecture. (Mittal et al ., 2021)

1.2 Stratigraphy of the basaltic lavas

Blanford (1867) and Krishnan (1960) initially attempted to classify the lava sequence into three units based on the presence or absence of intertrappean horizons and ash beds- subsequently named as the Lower, Middle and Upper Traps. Extensive mapping over 25 years by the Geological Survey of India resulted in the first published lithostratigraphic classification of the Western Ghats (Table 1.1, Godbole et. al., 1996). Cox and Hawkesworth (1985) and subsequently by Beane et al. (1986) and Subbarao and Hooper (1988) created the chemostratigraphic stratigraphy. Based on the scheme of classification the entire Western Ghats is divided into lower Kalsubai Subgroup (5 Formations), middle Lonavala Subgroup (2 Formations), and upper Wai Subgroup (5 Formations (Table 1). The Pune - Karad area exposes lavas belonging to the Bushe Formation (Lonavala Subgroup), Poladpur and Ambenali Formations (Wai Subgroup).

Lava flows are divided into ‘compound’ and ‘simple’ flows based on their morphology/geometry. At the outcrop scale, pāhoehoe lava flows in the DVP are commonly compound, while a'ā and transitional lava flows are simple. Usually, the thickness of individual a'ā lava flows range from 2 to 15 m, pāhoehoe ranges from 2 – 20 m and rubbly pāhoehoe varies from 10–80 m. The latter’s increased thickness may be higher due to endogenous lava transfer and inflation, which will be applicable later. The internal structure of a simple rubbly pāhoehoe lava flows consist of a vesicular crust with flow-top breccia; a thick, non-vesiculated, dense (but jointed) core and a sharp glassy base (Duraiswami et al., 2008, 2017).Simple a'ā lava flows in the Deccan Traps are dominated by core, with jointing, and bracketed by upper and lower breccia layers. Interflow horizons or red boles are common in simple lava flows and sometimes compound pāhoehoe flows.

Table 1: Geochemical stratigraphy in the western parts of the Deccan Traps (after Beane et al., 1986, Gadpallu, 2021). N - normal magnetic polarity, R- reverse magnetic polarity. GPB-Giant Phenocryst Basalt. Age based on U-Pb ages, Schoene et al., (2014[1]; 2019[2]) and $Ar^{39}/^{40}$ data from Renne et al., (2015[3]); Sprain et al., (2019[4]).

Group	Sub-group	Formation	Thickness (m)	Magnetic Polarity	Age (Ma)
D	Wai	**Desur**	~ 100	N	
E		Panhala	>175	N	
C		Mahabaleshwar	280	N	65.552± 0.026[1]
C					66.521± 0.065[4]
A					65.6-65.8[2]
N			*Purandhar GPB*		
		Ambenali	500	R	65.968 ± 0.248[3]
					65.9-65.8[2]
		Poladpur	375	R	66.1-66.0[2]
B					66.940± 0.092[4]
A		---	---	---	---
	Lonavala	Bushe	325	R	66.09-66.14[2]
S					66.059 ± 0.079[4]
A		Khandala	40	R	66.105 ± 0.102[4]
L		---	---	---	---
			Giravali GPB		
T	Kalsubai	Bhimashankar	40	R	66.208 ± 0.067[3]
					66.171± 0.076[4]
					66.3-66.15[2]
			Manchar GPB		
		Thakurwadi	650	R	66.199 ± 0.129[3]
					66.22 [2]
			Tunnel 5 GPB		
		Neral	100	R	66.28 ± 0.05[3]
					66.218 ± 0.036[4]
			Kashele GPB		

Group	Sub-group	Formation	Thickness (m)	Magnetic Polarity	Age (Ma)
		Igatpuri	700	R	66.347 ± 0.072[3]
			Thalghat GPB		
		Jawhar		R	66.381 ± 0.050[3]
					66.413 ± 0.067[4]
					66.29[2]

			Base not exposed		

1.3 Tumulus Troubles

Tumuli can be confused with tubes as in several places worldwide tumuli are generally aligned parallel to oblique to the tube axis. (Glaze et al., 2005; Duraiswami et al., 2001). Morphologically, both tumuli and tubes display bulging structures and cracked tops. Tumulis are typically formed when lava flows inflate due to build up of gases beneath a solidified crust, which causes it to bulge. They form when molten material stagnates, the extended time period contributing to the accumulation of pressurised gas, so they are often associated with the terminuses of long range lava tubes and complex pāhoehoe flows. The cracks and fissures on tumuli surfaces are formed due to gas escaping. On the other hand, collapsed lava tubes can have a cracked/craggly surface due to a collapsed roof, which can be differentiated from tumuli by the presence of rubble in the vicinity. Tubes are typically more elongated than tumuli as well. Tumulus are also likely to exhibit more dense vesicular textures than tubes due to the different processes of formation.

1.4 Lava tubes

Lava tubes are naturally forming tunnels or conduits when lava flows under a solidified surface. The tubes can be small with widths of few metres to massive tunnels that are several kilometres in length. Common examples include Hawaaii, and these are also found on the Moon (e.g. Hurwitz et al., 2013; Sisolekar et al., 2021).

The process of formation is similar to a lava cave, which are usually found in basaltic territory due to the low viscosity. Tubes are commonly found in pāhoehoe flows, as it is more fluid than a'ā and blocky flows. The surface of the lava tube is cooled when exposed to air. The tunnel walls are efficient insulators, hence the material beneath it can stay molten. These tubes thus can carry melt over long distances, sometimes resulting in the formation of extensive systems. When material is no longer being pushed out due to rapid volcanism at source due to depletion or

diversion, it slows and cools in the tunnel. This filling is much younger than the walls, and its age and varying geochemistry is a sure fire way of verifying that the structure is a lava tube.

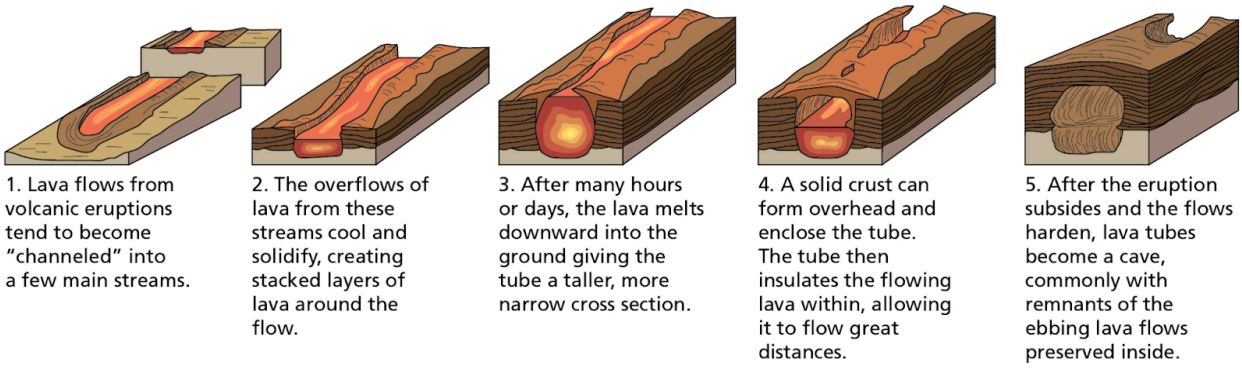

Fig. 3: Graphic depicting stages in the formation of a lava tube by Trista Thornberry-Ehrlich (Colorado State University) after USGS graphic by Bruce Rogers [25]

Lava tubes are easier to identify when they present as hollow tubes with cave-like entrances, however it is common for the last pulse of lava to fill the tube, or the tube collapsing in on itself. We can identify these structures by looking for morphologies associated with the intact tube such as remnants of tube walls with flow patterns and rubble from the roof collapse. Secondary associated features may include the ropy texture of the pāhoehoe lava and the shape of the system. However, tectonic processes, vegetation growth, sedimentation and/or erosion can make it harder to definitively identify by eye alone and we have to depend on geophysics and geochemistry to confirm our findings as well as glean more information on the depositional environment.

Lava tubes are found both in modern and ancient lavas and thus provide an opportunity to understand their genesis and role in the emplacement of these flows. Considering that tubes are known to provide an insulated and efficient mode of lava transport, they directly influence the aspect ratio (length: width) and emplacement dynamics of flows. It is believed that long lava flows (>r than 100 km long are essentially tube-fed (Keszthelyi and Self, 1998).

Considering the DVP is one of the largest volcanic regions in the world, in terms of both area covered and the high volume of lavas emplaced, methods of melting and transport are important factors to consider in the geology of the region. Lava tubes are conduits that form when the surface is chilled but the hot core continues to have movement of melt, and it can facilitate the efficient movement and dispersal of low viscosity basaltic lava over large distances. Features observed in lava tubes let us describe the behaviour of the flow (such as viscosity), emplacement and cooling history. They can be identified by their linear (sometimes branching) structures on a relatively undulating volcanic landscape.However, it is easy to confuse them with tumulus (as discussed in section 1.3), so we need to investigate further- Ground Penetrating Radar (GPR) and

Interferometric Synthetic Aperture Radar (InSAR) are more effective in mapping such subterranean structures .

In the western parts of the DVP a number of structures have been identified as lava tubes/channels (Thorat 1996; Sharma and Vaddadi 1996). Misra (2002) has described the tubes in relation to the regional setup, although a few structures identified by him as tubes/channels are probably cryptic lava flows (see Dole et al 2002, Duraiswami et al, 2005). A review of existing literature reveals a complete misunderstanding of the exact nature of these structures i.e., they have been vaguely described as lava tubes or channels without understanding the implication of usage of such terms.

Lava tubes were identified by Duraiswami et al., (2004), Pawar et al., (2016) and Sen et al. (2011). The identified systems were in hummocky and sheet lava flow dominated terrain. wherein the pāhoehoe is characterised by its smooth, undulating surfaces with ropy textures and are caused by low effusion rates and irregular topography. The present study focuses on the Gunjale lava tube previously studied by (Thorat, 1996), Sharma and Vaddadi (1996) and Misra (2002). We describe the same tube in light of modern physical volcanology using better investigation techniques in light of the fact that there is only a preliminary lava flow map island field description in these studies without detailed petrography, mineral chemistry, whole rock geochemistry, etc. We try to bridge this gap and present the results of our findings in this thesis.

1.5 Objectives of the present study

The following objectives were set before the commencement of the study:

1. To undertake lava flow mapping in the Gunjale area and mark the extent of the lava tube.
2. To observe and describe the physical volcanology of the lava tube in terms of modern volcanological terms.
3. To select a representative traverse across the lava tube and sample it in detail considering the textural and mineralogical variations across the tube.
4. To undertake a systematic and detailed petrographic, modal and geochemical characterisation of the tube samples so as to ascertain their true petrochemical identity.
5. To constrain and discuss the emplacement of the lava tube.

1.6 Methodology

The methodology to be adopted during the course of this study is organised into the following:

Library work: Literature survey on the geological aspects of the study area was undertaken. Published papers were collected from Savitribai Phule Pune University, other University libraries, Indian Institute of Technology (Powai), Mumbai, Geological Survey of India, Pune etc. Relevant literature on lava tubes was downloaded from the Internet.

Field work, geological mapping and sampling: The geological mapping and sampling was undertaken in the field. All samples collected for the laboratory were carefully labelled and brought to the laboratory for further analyses. A total of 20 kg of samples from representative parts of the channel levee, core, etc were collected.

Laboratory studies: This included digitisation and preparation of base maps and transfer of lava flow boundaries geological maps. Detailed textural studies, mineralogy and petrography was undertaken. Electron microprobe analyses (EPMA) of individual minerals like clinopyroxenes, plagioclase and opaques from representative samples were completed. Samples were also powdered and subjected to geochemical analyses i.e. major oxide by X-ray fluorescence (XRF) method. The detailed methodology and standards used are described in detail in the 'Methods and material' section.

Synthesis of the data, thesis writing and submission: The data generated during the field and in the laboratory during this study is synthesised, interpreted and presented in this section.

1.7 Study Area

This study focuses on a discontinuous, sinuous channel-like structure observed at Gunjale (Fig. 4), Ahmednagar District (Ahilya Nagar), Maharashtra, from the upland western Deccan Volcanic Province. The tube system is located in the Ahmednagar district of Maharashtra, India, located about 200 km East from Mumbai. The temperature of the region reaches a maximum of 33°C and minimum of 18.5°C with annual average rainfall being 583.5 mm (GSDA, Govt. of Maharashtra). The area is grassland type and is dominated by farmland with some small settlements in the region. The GroundWater Surveys and Development Agency, Government of Maharashtra, notes that the trap rock in the district is distinctively stratified, with beds of basalts and amygdaloidal basalts being parallel. The lava flows are generally horizontal but local geomorphology preserves gentle tilting and minute undulations. There are records of recent intrusive basic dykes, associated with intertrappean beds, red boles, and volcanic/pyroclastic material (GSDA, Govt. of Maharashtra).

We used both field techniques and laboratory analysis to explain the eroded structure and its surrounding compound pāhoehoe lava flow. As mentioned earlier, there is limited geological investigation in the region. We undertook detailed flow mapping in the region by taking suitable traverses along the Vambori and other ghat sections. The contact between different lava flows were identified based on presence of chilled margin, pipe vesicles or presence of thin red bole in the field and their GPS coordinates were noted. These were transferred to the 'Window of interest' where the 20 m contours were digitised and transferred from the Survey of India toposheet (47 I/15). Based on these, the lava flow contacts were extrapolated along the contour lines to produce the geological map (Fig. 5). The traces of the segments of the lava tube were also identified and transferred on the geological map. The stratigraphy of the basaltic lava flow exposed in the area around Gunjale, western Deccan Volcanic province is given in Table 2.

About 6 distinct lava flows are exposed in the area around Gunjale. They vary in thickness from 17 to greater than 34 m. Lava flow F1 to F4 consists of thick hummocky pāhoehoe and thick sheet lobes. A distinct compound giant phenocryst basalt which is equivalent to the *Manchar GPB* of the Kalsubai Group (See Table 1) is exposed in the region. This acts as a stratigraphic marker horizon in the region. The lava tube at Gunjale appears to be emplaced within the lava flow F1.

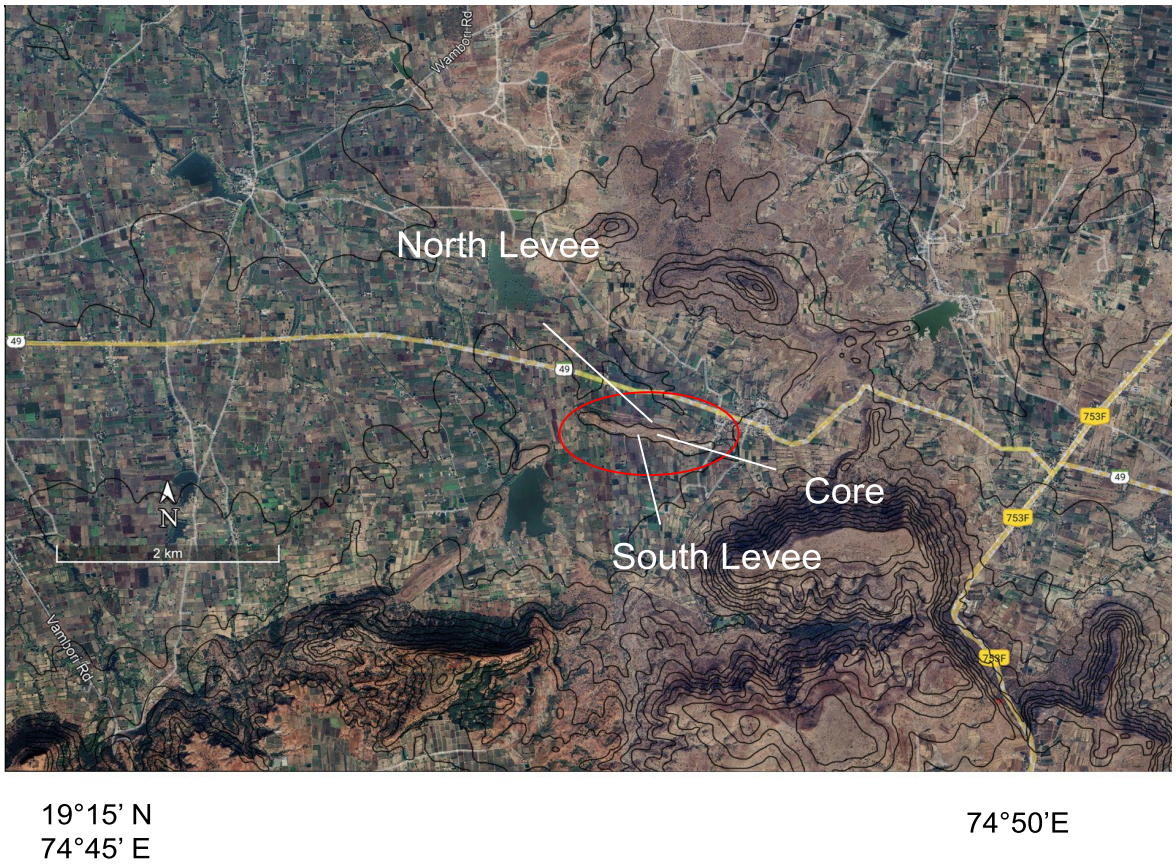

Fig. 4: Google Earth Pro satellite image of the Gunjale area. Red ellipse denotes the segment of the tube sampled.

The lava tube (Fig. 5, marked as red dashed line) we are focusing on is an exposed stretch of a possibly longer tube or conduit system that supplied lava to the region. The tube is aligned nearly East - West spanning nearly 1300 m from 19°16'49.71"N 74°47'40.98"E to 19°16'41.52"N 79°48'23.13"E. It is about 200 m at its widest point and 75m at its narrowest, with height varying 0.5 to 5 m above ground level. We approached the tube from the northwest, and began with a transit across the Northern Levee. Then we diagonally cut across the centre of the structure, henceforth referred to as the core, sampling as we went. Then we moved towards and along the Southern Levee. We also observed and collected the cognate samples in the core towards the east end of the tube studied tube segment.

Table 2: Basaltic lava flow stratigraphy exposed in the area around Gunjale, western Deccan Volcanic province

Sr. No.	Elevation (m amsl)	Thickness (m)	Description
1	< 616	2 to 3	Quaternary alluvium and Recent top soil overlying lava flow F1 which is a highly oxidised compound pāhoehoe with plagioclase micro phenocrysts. The toes and lobes show smooth or ropy surfaces. Thicker sheet lobes show distinct crust-core and pipe-bearing basalt vesicular zones with segregation features like vesicle cylinders and segregation sheets.The Gunjale lava tube occurs as segmented remnant within this lava flow.
2	648	32	F2- Compound pāhoehoe with numerous toes and lobes
3	665	17	F3- Lava with highly oxidised, vesicular sheets and lobes. A large lava tube is exposed within this lava.
4	686	21	F4- Thick sheet pāhoehoe lava with mega plagioclase phenocrysts of up to 7 cm long. The sheet is divided internally into ~ 2.6 m vesicular crust with vesicle banding and domed shaped vesicles at the base. The core is thick and plagioclase phyric. This lava flow is equivalent to the Manchar GPB (Giant Phenocryst Basalt) exposed in the Western Ghats, about 70 km to the west of the study area.
5	710	24	F5- Thick compound pāhoehoe with numerous P-type pāhoehoe lobes.
6	>710	2 to 5	F6 and lava flows above- Partly exposed lava flow F5 that occurs as core stones and boulders on the plateau areas

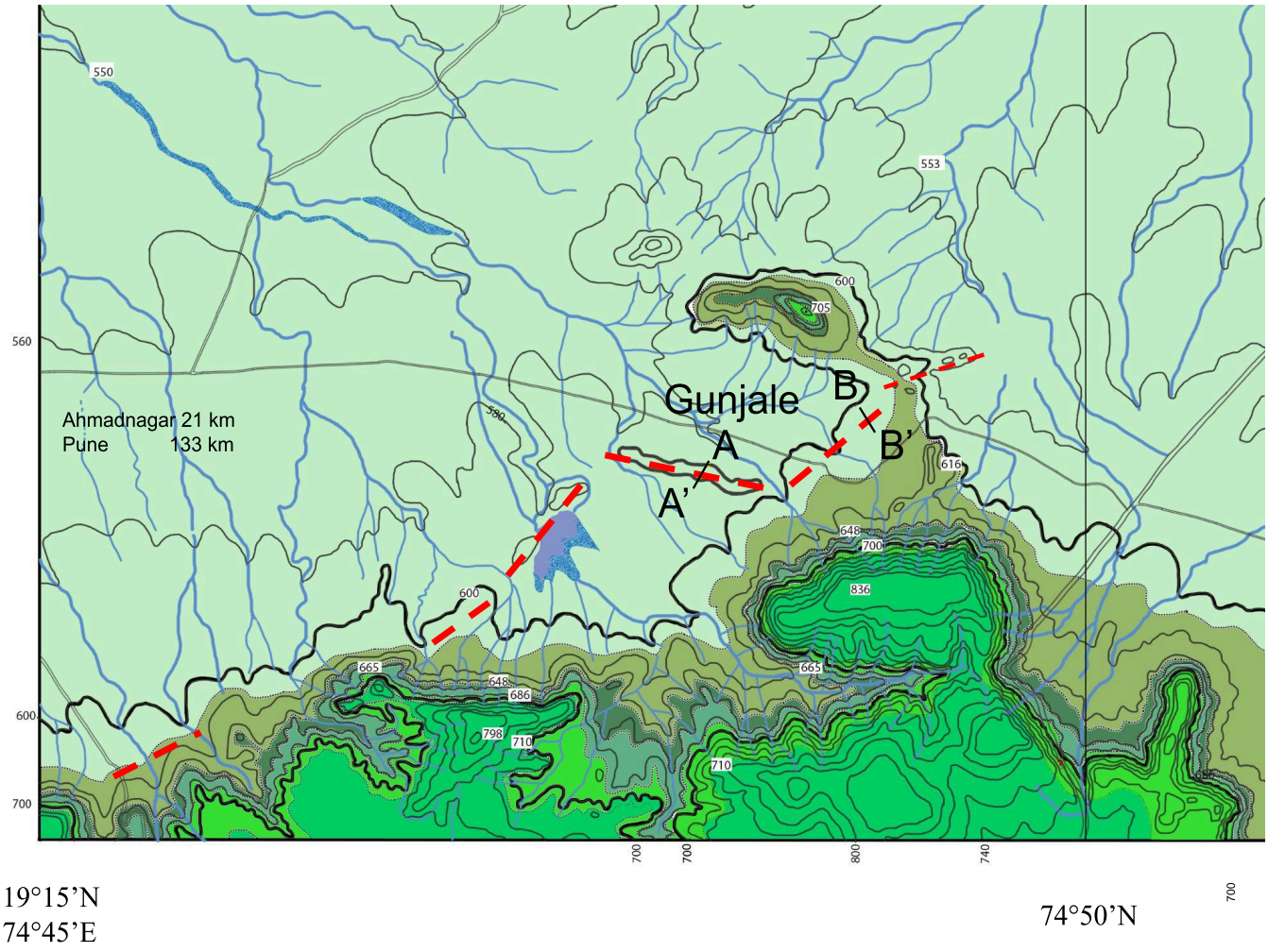

Fig. 5: Geological map of the Gunjale area showing the disposition of lava tube vis-a-vis the various basaltic lava flows.

Chapter 2: Materials and Methods

2.1 Field Mapping

The location was visited twice over the duration of the project. Preliminary mapping was done on the tube (Fig. 6a) using GPS and compass. Extensive sampling was done on both trips, with priority given to fresh samples from levees and core. We discovered cognates of unknown origin and a basaltic xenolith, which was removed using a portable rock corer. We had also chanced upon a freshly dynamited surface on the North levee on the first trip, which gave a great section as depicted in Fig. 5. Rough sketches were drawn on the field (Fig. 6b, c). All hand samples were categorised and described for record keeping and laboratory processing (Table 3).

Fig. 6a: Google Earth Pro satellite image of the Gunjale tube section showing the locations of the samples collected and described in Table 3.

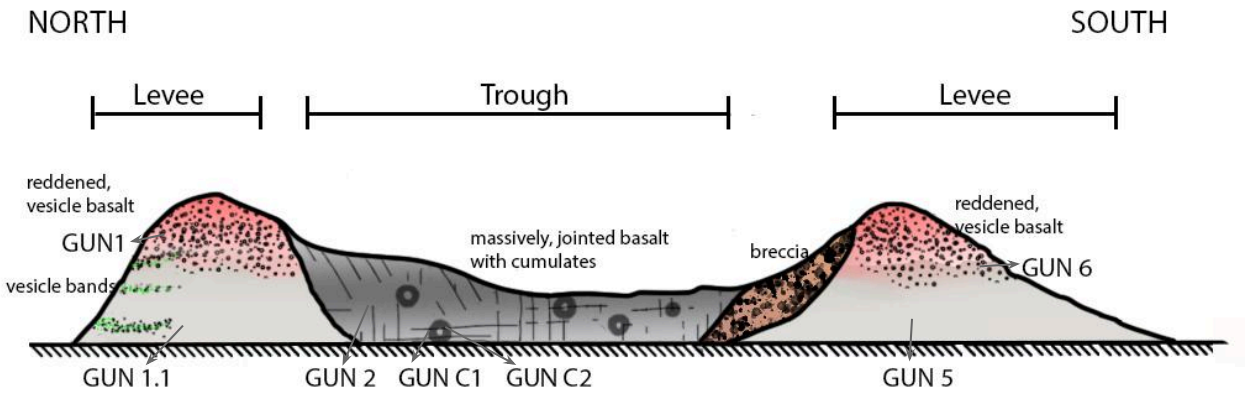

Fig. 6b: Field sketch of geological cross sections across the Gunjale lava tube in the mid-section (A- A'). Width of structure ~ 200 m, and height approximately 2.5 m from ground level.

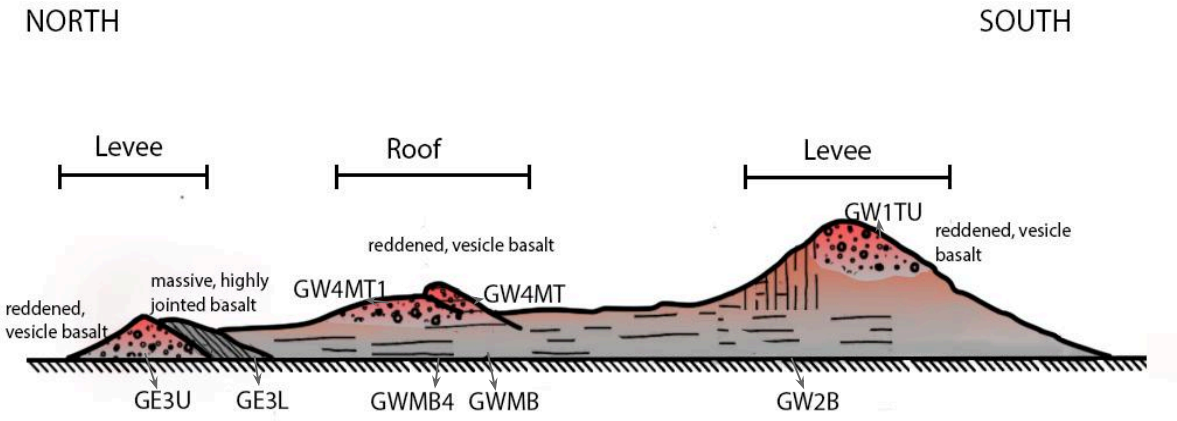

Fig. 6c: Field sketch of geological cross sections across the Gunjale lava tube towards the east end (B-B'). Width of structure 80 m, and height approximately 3 m from ground level.

Table 3: Location wise descriptions of the samples collected across the Gunjale tube section.

Sr. No.	Sample No.	Latitude, Longitude	Description
1	GUN 1	19.2791 N 74.8008 E	Reddish grey, Fine to Medium grained, Inequigranular, Vesicular, Stout plagioclases in a matrix of surface oxidised mafic material. Vesicular band 1.5 - 3 cm wide across the collected specimen. Drastic textural change within band- Plagioclases decrease in size, Highly irregular amygdules. Has at least two types of secondary minerals- cloudy white ovoid grains and transparent crystals
2	GUN 1.1	-	Gray, Very Fine grained, Inequigranular Evenly distributed amygdules- Circular to irregularly shaped, filled with secondary minerals.
3	GUN 2	19.2789 N 74.8004 E	Gray-Black, Micro Porphyritic, Inequigranular, Larger plagioclases (only up to 1 mm) suspended in a matrix of darker minerals and smaller plagioclases. Few disproportionately large plagioclases- limited porphyritic texture
4	GUN 3	-	Gray, Amygdaloidal, Inequigranular. Very long plagioclases (1mm-8mm) suspended in fine grained dark matrix with smaller plagioclase Sub rounded amygdules with secondary deposit of transparent crystals.
5	GUN 4	19.2789 N 74.8002 E	Dark grey- black, Very Fine grained, Large lathe-shape plagioclases (<5m) Rare vesicles (circular with white zeolite) Copious amounts of brown material, incl. on fresh cut surface.
6	GUN 5	-	Greyish Black, Equigranular, Some stout plagioclases, Hemicrystalline, Fine grained Rare vesicles containing secondary minerals,
7	GUN 6	19.2784 N 74.7994 E	Red fresh surfaces-oxidised- air cooled. Porphyritic texture with Very Large plagioclases clumped together. Smaller plagioclases scattered in the matrix.
8	Cumulate GUN C1 GUN C2	19.2783 N 74.8016 E	Fine grained with large ovoid aggregates of large dark minerals and plagioclases radiating from a centre, in a daisy-like fashion. Both the centre and matrix are fine grained, with dark minerals and small plagioclases.

2.2 Processing - Preparation of Powders and Thin Sections

The samples were cleaned thoroughly, before removing any parts that were visibly altered by hammering. I prepared chips of 5-8 cm with and 3-5 cm thickness, which were then processed by LAB CRYSTALS, a company based out of Uttar Pradesh for thin sections. The remaining chips were powdered by hand with an agate mortar, followed by further processing into powder of size <1μm with an automated agate ball mill.

2.3 Microscopy

The prepared slides were observed under 5x, 10x, and 20x magnification under the polarising light microscope to create an extensive knowledge base of the petrology of the samples. All samples were photographed in both Plain Polarised Light and Cross Polarised Light (mostly under 10x magnification) in IISER Pune's G1 geology laboratory.

2.4 Modal Composition Measurement

I used a Dollar point counter mechanical stage to measure the modal composition of minerals of all prepared slides, with extra emphasis on the slides selected for EPMA. We made sure that we had correctly identified major mineral compositions on the slides before, and manually moved the slide in a predetermined grid-like path to count exposed minerals. This was done 10 times for each slide, averaged, and converted to percentage to obtain modal composition. Please note there might be minor errors as the magnification was only at 10x, attachment of the mechanical stage was at the expense of the rotating stage, and it was difficult to distinguish between metastable states and oxides apart from boundary shapes.

2.5 XRF

Representative samples from levee and core groups were chosen. The rocks had already been crushed, pulverised and agated into very fine powder (<1μm), which ensured that the samples were homogeneous. This leads to uniform heating during the Loss Of Ignition (LOI) process. The sample was weighed, about 4 grams, and placed in crucibles where it was placed in the furnace set at about 650°C for about 6 hours. This single step process was done to get rid of possible volatiles which can cause problems during XRF.

These volatiles may include surface moisture absorbed by the powder, water in hydrated minerals, gases such as CO_2. Any contaminating organic matter also combusts in this process. The product is removed and weighed again. Then we make a fusion bead with lithium tetraborate which is then loaded in the XRF sample chamber of the Bruker WD X-ray Fluorescence machine

(model Tigor 8), here at IISER Pune. The XRF analysis was conducted using a Bruker XRF analyzer equipped with a rhodium (Rh) X-ray tube, operating at 50 kV and 40 mA. Calibration of the XRF spectrometer was meticulously performed using certified reference materials to ensure accurate and precise elemental quantification. The Bruker XRF analyzer measures the major oxide concentrations using the Geoquant Advance standard calibration method, providing an accuracy and precision of ±2% and ±1%. Elemental concentrations obtained from XRF analysis were then converted to oxide concentrations. The CIPW norm calculation method is a fundamental approach in petrology for estimating the mineralogical composition of rocks based on bulk chemical analysis. The normative mineral composition was calculated using the SINCLAS program of Verma et al. (2002). The program calculates the anhydrous recalculated data, gives a rock name following the Total Alkali Silica (TAS) diagram and also fixes the Fe_2O_3: FeO ratio for the given rock name and then calculates the norm. The SINCLAS program proved very useful as it provided the option of taking into account the subdivision of total iron. In the measured iron-oxidation ratio option, all iron was considered as $Fe_2O_{3(T)}$ the Middlemost option (Middlemost, 1989) was used, which proposed a fixed ratio of Fe_2O_3 to FeO that depended on the rock type (classification).

2.6 EPMA

For EPMS analyses, the prepared slides were further polished with 1µm and 0.3µm alumina powder, finally finished with diamond paste polish. This gave a mirror like sheen to the samples, which hopefully reduced uneven electron beam interactions. This also helped to distribute charge better on carbon coating. We chose 4 representative samples for spot analysis- GUN 1.1 for northern levee, GUN 6 for southern levee, GUN 2 for core material and GUN C1 for cognates, limiting measurements to about 50 per slide. We used a Cameca microprobe at the National EPMA facility in the Department of Earth Science, Indian Institute of Technology, Bombay to obtain Electron Probe Micro Analyses (EPMA) data and backscatter electron (BSE) images. All mineral phases from the rocks were analysed using strict protocol.The EPMA protocol was applied at an accelerating voltage of 15 kV with a beam current of 20 nA. The beam size was 0 µm for point analysis, and scanning was turned off. Minerals were identified from the given oxide wt.% and their stoichiometric calculations were made by referring to Appendix 1 from Deer et al., (1992). Fe^{+3} or Ferric ion was estimated using a general equation given by Droop (1987) and Schumacher (1991) for microprobe analyses. Using the mineral formula, end member's calculations were done for *sensu stricto* classifications of minerals. The data and results are presented in Supplementary Table 1-12.

Chapter 3: Results and Discussion

3.1 Physical Volcanology and Structure of the Gunjale Lava Tube

In this chapter we describe the geology and physical volcanology of the Gunjale tube. For the sake of convenience the cross section (see Fig. 6a, c) of the tube is described in detail here.

The northern levee of the lava tube represents a raised basalt boundary (Fig. 7a), bordering the relatively smooth surfaced tube core. This morphology suggests a slow lava flow during emplacement, allowing the interior of the lava to remain fluid and form a streamlined core-making the surface smooth. The vesicular crust (Fig. 7b) and angular basalt fragments (Fig. 7c), indicates accretion of lobes and breccia to form the northern levee indicating stable flow field conditions within a slow cooling regime. The vesicles were formed by trapped gas escaping through molten lava, and the amoeboid mega-vesicles (Fig. 7d) likely formed through the coalescence of smaller vesicles. This gas pooling represents variation in flow dynamics and cooling rate. Small proto-pipes (Fig. 7e) formed in the basaltic lobes, which depict degassing paths within individual still plastic lobes from the lava flow that accredited to the lava leeve. The accumulation of small cognates along the inner side of the levee are probably a product of erosive internal movement, when small pre-crystallised fragments within the lava tube interior (core) get carried by the flow and settle in regions where the flow slows down.

We found a section of the northern levee which had been dynamited by the locals for road metal to be used for building construction purposes. A large sheet lobe is exposed near the surface (Fig. 8a). The sheet lobe is red, highly oxidised and moderately-highly vesicular. The oxidation may be a result of surface interaction of atmospheric oxygen during the cooling and the post eruption emplacement. Plagioclase phyric massive basalt (Fig. 8b) representing the core of the thick sheet lobe is also visible at the base of the section. Couple of tapering segregation vesicle sheets exposed in the massive core (Fig. 8c). The tapering segregation vesicle sheets (Fig. 8d) are exposed in the massive core representing the intersection of the advancing cooling front from the surface to the lobe interior. Thick, vesicular cylinder feeding a couple of levels of horizontal vesicular sheets (Fig. 8e). We see (atleast) 3 sets of perpendicular joints that produced cuboidal blocks of massive basalt (Fig. 8f). The jointing represents rapid cooling in a thick sheet lobe of basalt.

The core of the tube is represented by a bouldery surface (Fig. 9a) due to formation of 3 sets of perpendicular cooling joints. Highly oxidised basalt in the core (Fig. 9b) suggests prolonged exposure to the surface where atmospheric oxygen interacted with the channel levee. The core of the lava is massive but contains sporadic vesicles (Fig. 9c) and contains spherical to elongated plagioclase- clinopyroxene cognates (Fig. 9d, e). The presence of small (2 mm-7 cm) spherical-oblong cognates reflects a different type of crystallisation as compared to the matrix of the core.

The oblong shape is a product of an environment with shearing forces or a sign of differential flow velocities within the tube. The cognates were not present all over the core, and were clustered in the eastward section, which suggests that they settled out of the flowing lava and the speed was probably less in this region.

The southern levee is characterised by a linear ridge-like low lying wall of fine grained basalt (Fig. 10a). Near village Gunjale the southern levee (Fig. 10b) is represented by nearly a tall vertical ledge (1.8 m) with a clear contact with the massive core of the lava tube (Fig. 10c). This sudden increase in the may be due to steeper cooling gradient compared with the northern levee. We see jointing on this levee as well, with 3 planes being more apparent (Fig. 10d). This results in cube-cuboids of basalt which is common when thick layers of lava cool and shrink. The region is not heavily vesiculated but still has some irregularly shaped vesicles. The massive basalt from the southern levee contains large silica/agate rich gas vesicles (Fig. 10e) It also contains small vesicular basaltic xenoliths (Fig. 10f). Close to the southern leeve there are accumulations of basaltic breccias. The higher elevation and volcanological features is achieved due to greater accretion of basaltic lava and breccias in comparison to the northern levee.

3.2 Thin Section Analysis

In this section we describe the detailed description on the textures and petrography of the representative samples from the lava tube levees and the core. These provide important insights into the emplacement dynamics and cooling history of the lava tube.

The northern leeve is fine grained and the opaques are highly oxidised leading to red coloration of the rock. The basalt showing a predominantly glassy appearance and intersertal texture (Fig. 11a). Large subhedral plagioclase and opaque crystals are seen in the basalt (Fig. 11b). Some plagioclase constitute the micro porphyritic texture (Fig. 11c). Several small euhedral to subhedral plagioclase crystals show polysynthetic twinning between cross nichols. The smaller plagioclase crystals occur in subophitic relationships with larger clinopyroxene crystals (Fig. 11d).

The thin sections from the southern leeve are also fine grained basalt that is rich in groundmass (Fig. 12a). Between cross nichols, the groundmass plagioclase show multiple twinning Plagioclase meshwork encloses minor clinopyroxene and small opaque grains there by constituting the intergranular texture (Fig. 12b, c). Phenocrysts of plagioclase within a fine groundmass of plagioclase, pyroxene and opaque lend a micro porphyritic texture to the rock. The plagioclase phenocrysts occur as aggregate or in glomeroporphyritic clusters. Individual phenocrysts show shrap grain boundaries and tick twin lamellae between cross nichols (Fig. 12d).

Fig. 7: Field photographs of the northern levee. (a) Panoramic view of the northern levee showing the raised basaltic boundary. Note the smooth surface of the tube core within the levee. (b) The smooth surfaced vesicular crust constituting the northern leeve. (c) Slabs of angular fragments of vesicular basalt preserved within the northern levee. (d) Vesicles of variable size and shape as seen in the northern leeve. Note the amoeboid mega vesicle formed due to the coalescence of small spherical vesicles. (e) Small proto pipes formed in the basaltic lobes constituting the northern levee. (f) Accumulation of small spherical cognates along the inner side of the northern levee

Fig. 8: Field photographs of the fresh dynamited section along the northern levee.
(a) Ledge exposing the part of the highly oxidised vesicular sheet lobe.
(b) Plagioclase phyric massive basalt representing the core as exposed at the base of the ledge.
(c) Couple of tapering segregation vesicle sheets exposed in the massive core.
(d) Slender vesicular sheets exposed at the base of the highly oxidised crust.
(e) Thick, vesicular cylinder feeding a couple of levels of horizontal vesicular sheets.
(f) The core of the northern leeve showing three sets of jointing that produces cuboidal blocks of massive basalt.

Fig. 9: Field photographs of the core of the lava tube.
(a) Bouldery surface of the core of the lava tube as seen against the basaltic hill in the background.
(b) Highly oxidised vesicular basalt in the core zone proximal to the northern levee.
(c) Close up of an oxidised vesicular core.
(d) Small spherical to oblong cognates within the core of the lava tube.
(e) Closeup of fresh oblong mafic cognate exposed in the massive basalt of the lava tube.

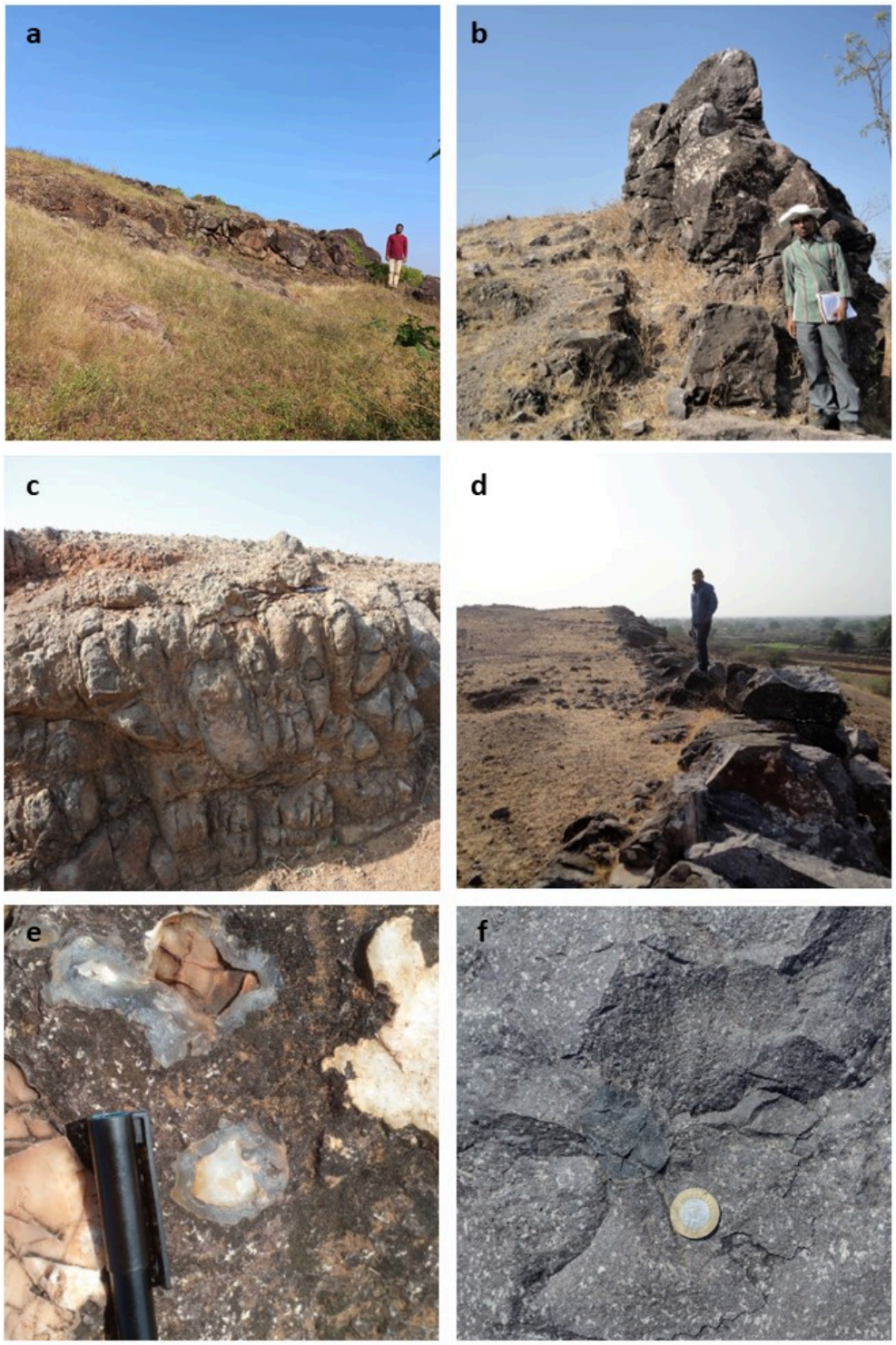

Fig. 10: Field photographs of the right levee of the lava tube. (a) Panoramic view of the southern leeve ledge. (b) Contact between the massive tube core and vertical ledge of the southern leeve as seen near village Gunjale. (c) 3 sets of mutually perpendicular cooling joints in the massive tube core. (d) View of the southern leeve forming a wall like ridge. Note the smooth surfaced (with small boulders) depression constituting the core of the lava tube. (e) Irregular vesicles with deposition of secondary minerals (f) Xenolith

The margin of the tube core adjacent to the lava levees is also fine grained basalt made up of plagioclase, clinopyroxene and opaque showing intergranular texture (Fig. 13a). This zone of fine grained basalt is fresh, un-oxidised and shows abundance of small, euhedral opaque grains (Fig. 13b). Large plagioclase phenocrysts occur as glomeroporphyritic aggregates within a fine groundmass of plagioclase, clinopyroxene and opaque. Individual plagioclase phenocrysts are euhedral with sharp grain boundaries suggesting slow growth in a stable magma chamber. Between cross nichols they exhibit thick twin lamellae (Fig. 13c). Some inclusions occur within the plagioclase phenocrysts. Large angular fragments of plagioclase phenocryst showing variations in the twin lamellae and alteration along the fractures are also seen (Fig. 13d). The presence of such crystal fragments of plagioclase phenocrysts suggest fracturing and breaking either during transportation in the magma plumbing system or during eruption at the vent or subsequently during lava flowage in the lava tube.

The petrography of cognates from the lava tube core shows some interesting insights into their genesis and cooling. The central parts of the cognates are fine grained and show subophitic relationship between plagioclase and clinopyroxenes (Fig. 14a). They show large opaque crystals within the silicates (Fig. 14b). The contact between the fine grained cognate centre and the coarse grained periphery made up of cumulus clinopyroxenes and plagioclase is perceptible in thin sections. The twinned clinopyroxene are common in the coarser rim. Large intergrowth of clinopyroxenes and plagioclase crystals are common towards the cognate periphery (Fig. 14c). Cumulus growth of plagioclase and opaque is also seen in the cognate (Fig. 14d). Based on the texture it appears that the fine grained cognate interior formed under normal crystallisation during magma ascent and flowage into the tube and later stagnation in the insulated lava tube led to the larger crystal growth in the cognate periphery.

The modal analyses of 13 samples from the Gunjale lava tube show significant variations in the constituent mineral content (Table 4). The plagioclase content varies from 37.84% to 49.23% while the clinopyroxenes vary from 1.56 to 41.07%. There is a significant variation in the opaque content (5.6% to 20.4%) and mesostasis (glass + microlites- 1.73% to 42.22%). Depending on weather the sample is from the core or the levee. In general, the lava from the core has higher plagioclase and opaques while the levees are richer in glass + microlites in keeping with the differential thermal regimes and cooling history of the parts of the lava tube.

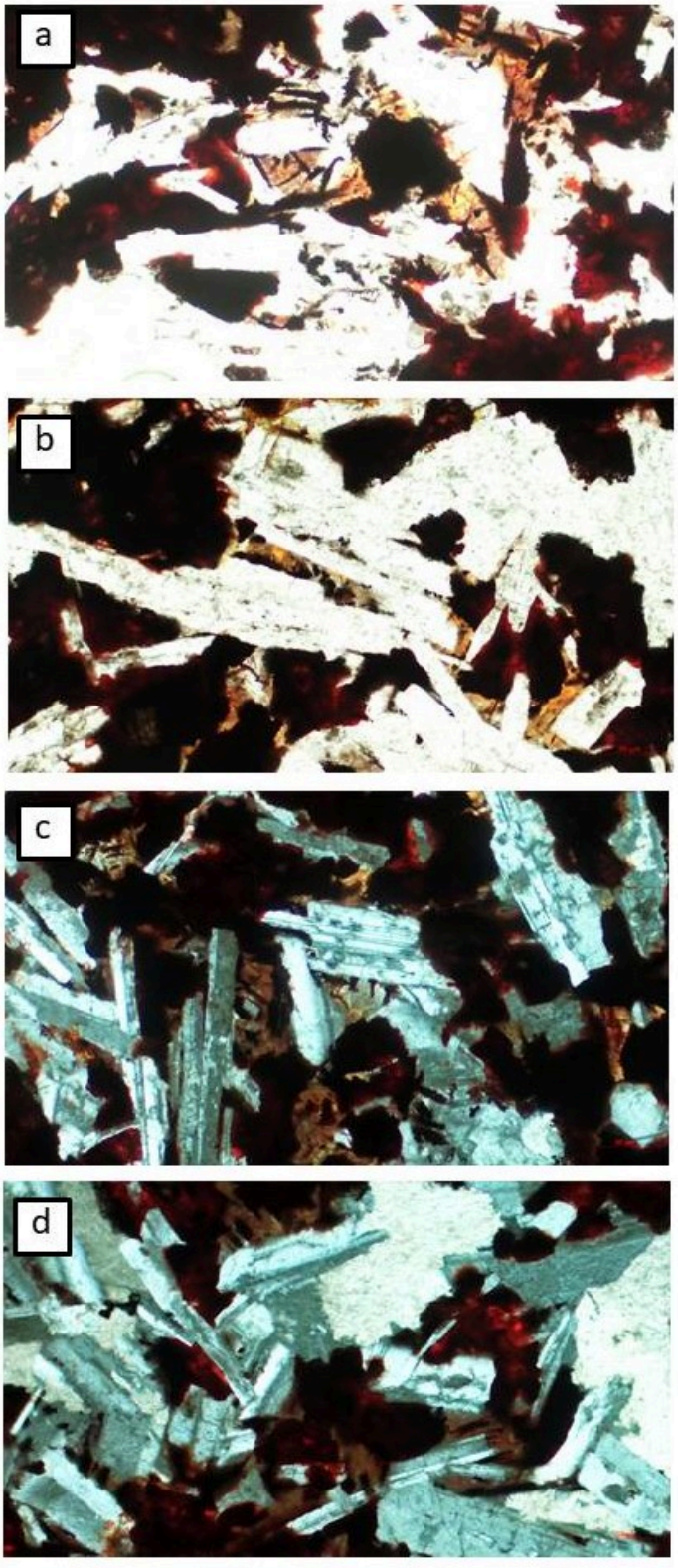

Fig. 11: Photomicrographs from the northern leeve.
(a) Fine grained basalt showing intersertal texture. Note the oxidation of the opaques leading to red coloration of the rock.
(b) Large subhedral plagioclase and opaques.
(c) Small euhedral to subhedral plagioclase crystals showing twinning.
(d) Plagioclase- clinopyroxene in subophitic relationship.
Photomicrographs a and b in plane polarised light and c and between cross nichols.

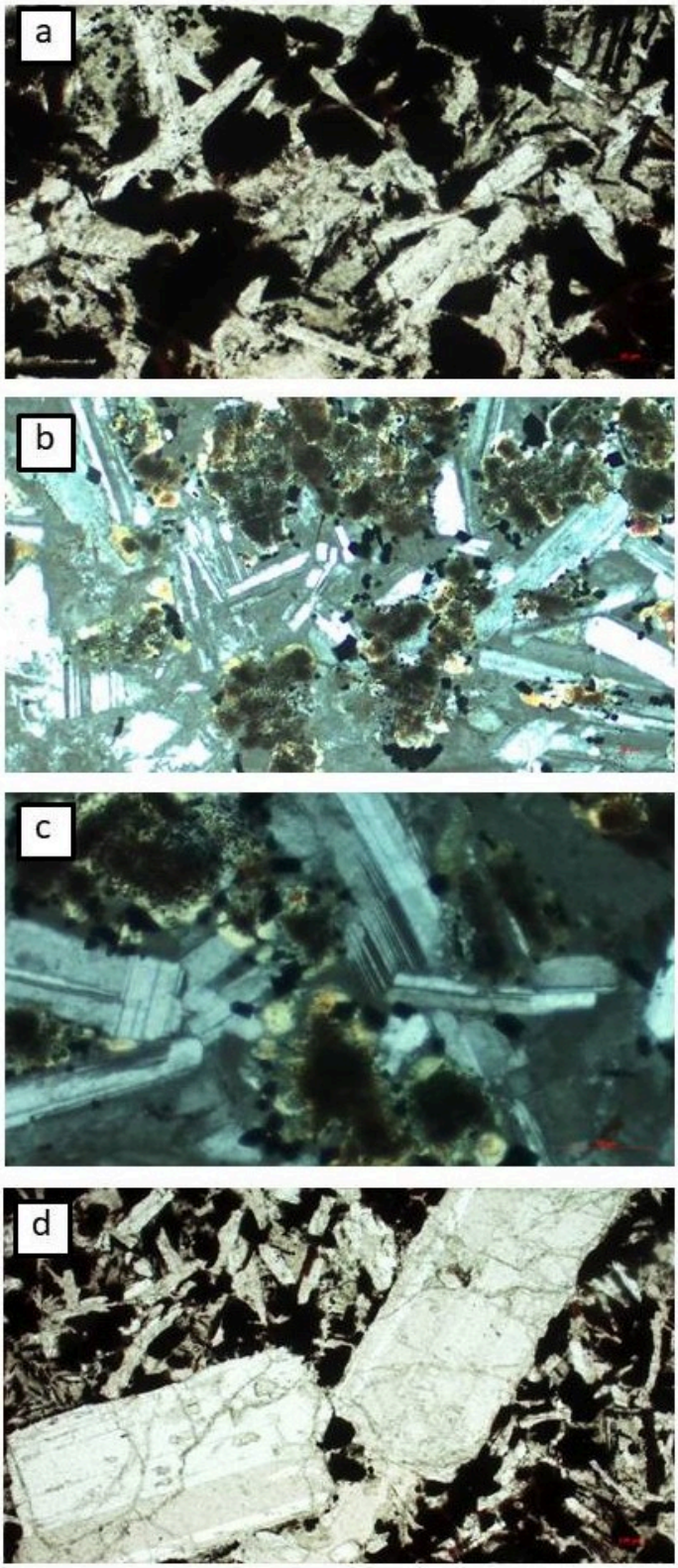

Fig. 12: Photomicrographs from the southern leeve. (a) Fine grained basalt showing lath-shaped plagioclase- clinopyroxene-opaque groundmass. (b) Groundmass plagioclase with minor clinopyroxene and small opaque grains. (c) Large lath-shaped plagioclase crystal showing twining. Note the fine grained aggregate of opaque and clinopyroxene between the plagioclase crystals. (d) Phenocrysts of plagioclase within a fine groundmass of plagioclase, pyroxene and opaque. Photomicrographs a and d in plane polarised light and b and c in between cross nichols.

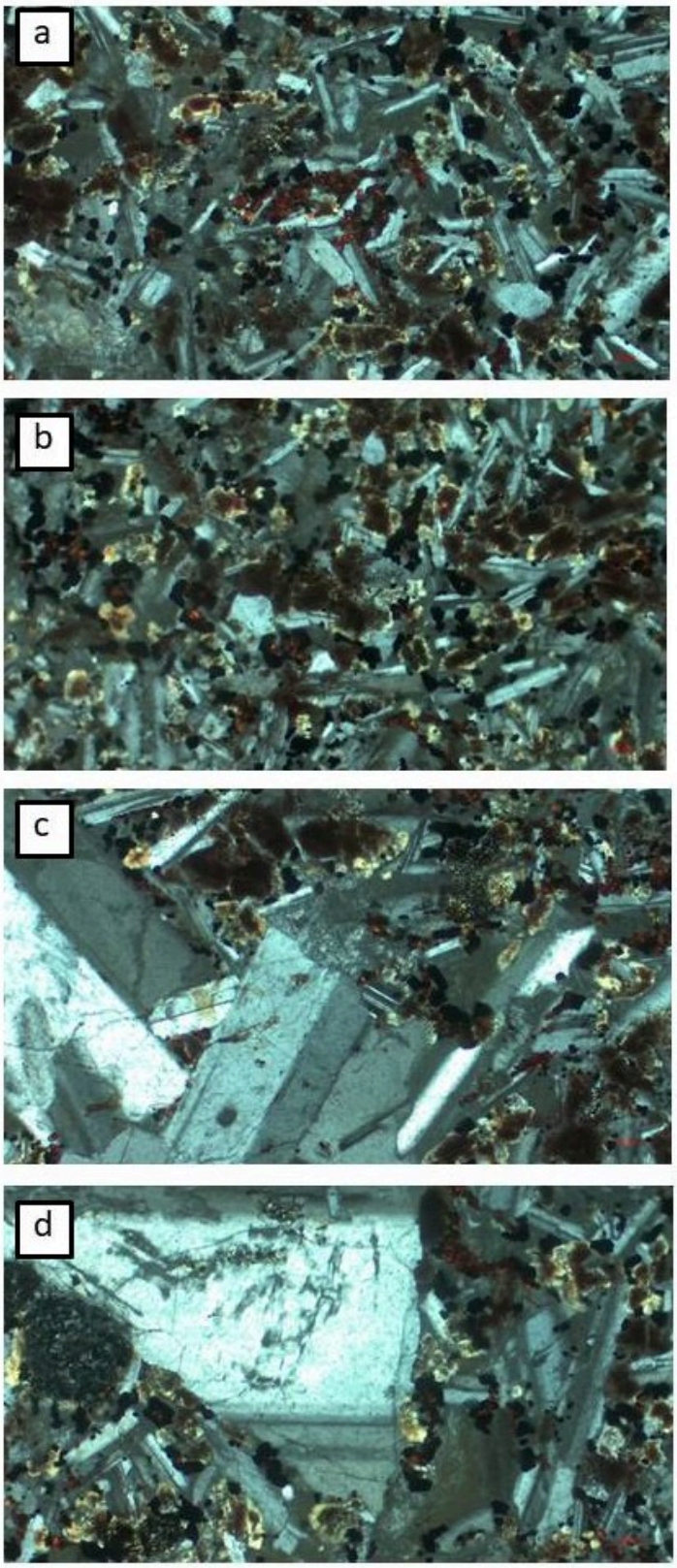

Fig. 13: Photomicrographs from the tube core.
(a) Fine grained basalt showing intergranular texture.
(b) Fine grained basalt showing abundance of euhedral opaque grains.
(c) Large plagioclase phenocrysts within a fine groundmass of plagioclase, pyroxene and opaque. Note the thick twin lamellae and inclusions within the plagioclase phenocrysts.
(d) Large angular fragment of plagioclase phenocryst showing variations in the twin lamellae and alteration along the fractures.
All photomicrographs between cross nichols.

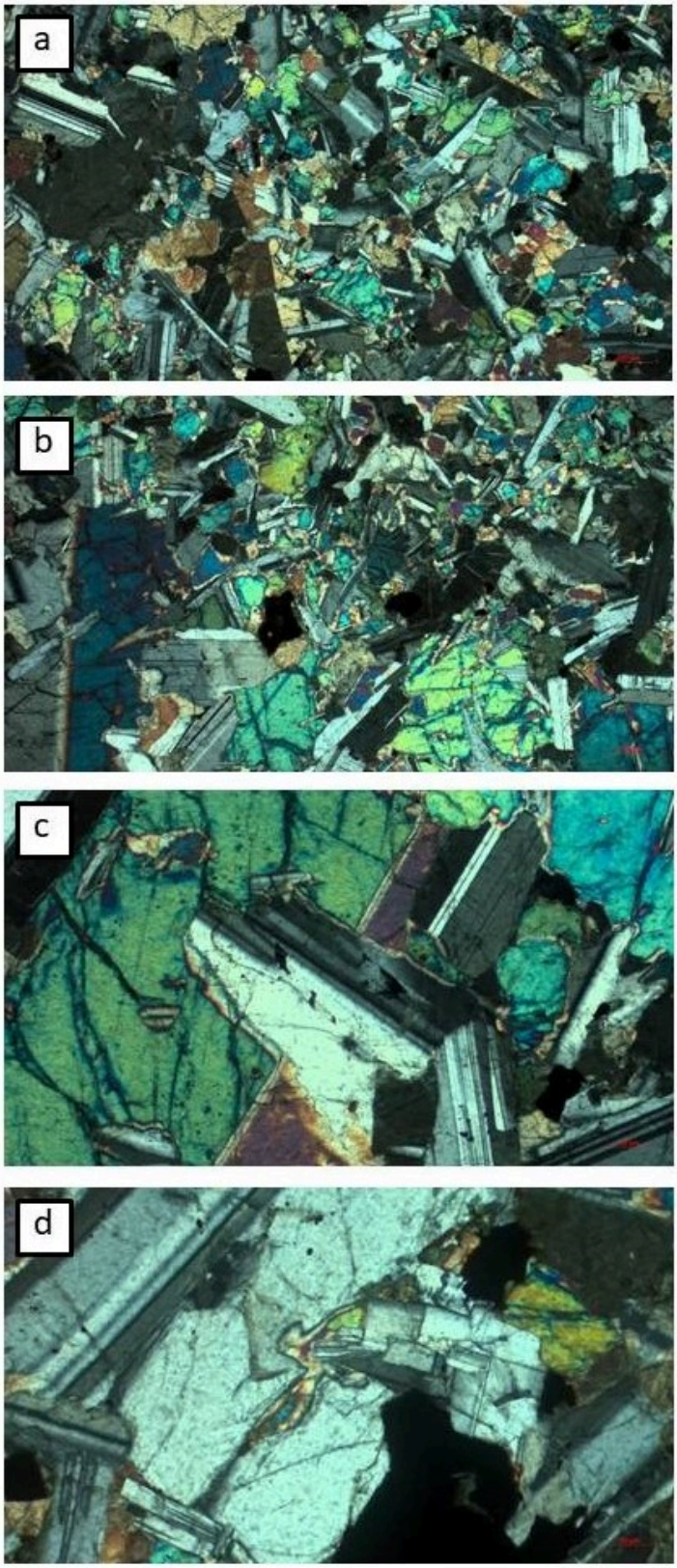

Fig. 14: Photomicrographs of cognates from the lava tube core.
(a) Central parts of the cognates showing subophitic Relations between plagioclase and clinopyroxenes. Note the large opaque crystals within the silicates.
(b) Contact between the fine grained cognate centre and the coarse grained periphery made up of cumulus clinopyroxenes and plagioclase. Note the twinned clinopyroxene towards the left of the photomicrograph.
(c) Large intergrowth of clinopyroxenes and plagioclase crystals periphery towards the cognate.
(d) Cumulus growth of plagioclase and opaque in the cognate.
All photomicrographs between cross nichols.

Table 4: Classification of rock by modal percentage (%) of each mineral

Sr. No.	Slide number	Plagioclase	Clinopyroxene	Opaque	Mesostasis	Other
1	GUN 1	37.84	12.94	7.00	42.22	0.00
2	GUN 1.1	49.23	1.56	8.74	34.16	6.31
3	GUN 2	44.03	17.43	13.95	23.28	1.31
4	GUN 3.2	46.13	10.22	11.02	32.28	0.34
5	GUN 5	46.15	20.37	10.08	12.28	11.12
6	GUN 6	48.37	3.44	20.40	24.56	3.22
7	GUN C1	43.20	37.07	8.95	9.98	0.80
8	GUN C2	47.95	40.17	9.88	1.75	0.25
9	GW 2B	49.20	40.49	8.30	1.73	0.27
10	GW 2B’	46.98	38.24	8.80	5.98	0.00
11	GWMB	48.59	39.02	5.60	6.68	0.10
12	GW1TU	39.73	10.97	13.97	35.32	0.00
13	GWM5	43.48	41.07	7.71	5.77	1.97
Minimum		37.84	1.56	5.60	1.73	0.00
Maximum		49.23	41.07	20.40	42.22	11.12
Median		46.15	20.37	8.95	12.28	0.34
Standard Deviation		3.63	15.51	3.87	14.35	3.29

3.3 Backscattered Electron Imagery

Backscattered Electron images of basalt from the parts of the Gunjale lava tuber were obtained at IIT, Mumbai.The BSE images show significant textural variations similar to those seen in the optical microscopy. The sample from the northern levee (GUN 1.1) shows coarse grained

texture of basalt consisting of clinopyroxenes, plagioclase and opaques (Fig. 15a). The rock is characterised by the irregular form of large titano-magnetite crystals (Fig. 15b) . (Fig. 15c) At places intercumulus crystallisation of plagioclase within a clinopyroxene framework is seen in the rock.

The backscattered electron image of basalt from the southern levee (GUN 6) show typical miroporphyritic textures (Fig. 16a) due to presence of large, euhedral plagioclase phenocryst within fine grained groundmass. The groundmass phases contain plagioclase, clinopyroxenes and opaques (Fig. 16b). Large subhedral plagioclase and clinopyroxene phenocrysts in a glomeroporhyritic association are also seen within the fine grained groundmass (Fig. 16c). In general, the titanomagnetite crystals occur as skeletal form suggesting reabsorption (Fig. 16b). In some parts of the polished section large slender, lanceolate opaque crystals are seen indicating significant undercooling due to water vapour.

The backscattered electron image of basalt from lava core margin (GUN 2) shows fine grained, microporphyritic textured basalt (Fig. 17a). Intersetal glassy texture within the groundmass phases plagioclase, clinopyroxenes and opaques are common (Fig. 17b). Extremely fine grained opaque crystals are disseminated throughout the groundmass. At places, glomeroporphyritic accumulations of plagioclase phenocrysts (Fig. 17c) within fine grained groundmass are seen (Fig. 17c). The BSE images of the cognate sample from core (GUN C1) were also used to reconfirm the inferences drawn from the petrographic studies. However the large size of the cognate did not permit a low power image in one screen. Hence we decided to concentrate on the interface between the fine-grained and the coarse-grained part of the cognate to bring out the textural variations (Fig. 18a). From the image it is clearly seen that the cognate interior is relatively fine grained and composed on plagioclase and clinopyroxene with large skeletal opaques. The periphery of the cognate is coarser and contains radiating aggregates of alternating plagioclase and clinopyroxene crystals.

Elemental X-ray mapping of the interface between the fine-grained and the coarse-grained part of the cognate was undertaken as feeble zoning was seen in the BSE images. The elemental map for Ca shows significant variations ((Fig. 18b). In the elemental map there appears to be a diffuse distribution of Ca in the clinopyroxene interior. In contrast, there appears to be a feeble zoning in the terms of Ca in the large clinopyroxene in the peripheral regions of the cognate. From the elemental map and data (Table 3.3) it is clear that the clinopyroxene is magmatically zoned. No zoning is seen in the Al distribution (Fig. 18 c) elemental X-ray maps. However, the highly Al-content in plagioclase vis-a-vis is seen clearly. There is considerable variation in the Na-content of plagioclases with the rims being richer in an-content. The feeble zoning seen in the silicate minerals of the cognate clearly indicates the role of fractional crystallisation.

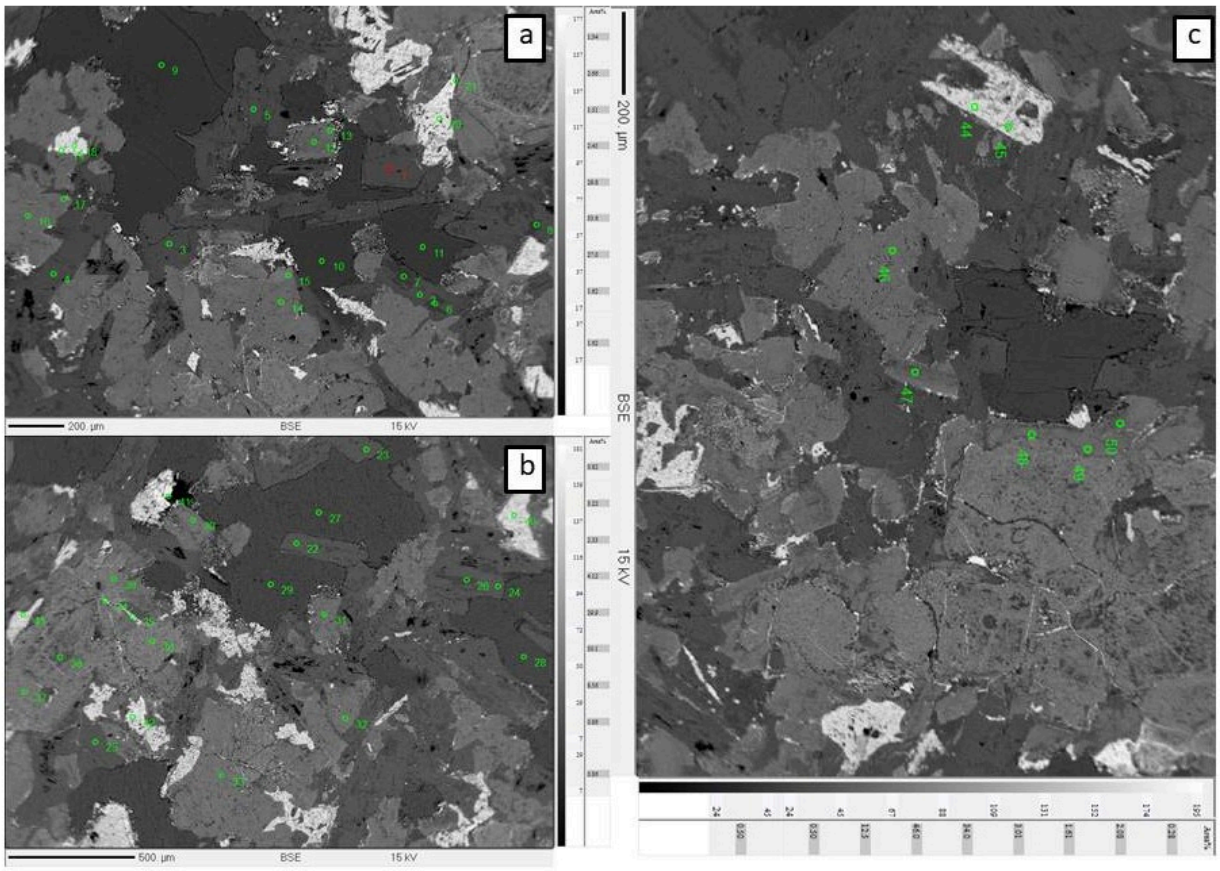

Fig. 15: Backscattered Electron image of basalt from northern levee (GUN 1.1). (a) Coarse grained texture of basalt consisting of clinopyroxenes, plagioclase and opaques. (b) Another view of the cumulate accumulation of plagioclase, clinopyroxenes and opaques. Note the irregular form of the titano-magnetite crystals. (c) Intercumulus plagioclase with clinopyroxene in the rock.

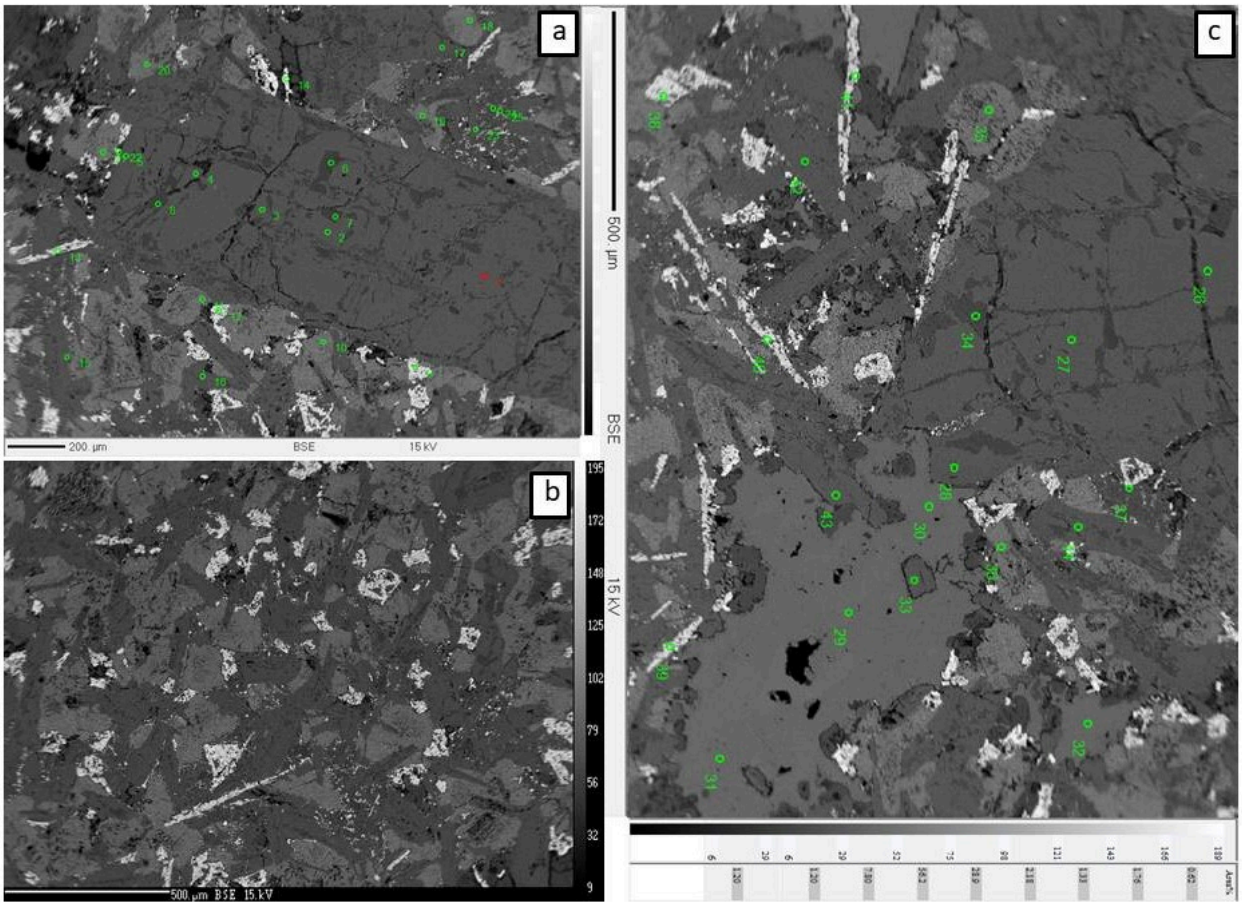

Fig. 16: Backscattered Electron image of basalt from southern levee (GUN 6) (a) Large, euhedral plagioclase phenocryst within fine grained groundmass. (b) Groundmass phases containing plagioclase, clinopyroxenes and opaques. Note the skeletal nature of the titanomagnetite crystals. (c) Large subhedral plagioclase and clinopyroxene phenocrysts within fine grained groundmass. Also seen are large slender, lanceolate opaque crystals indicating significant undercooling.

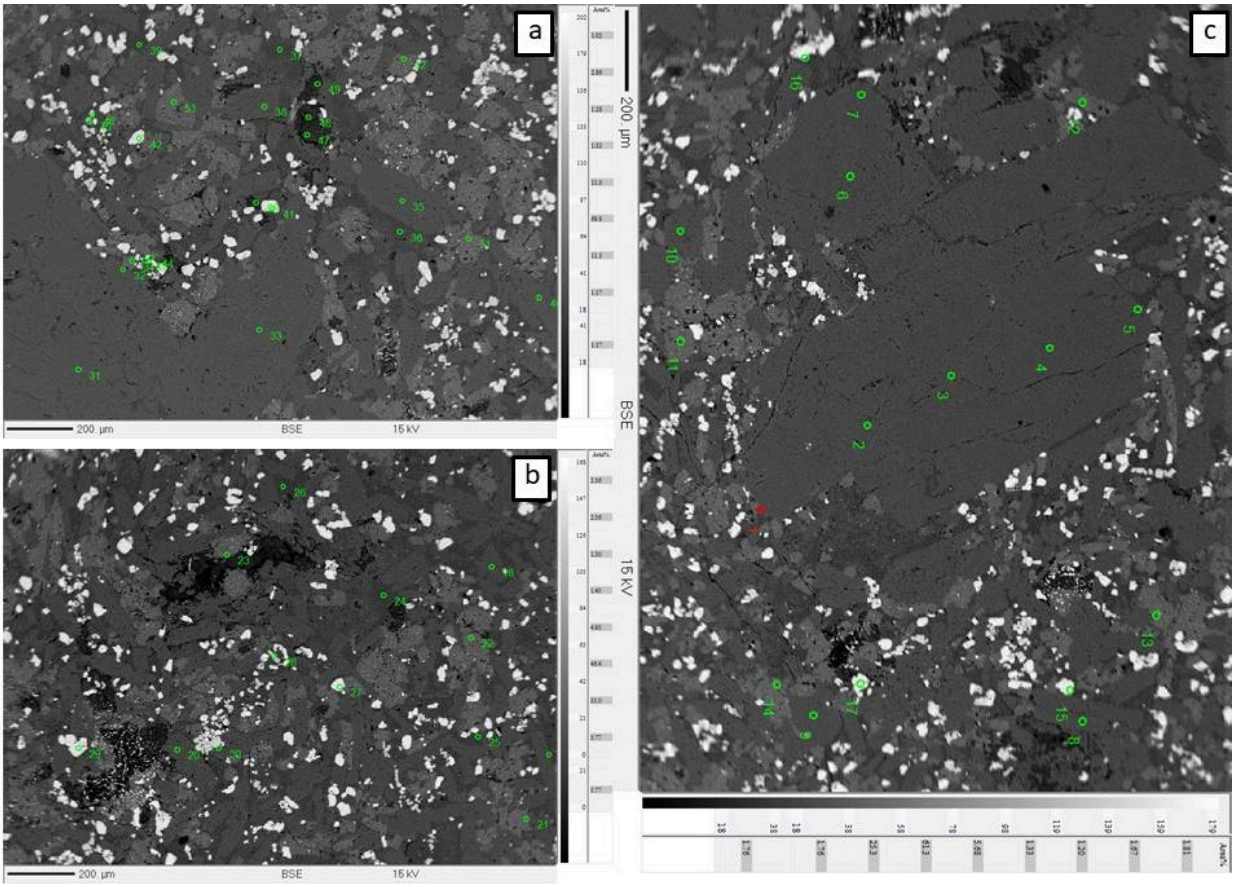

Fig. 17: Backscattered Electron image of basalt from the core (GUN 2). (a) General view of the basalt shows fine grained micro porphyritic texture. (b) Intersetal glassy texture of the groundmass phases plagioclase, clinopyroxenes and opaques. Note the extremely fine grain size of the opaque crystals. (c) Glomeroporphyritic accumulations of plagioclase phenocrysts within fine grained groundmass.

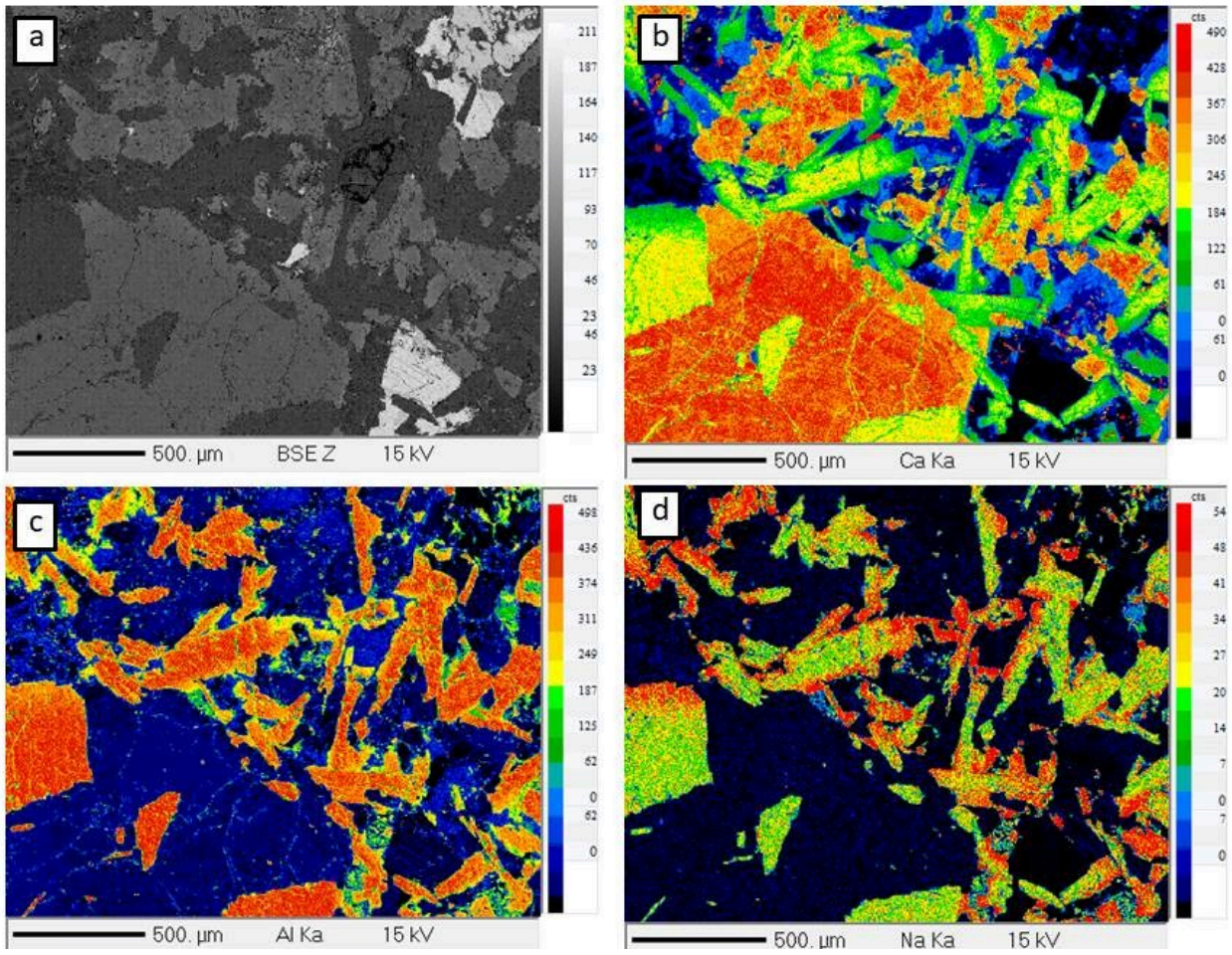

Fig. 18: Backscattered Electron image of the cognate sample from core (GUN C1). Note the boundary- one large grain surrounded by a smaller matrix. (a) Backscattered Electron image and Elemental X-ray maps showing distribution of (b) Ca, (c) Al, and (d) Na in the various minerals found in the cognate within the core.

3.4 Mineral chemistry

The polished sections from 4 representative samples from the Gunjale tube were selected based on their freshness and analysed by Electron Probe Micro Analyses (EPMA) using a Cameca microprobe at the Department of Earth Science, Indian Institute of Technology, Bombay. The data is presented in the Supplementary Table 1-12 and discussed below.

3.4.1 Pyroxene

In the northern lava levee (GUN 1.1) sample (Supplementary table 7), SiO_2 shows a wider range (38.43–66.85 wt%), with Al_2O_3 ranging from 0.67 to 2.39 wt%. FeO concentrations are significantly higher compared to the core sample, ranging from 8.99 to 38.33 wt%. MgO ranges

from 0.02 to 19.87 wt%, and CaO varies wildly- 0.1 to 18.72 wt%. Mg# values vary greatly, ranging from 0.093 to 86.46 and the overall composition is $Wo_{0.33-45.07}En_{0.09-72.10}Fs_{7.48-99.57}$ (Fig. 19), indicating diverse pyroxene populations.

The pyroxenes in the GUN 2 (Supplementary table 8) sample represent the core and show SiO_2 ranging from 48.33 to 53.46 wt%, with TiO_2 between 0.6 and 1.79 wt%. Al_2O_3 varies between 2.21 and 3.52 wt% while the FeO content ranges from 5.26 to 11.54 wt%. MgO ranges from 14.10 to 17.15 wt% and CaO varies from 16.57 to 21.73 wt%. Mg# values range from 71.76 to 96.64. The overall pyroxene composition varied within $Wo_{37.44-46.55}En_{44.68-51.44}Fs_{1.84-17.58}$ (Fig. 20).

The pyroxenes in the GUN 6 (Supplementary table 6) sample represent the southern levee and contain SiO_2 from 30.01 to 50.75 wt%, with higher TiO_2 concentrations, ranging from 0.91 to 11.48 wt%. Al_2O_3 shows a large variation, between 1.99 and 16.99 wt%.FeO varies between 10.23 and 23.05 wt%, MgO content varies between 0.63 and 15.1 wt%, and CaO shows large variation (2.95 to 19.19 wt%). Mg# values range widely, from 4.646 to 94.5, and overall pyroxene composition is in the range of $Wo_{14.45-48.72}En_{30.61-56.83}Fs_{15.28-41.74}$ (Fig. 21).

Pyroxenes from GUN C1 show SiO_2 content between 45.93 and 52.88 wt%, with TiO_2 ranging from 0.03 to 1.11 wt%. Al_2O_3 varies from 0.59 to 6.11 wt%. FeO content ranges from 9.4 to 24.89 wt%, while MgO ranges between 10.22 and 16.35 wt%. CaO varies from 1.95 to 19.33 wt% and compositions range from $Wo_{4.87-40.90}En_{30.61-56.38}Fs_{15.28-41.74}$ (Fig. 22).

Separating and measuring 13 of the larger pyroxene grains in the cognate (Supplementary table 9), SiO_2 content ranges from 50.52 to 52.88 wt% and Al_2O_3 varies from 0.59 to 2.53 wt%. FeO content is higher, from 9.9 to 24.89 wt%, and MgO ranges from 13.26 to 16.15 wt%. CaO content varies between 5.11 and 18.76 wt%. Mg# values range from 53.12 to 74.55 and pyroxene range from $Wo_{10.98-39.60}En_{39.53-47.29}Fs_{15.54-41.74}$. In the 8 matrix pyroxene grains analysed (Supplementary table 10), SiO_2 content is between 45.93 and 51.71 wt%, with TiO_2 present in trace amounts (up to 0.89 wt%). Al_2O_3 ranges from 1.1 to 6.11 wt%, and FeO varies between 9.4 and 21.1 wt%. MgO content ranges from 10.22 to 16.35 wt%, while CaO content ranges from 1.95 to 19.33 wt%. Mg# values range from 46.33 to 74.13. Overall pyroxene composition is $Wo_{4.87-40.90}En_{30.61-56.38}Fs_{15.28-38.29}$.

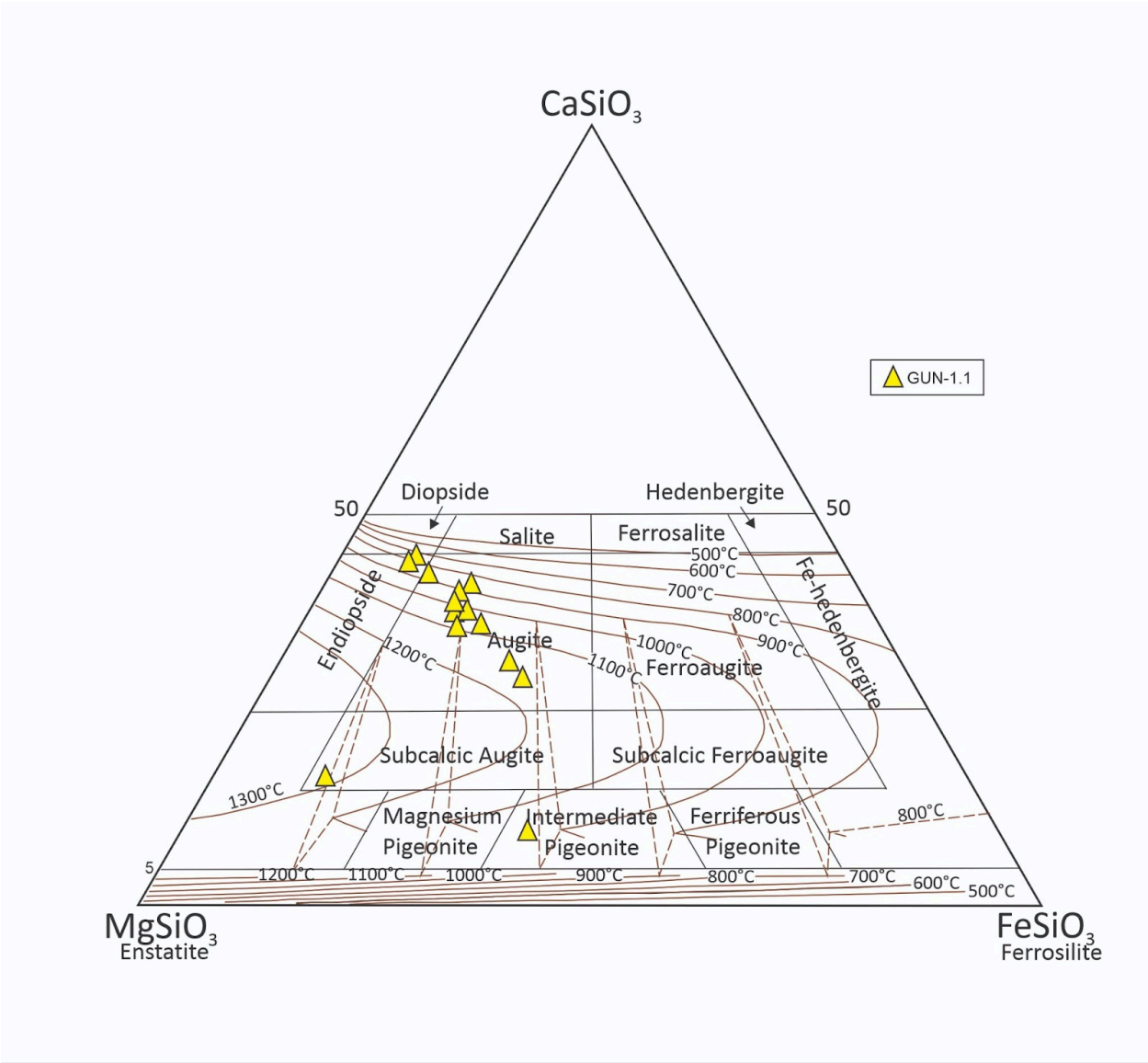

Fig. 19: Northern lava levee (GUN 1.1) samples plotted on the Hess's triangle (MgSiO3-FeSiO3-CaSiO3) for pyroxene (nomenclature after Morimoto, 1988). Also plotted are isotherms after Lindsley (1983).

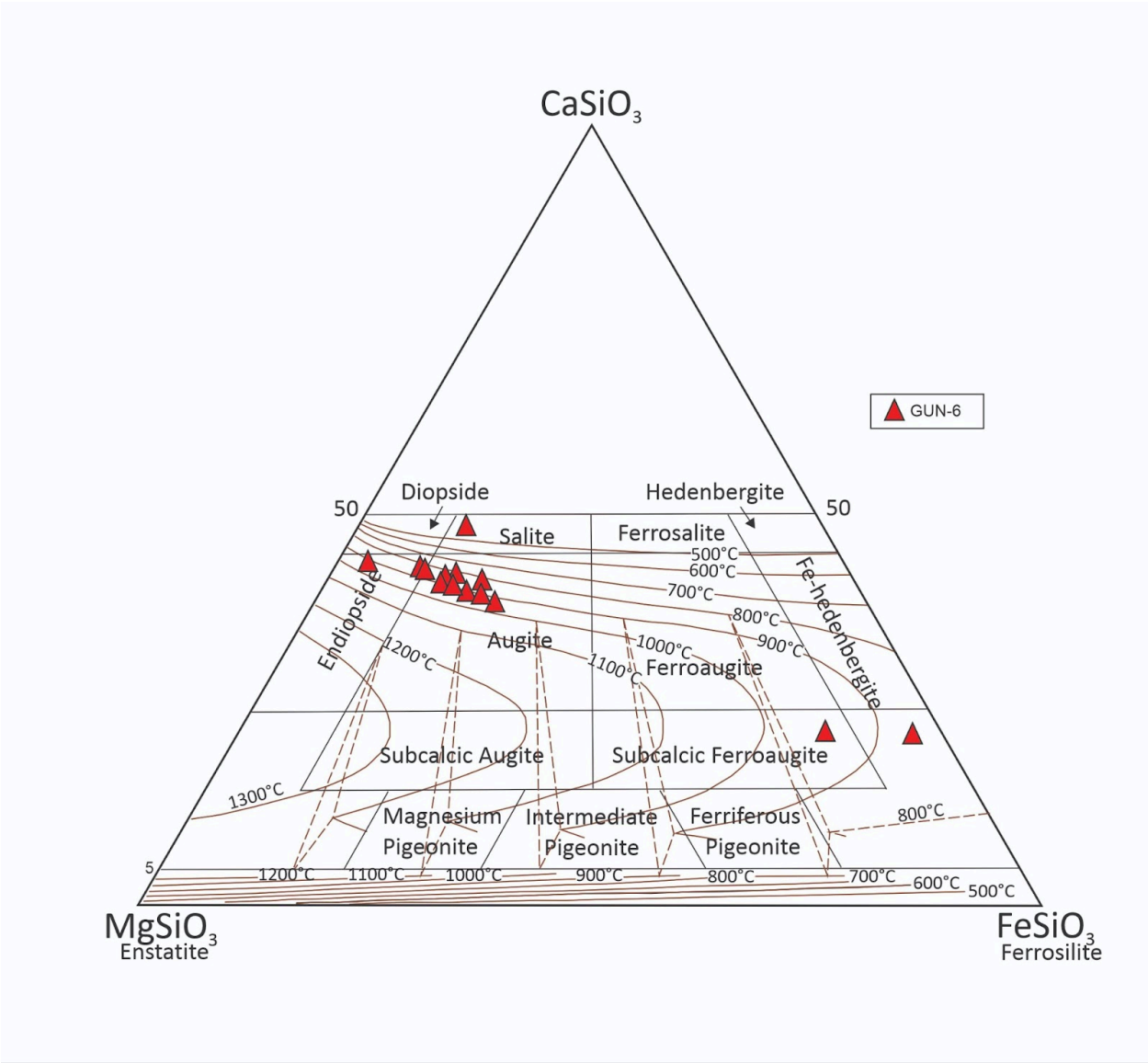

Fig. 20: Southern levee (GUN 6) plotted on the Hess's triangle (MgSiO3-FeSiO3-CaSiO3) for pyroxene (nomenclature after Morimoto, 1988). Also plotted are isotherms after Lindsley (1983).

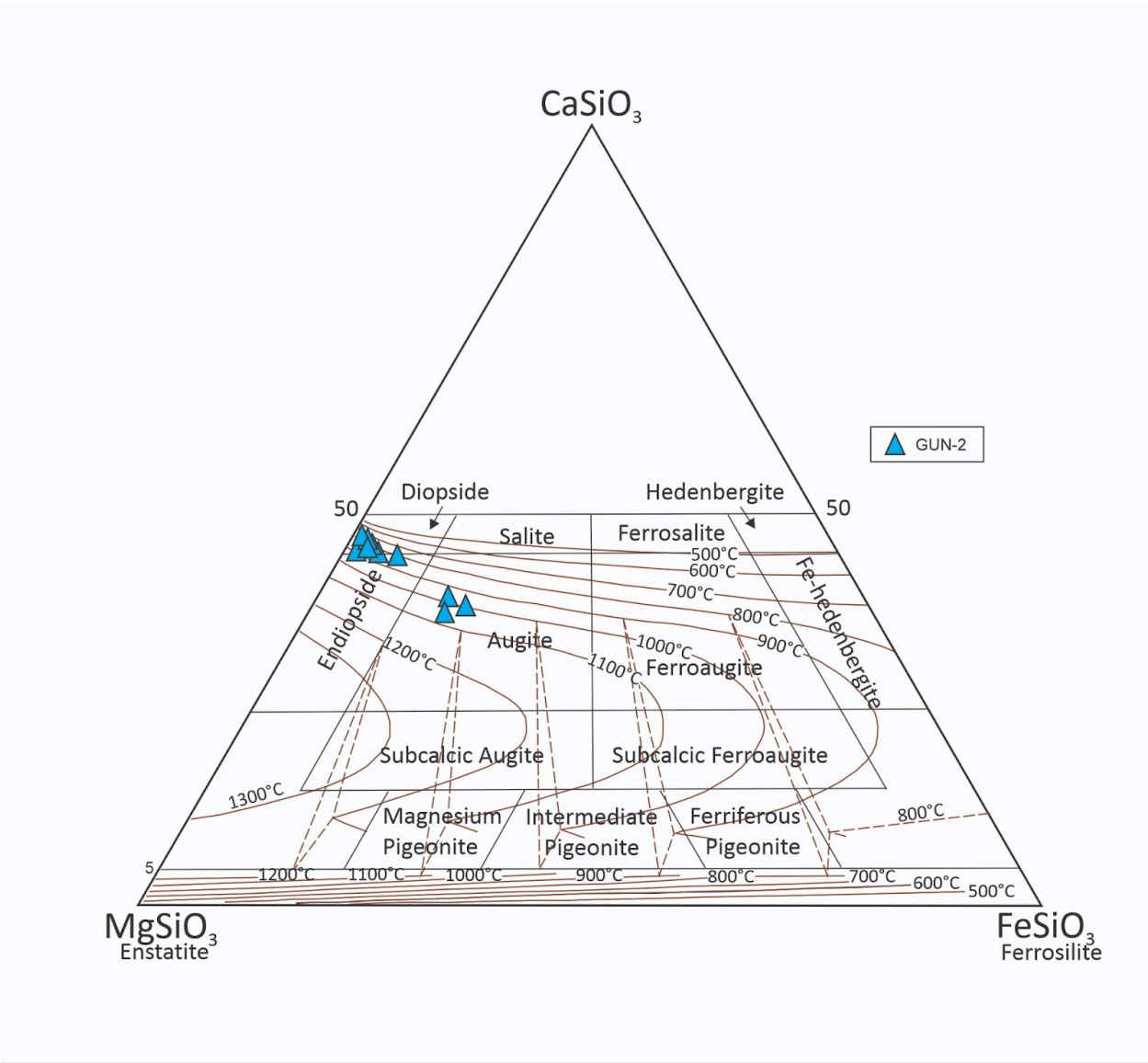

Fig. 21: Lava tube core (GUN 2) plotted on the Hess's triangle (MgSiO3-FeSiO3-CaSiO3) for pyroxene (nomenclature after Morimoto, 1988). Also plotted are isotherms after Lindsley (1983).

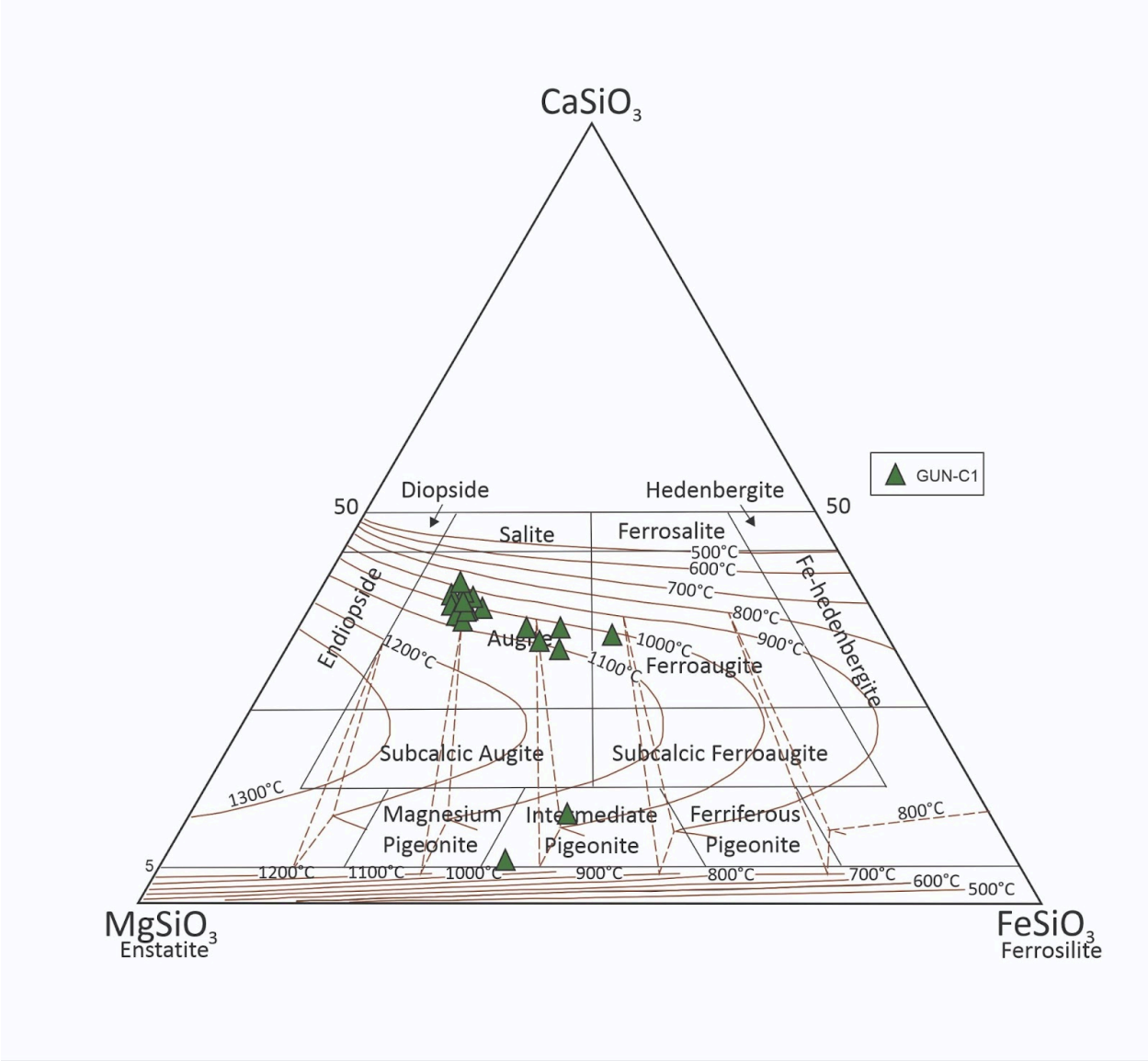

Fig. 22: Lava tube cognate (GUN C1) plotted on the Hess's triangle (MgSiO3-FeSiO3-CaSiO3) for pyroxene (nomenclature after Morimoto, 1988). Also plotted are isotherms after Lindsley (1983). Measurements taken across the boundary separating the cognate and the matrix

3.4.2 Plagioclase

The variation in CaO content is high for the plagioclases in the sample collected from the northern levee (GUN 1.1) (5.89–12.47 wt%) while the MgO ranges from 0-0.21 wt%.The SiO_2 content in GUN 1.1 ranges from 53.52 to 66.62 wt% and Al_2O_3 displays a larger range from 12.75 to 28.21 wt% as seen in Supplementary Table 2. The Na_2O values range from 0.23 to 5.53 wt% and K_2O from 0.12 to 1.55 wt%. The Mg# range is 48.83 - 92.95 while the overall composition ranges in $An_{48.83\text{-}92.95}Ab_{15.14\text{-}47.03}Or_{0.63\text{-}4.23}$ (Fig. 23). The large range suggests that the plagioclases crystallised from magmas with differing levels of evolution.

The plagioclases from GUN 2, or the representative core sample as recorded in Supplementary table 3, contain CaO range from 11.17- 14.39 wt% and MgO in the lower range from 0.08- 0.22 wt%. The plagioclases have Na_2O ranging from 3.51- 5.18 wt% and low K_2O 0.11- 0.74 wt%. The sample also contains Al_2O_3 25.61- 30.3 wt% and SiO2 50.44- 54.39 wt%. The Mg# range from 54.06 to 68.94. The composition is in the range of $An_{54.06\text{-}68.94}Ab_{30.43\text{-}44.41}Or_{0.63\text{-}4.23}$ (Fig. 24).

The plagioclases in GUN 6 (sample representative of southern levee) have CaO ranges from 7.24 to 14.01 wt% and MgO content 0.02 - 0.17 wt%. Meanwhile the SiO_2 concentrations are 48.09 - 63.48 wt% and Al_2O_3 concentrations are from 12.98 to 29.71 wt%. Na_2O content varies between 0.04 to 6.39 wt%, with K_2O ranging between 0.1 and 0.81 wt%. Mg# values vary from 40.45 to 97.42 in Supplementary table 1. The overall composition of the plagioclase varies within $An_{40.25\text{-}97.42}Ab_{0.97\text{-}54.97}Or_{1.02\text{-}7.10}$ (Fig. 25). Again, this large variation may be due to magmatic mixing or variable crystallisation processes.

The plagioclases from GUN C1 (the cognate sample collected from the core of the structure) shows CaO values range from 9.48 to 13.14 wt% and MgO range from 0.05- 0.76 wt%. The sample shows SiO_2 values from 50.88 to 57.01 wt%, with Al_2O_3 varying between 26.37 and 29.05 wt%. Na_2O values are higher than other samples ranging between 4 and 6.11 wt% while K_2O remains low (0.17–0.51 wt%). The Mg# ranges from 44.38 to 100. The overall plagioclase composition varies between $An_{44.82\text{-}63.52}Ab_{35.19\text{-}52.29}Or_{0.97\text{-}2.87}$ (Fig. 26). However this is a compilation of 18 spot measurements that does not differentiate between cognate and surrounding matrix. If we differentiate the measurements on basis of generation, then the large grained plagioclases from cognates are measured as SiO_2 (50.88 - 56.22 wt%), Al_2O_3 (26.86-29.05 wt%), CaO (10.21 - 13.14 wt%), MgO (0.06–0.33 wt%), Na_2O (4 - 5.83 wt%), K_2O (0.17-0.32 wt%), with Mg# ranging from 48.29 to 63.52 as seen in Supplementary table 3. The composition ranges within $An_{48.29\text{-}63.52}Ab_{35.19\text{-}49.90}Or_{0.97\text{-}1.80}$. The finer grained matrix plagioclases measure as SiO_2 (51.11 to 57.01 wt%), Al_2O_3 (26.37- 28.71 wt%), CaO (9.48–12.72 wt%), Na_2O (4.1 - 6.11 wt%), K_2O (0.22 - 0.51 wt%) while Mg# ranges from 44.38 to 100 as seen in Supplementary table 4. The overall plagioclase composition ranges in $An_{44.83\text{-}100}Ab_{36.44\text{-}52.29}Or_{1.24\text{-}2.87}$ (Fig. 26).

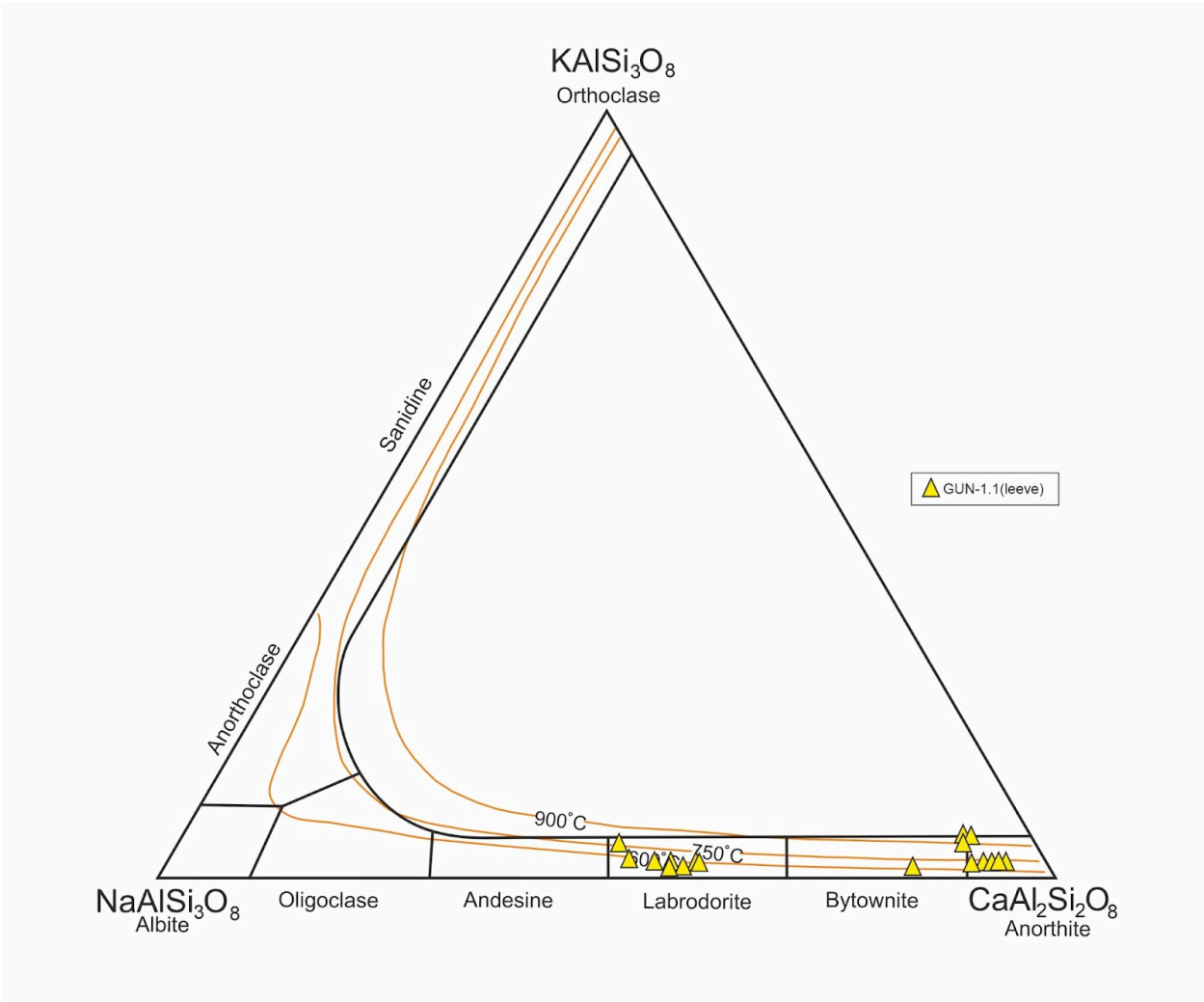

Fig. 23: Northern levee (GUN 1.1) samples plotted on plagioclase ternary diagram (NaAlSi3O3-KAlSi3O8-CaAl2Si3O8) for samples from the Gunjale tube

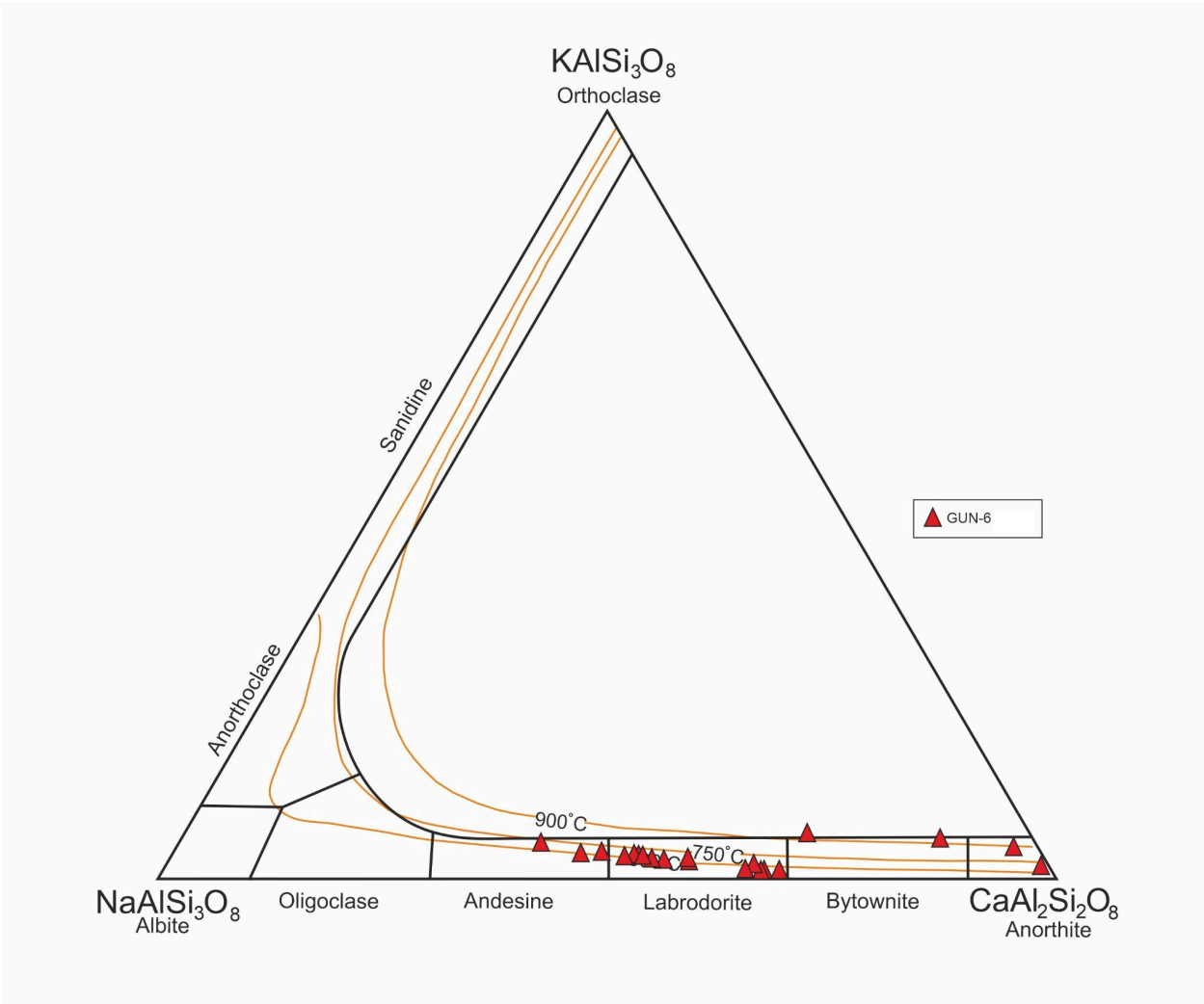

Fig. 24: Southern levee (GUN 6) samples plotted on the plagioclase ternary diagram (NaAlSi3O3-KAlSi3O8-CaAl2Si3O8) for samples from the Gunjale tube

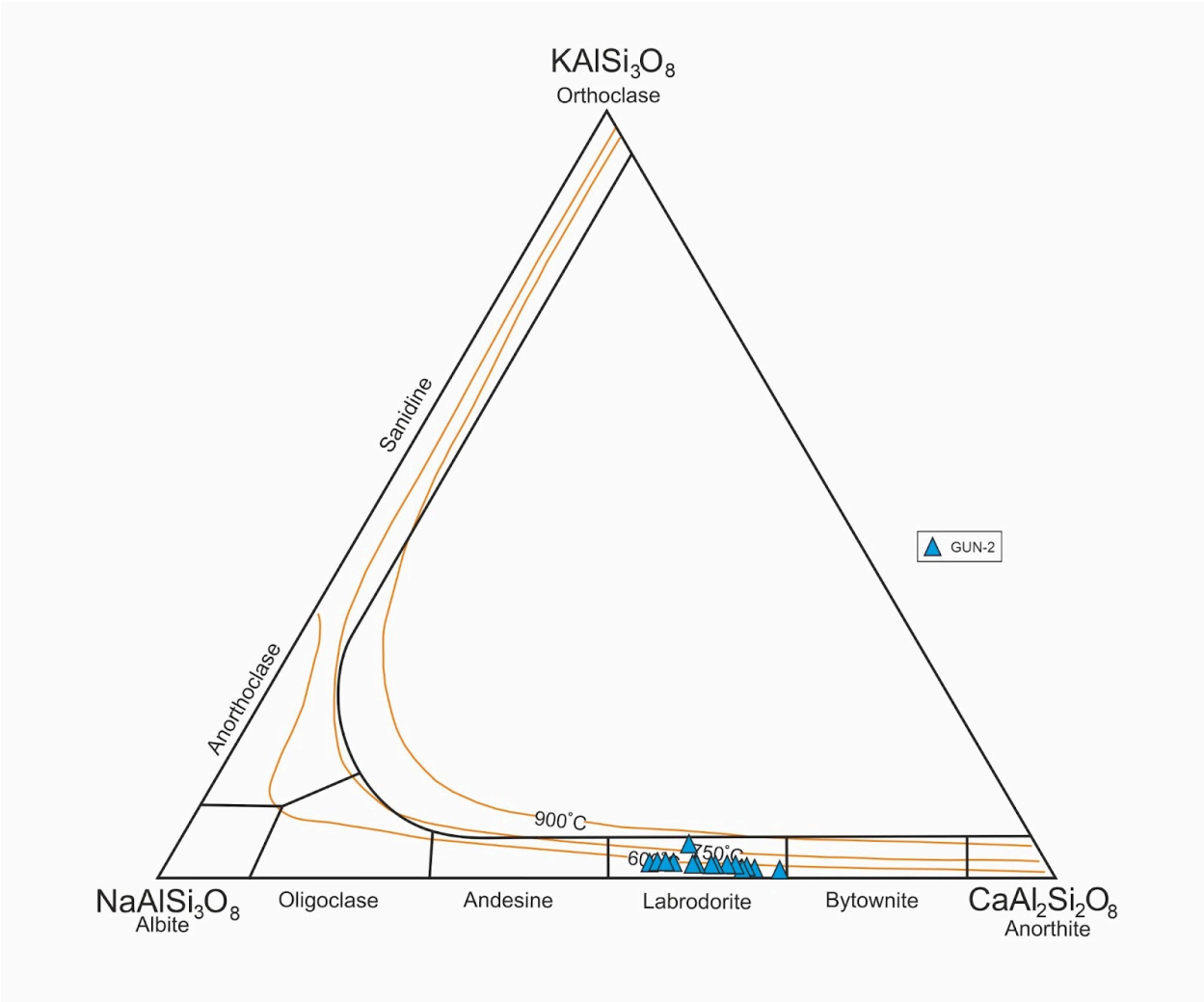

Fig. 25: Lava tube core (GUN 2) plotted on plagioclase ternary diagram (NaAlSi3O3-KAlSi3O8-CaAl2Si3O8) for samples from the Gunjale tube.

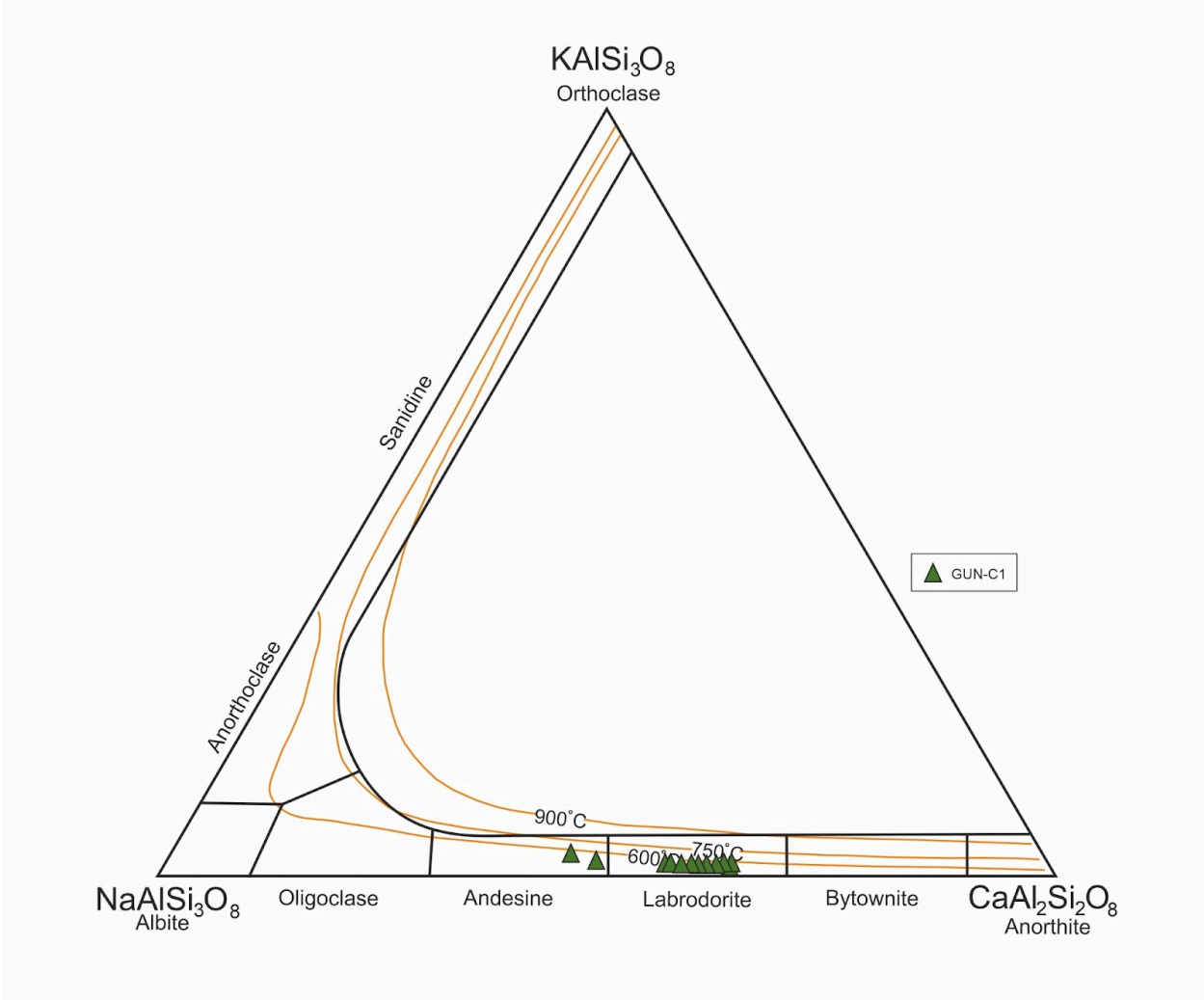

Fig. 26: Plagioclase ternary diagram (NaAlSi3O3-KAlSi3O8-CaAl2Si3O8) for cognate sample (GUN-C1) from the Gunjale tube.

3.4.3 Opaques

All the spinel data is recorded in Supplementary table 11. In GUN 1.1 spinels (Fig. 27), the FeO concentration does not vary much across measurements (32.26-33.86%), with Fe_2O_3 displaying similar behaviour (60.32% - 63.22%) with some TiO_2 variations (4.52-5.82%). SiO_2 varies within 0.01% - 0.04%, Cr_2O_3 only goes up to 0.03%, and Al_2O_3 varies from 0.62% - 0.74%. MgO, CaO, and MnO values are respectively 1.97%- 2.11%, 0.04%- 0.07%, and 0.31%-0.79%. The Mg# varies from 10.143 to 11.091.

The ilmenites display similar behaviour with TiO_2 (38.44% - 40.45%), FeO (31.34% - 32.53%), and Fe_2O_3 (27.44% - 30.18%). MgO content varies from 1.08%- 2.16%, CaO content varies from 0.01%- 0.05%, and MnO varies from 0.04% -0.61%. These samples have low SiO_2 (0.02%- 0.15%), Al_2O_3 (0.3%- 2.78%) and Cr_2O_3 up to 0.14%. The Fe_2O_3 values imply some oxidation,

there is some titanomagnetite crystallisation, but the crystallisation conditions are relatively homogeneous.

In GUN 2 spinels, the FeO concentrations does not vary a lot (34.46% - 37.05%) and moderate variation in Fe_2O_3 (50.92% - 56.66%) but the TiO_2 is relatively enriched compared to GUN 1.1 (8.88% - 12.03%). GUN 2 contains Cr_2O_3 up to 0.07%, SiO_2 only up to 0.07% with Al_2O_3 in the range of 0.58%- 1.05% suggesting ferroilmenite composition. The MgO, CaO, and MnO values are respectively 3.36%-4.46%, 0.02%-0.52%, and 0.34%-0.59%. The Mg# is in the range of 15.834- 20.119.

The ilmenites display similar trends of TiO_2 (42.38% - 43.20%), FeO (32.27% - 33.38%), and Fe_2O_3 (23.42% - 25.35%). MgO content varies from 2.51%-2.71%, CaO content varies from 0.05%-0.14%, and MnO is in the range of 0.11%-0.21%. Ilmenites have low SiO_2 (0.05%-0.15%), Al_2O_3 up to (1.09%-1.33%), and Cr_2O_3 up to 0.3%.The MgO appears to be higher than other samples. The core appears to be slightly less oxidised than the Northern Levee and the presence of titanium oxides is higher here.

Spinels (magnetite) in GUN 6 display more extreme values with FeO (32.95% - 42.45%), Fe_2O_3 (42.57% - 61.02%) and TiO_2 (5.07% - 15.46%).. The spinels contain Cr_2O_3 only up to 0.03%, SiO_2 in the range of 0.04%- 8.7%, with Al_2O_3 between 0.63% -3.06%. The MgO, CaO, and MnO ranges are respectively 1.33%- 2.66%, 0.07%-0.97%, and 0.48% -0.6%. The Mg# is in the range of 5.641- 13.826.

All the ilmenite data is recorded in the Supplementary table 12.The ilmenites in GUN 6 exhibit a very wide range of concentrations TiO_2 (18.59% - 43.35%) , FeO (12.20% - 38.44%), Fe_2O_3 and (18.21% - 69.21%). SiO_2 values go up to 6.51%, Cr_2O_3 goes up to 0.08%, Al_2O_3 ranges from 1.02% to 2.59%. The spot measurements also record the concentrations of MgO(2.05%- 2.63%), MnO (0.26%- 0.49%), and CaO (0.06%-0.31%).
The significant variation in Fe^{2+} and Fe^{3+} may imply differential cooling or an alteration process. The variation in TiO_2 points to the former.

Spinels (magnetite) in GUN C1 display the largest range in FeO (31.41% - 40.99%) and Fe_2O_3 (42.09% - 68.42%) with a few abnormally low TiO_2 values (0.17% - 9.41%) . Cr_2O_3 goes up to 0.03%, SiO_2 ranges 0.12%- 0.44% and Al_2O_3 varies between 0.07%-2.31%. The MgO, CaO, and MnO ranges are respectively 0.03%- 0.29%, 0.04%- 0.07%, and 0- 0.24%. This produces an Mg# in the 0.18- 1.339 range. The ilmenites on the other hand have extremely high TiO_2 (51.16% - 53.17%), high FeO (42.15% - 45.62%), and extremely low Fe_2O_3 (2.95% - 5.64%). Cr_2O_3 goes up to 0.15%, SiO_2 up to 0.15% with Al_2O_3 varying between 0.02%- 0.1%. MgO and MnO concentrations are respectively in the ranges of 0.61% - 2.67% and 0.41%- 0.67% while

CaO can go up to 0.13%. This can imply either highly reduced conditions of enrichment of Fe^{2+}. This heterogeneity can imply late stage crystallisation or alteration.

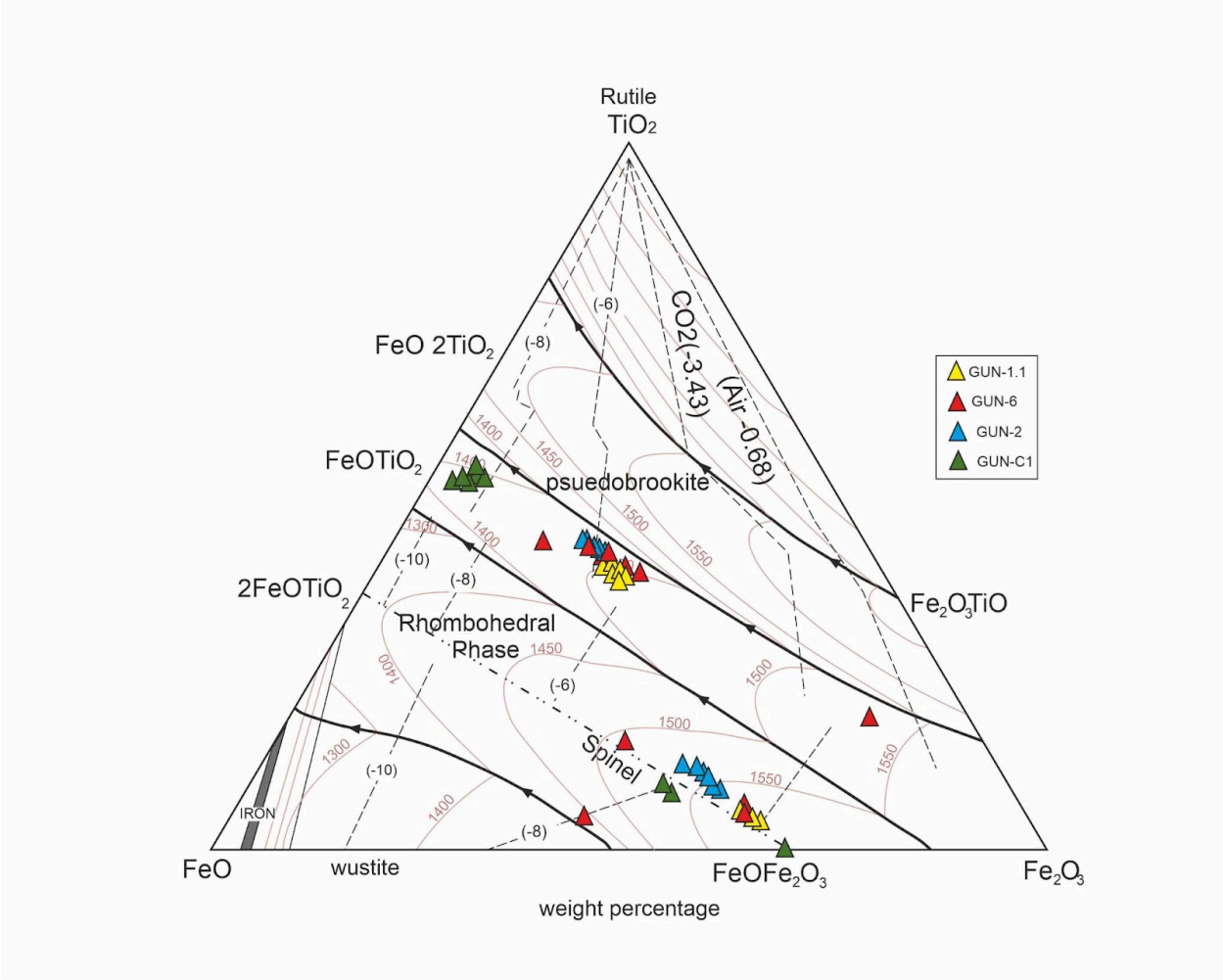

Fig. 27: All samples plotted on a TiO_2-Fe_2O_3-FeO diagram for spinel and ilmenites (modified after Buddington and Lindsley, 1964, Taylor 1964).

3.5 Temperature of Crystallisation

The simple mineralogy of plagioclase-pyroxene and opaques in the basalts from the Gunjale tube does not support a robust geothermobarometry. Hence we rely on the temperatures of the ternary diagrams depicted in figures to 19 to 27 (Lindsley, 1983) to make our conclusions. Based on the clinopyroxene compositions, the northern levee crystallised at a higher temperature (800 to 1300 °C) when compared to the southern levee (~500 to 1000 °C). As such the levees record the primary emplacement temperatures of the lava tube. The core of the lava tube contains secondary

lava or lavas that subsequently underwent cooling induced fractional crystallisation and therefore record a lower temperature range (~700 to 1100 °C). The cognate also records similar temperatures of ~900 to 1100 °C suggesting a similar thermal regime as that of the core. Similar observations on the temperature can be seen using plagioclases. In general the plagioclase compositions from the northern levee are more calcic and have higher temperature (~750 to 900 °C) in comparison to the southern levee (650 to 900 °C). The plagioclase from the lava tube core and cognate record significantly lower temperatures (650 to 750 °C).

Based on the oxide geothermometer (Lindsley, 1991), it can be concluded that magnetites form the core and cognates record a high temperature of 1500 to 1550 °C while the ilmenites form the core and cognates record slightly lower temperature of 1400 °C. Deuteric alteration of the magnetite to hematite occurred in the oxidised levee probably in the presence of magmatic water vapour at temperatures < 1000 °C.

3.6 Whole Rock Geochemistry

The major oxide data obtained by XRF analysis is presented in Supplementary Table 13 and plotted on various binary diagrams. The samples from the Gunjale lava tube are characterised by low SiO_2 (45.78 wt% - 48.98 wt%), moderate MgO (4.75 wt% - 5.42 wt%), higher FeO_T (14.47 wt% - 14.98 wt%, low Na_2O (2.01 wt% - 2.44 wt%), low K_2O (0.54 wt% - 1.18 wt%), and low P_2O_5 (0.21 wt% - 0.24 wt%). Based on the calculated normative mineral compositions using SINCLAS program of (Verma et al., 2002), few samples are olivine normative (olivine, ol- 3.33–10.88 wt%) while few are quartz-normative (quartz, q- 1.21–1.74 wt%) subalkaline tholeiite basalt (hypersthene, hy- 3.21–22.85 wt%).

In the TAS diagram of LeBas et al. (1986), all the samples from the present study plot in the field of subalkaline basalt (Fig. 28). In the Total alkali – total iron as FeO - MgO or AFM diagram (Fig. 29) the samples from the Gunjale tube plot in the tholeiite field of Kuno (1968) and Irvine and Baragar (1971). They show moderate Fe-enrichment trends (FeO_T/MgO- 2.69 to 3.15) that are typical of tholeiitic basalts for the Deccan Traps of the Western Ghats (field of 624 samples from Beane, 1988).

The Mg# [$(Mg^{+2}/(Mg^{+2}+Fe^{+2}))*100$] provides valuable information on the nature of melt and degree of fractional crystallisation and is therefore a sensitive petrogenetic indicator (Cox, 1980). In general, magmas with Mg# >70 and SiO_2 ≤50 wt% are considered primitive or primary magmas. In the present study, the Mg# for all basalts from the Gunjale tube varies from 40.01 to 43.85.Thus the lava forming the Gujale tube is not a primary magmas but a derived magmas that has undergone moderate degrees of fractionation (DI- 21.95 to 43.85).

Mg# was plotted against some sensitive major oxides (Fig. 30), interesting correlation is seen for the basalt samples from the Gunjale lava tube.

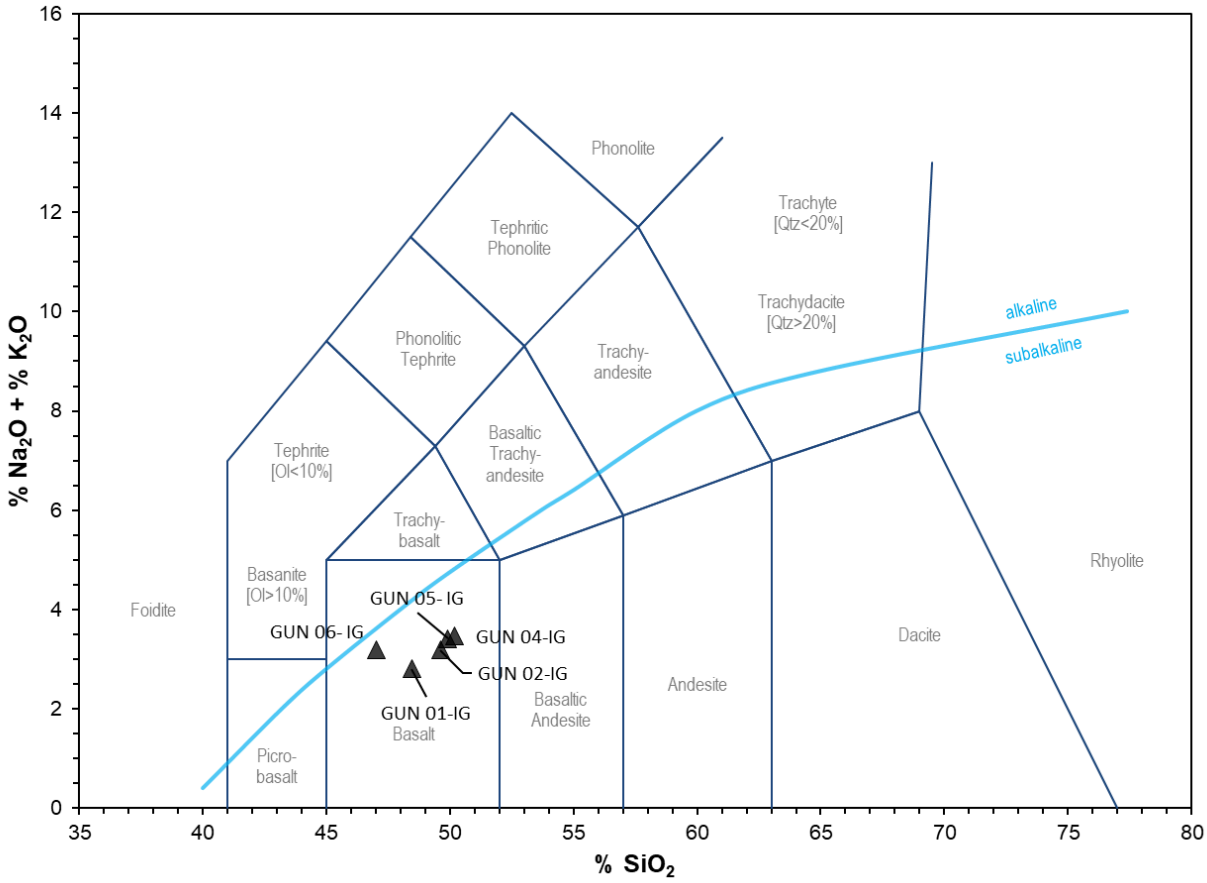

Fig. 28: Total Alkali Silica diagram (LeBas et al., 1986) for samples from the Gunjale lava tube. Boundary line between tholeiitic and alkali basalt fields after Macdonald and Katsura (1964). Values in Supplementary table 13.

TiO_2 increases across the samples (Fig. 30a), with GUN 5 displaying an anomalous low. The increase in TiO_2 with decreasing Mg# suggests that as titanium-bearing minerals crystallise early but were removed as ilmenites, later crystallisation of ilmenites stopped with reduced temperature leading to an enrichment of Ti in the more differentiated samples.

FeO remains relatively constant (despite the slope, see Fig. 30b), but there is a slight increase towards GUN 6. This can be indicative of late-stage iron enrichment in the magma as the mafic minerals (olivine and pyroxene) crystallise, leaving more Fe in the remaining melt.

SiO_2 values show a steady increase from GUN 1 to GUN 4, with a peak at 4, followed by slight decrease in GUN 5 and massive decrease in GUN 6 (Fig. 30c). As Mg# decreases (for levee samples) SiO_2 increases, which appears to be typical magmatic differentiation. SiO_2 is higher in

the core (47.68–48.98 wt%) compared to the levees, so the core may be more evolved magmatically.

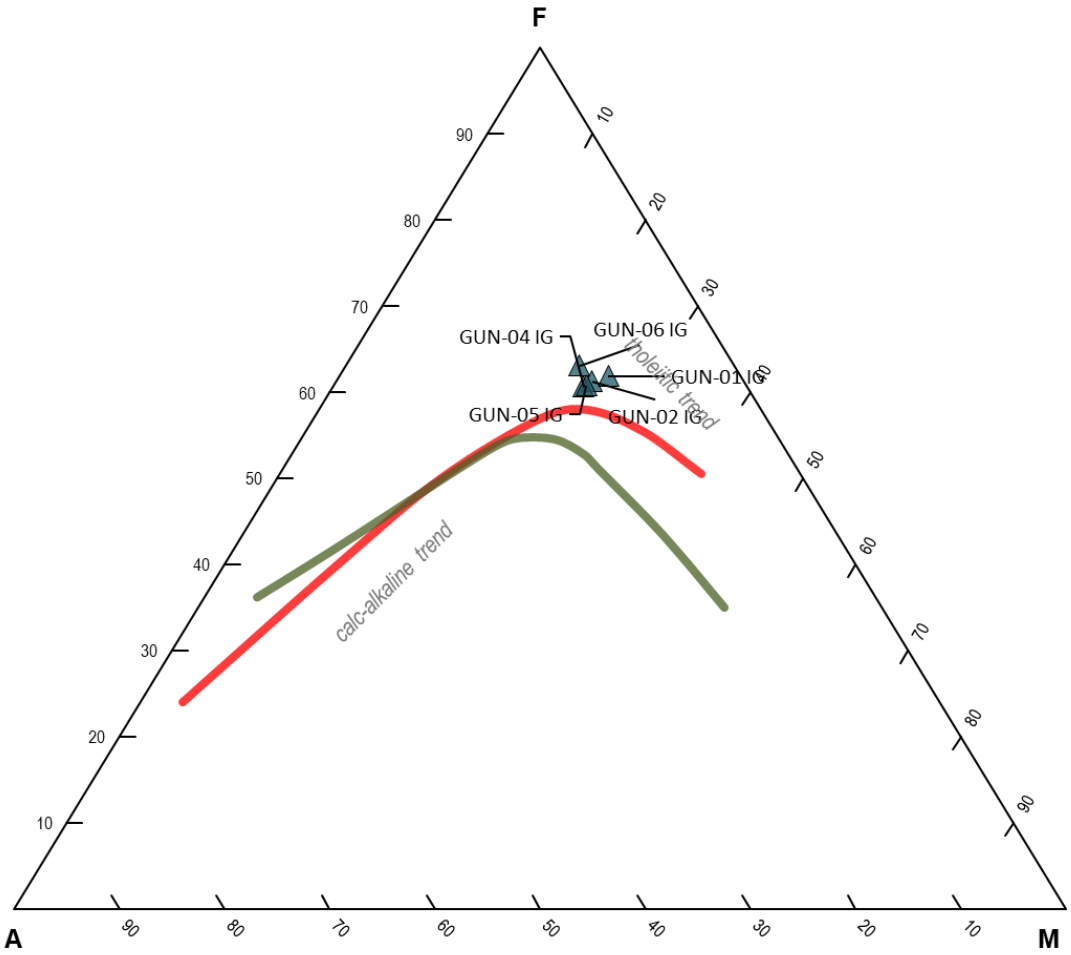

Fig. 29: AFM diagram for samples from the Gunjale lava tube. Boundary line between tholeiitic and calc-alkali basalt fields after Kuno (1968) and Irvine and Baragar (1971).

Al_2O_3 increases from GUN 1 to GUN 2 (Fig. 30d), decreases slightly by GUN 4 and GUN 5, and then increases sharply in GUN 6. The large increase with low Mg# may be attributed to plagioclase crystallising in GUN 6.

CaO decreases from GUN 1 to GUN 4, increases at GUN 5 then increases again at GUN 6 (Fig. 30e). Values can be low due to crystallisation of clinopyroxene and plagioclase which depletes

Ca from melt. The difference in GUN 5 and GUN 6 may be due to them belonging to a different flow or new influx of Ca rich material.

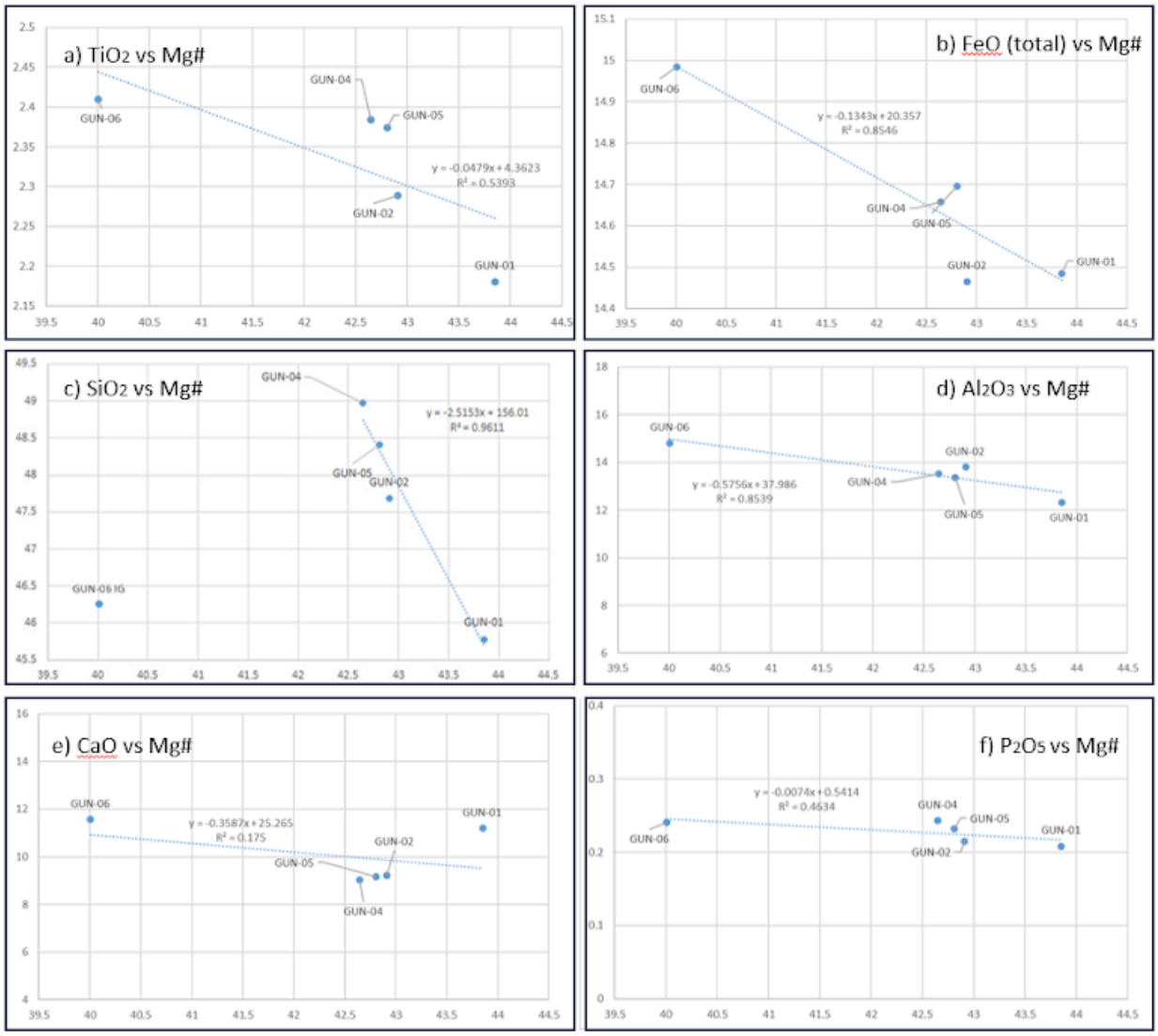

Fig. 30: Trends of various major oxides versus Mg number(Mg#) for the various samples from the lava tube

There is an inverse relationship between P_2O_5 and Mg# (Fig. 30f) - as the magma differentiates, Mg# decreases, while P_2O_5 increases in the melt. The core samples 02, 04 have higher P_2O_5 and lower Mg# compared to levee samples, so the core is more differentiated. GUN 6 appears most differentiated.

The variation in the oxide percentage vs. Mg# is similar for typical tholeiitic basalts from the Deccan Traps of the Western Ghats (field of 624 samples from Beane, 1988) indicating fractionation of olivine, pyroxene and possibly opaque oxides.

Conclusions

1. The Gunjale lava tube is a medium sized lava tube from the Deccan trap similar to those reported earlier in literature (Thorat 1996; Sharma and Vaddadi 1996; Misra 2002; Duraiswami et al., 2004; Pawar et al., 2016; Sen et al., 2011). It occurs in a compound pāhoehoe lava flows and is characterised by prominent levees formed by accreditation of breccias and lava lobes.

2. The northern levee is actually the preserved remnant of the lava flow composed of pāhoehoe sheets and lobes (from field observations). Hence, its texture is microporphyritic and interdental, similar to the basaltic flow that hosts the tube. This basalt is highly oxidised suggesting subaerial emplacement and deuteric alteration of the original magnetite to hematite.

3. The southern levee displays an accretion of vesicular crust and breccia. The texture is exceptionally microporphyritic with large lanceolate opaque suggesting under cooling. Under cooling is the cooling of a melt below the temperature of crystallisation of a mineral. If undercooling is significant, it delays nucleation and only results in quick crystallisation which leads to small crystals. Undercooling also causes opaques to crystallise in melts with higher concentration of FeO and TiO_2- suppression of formation of other minerals means the opaques can get larger.

4. The core of the lava is massive and contains spherical to elongated plagioclase-clinopyroxene cognates (1 cm to as large as 15 cm).

5. The textures in the cognate are extremely coarse grained indicating slow cooling possibly due to accumulation in a magma chamber. They were subsequently then brought into the magmatic plumbing system and then into the lava tube where they are preserved in the core. The core of the lava tube was insulated, resulting in a coarser cumulus texture.

6. Compositionally, the clinopyroxenes from the Gunjale tube levees range from diopside-augite to pigeonite while those from the care are diopside-augite. The cognates show augite-pigeonite compositions.

7. There is considerable variation in the plagioclase compositions across the Gunjale lava tube. In the northern levee the plagioclases are of anorthite-bytownite-labradorite composition while those from the southern levee have andesine in addition. Plagioclase from the core has labradorite composition while the cognates show labradorite-andesine

8. The opaque minerals are predominantly magnetite that has been converted into The cognates contain ilmenite.

9. The textural and compositional diversity (Monterio et al., 2024) seen in the samples from the various parts of the tube can be attributed to fractional crystallisation in a differential cooling regime.

10. Based on the clinopyroxene compositions, the northern levee record the primary emplacement temperatures of the lava tube and crystallise at a higher temperature (800 to 1300 °C) when compared to the southern levee (~500 to 1000 °C). The core on the other hand underwent cooling induced fractional crystallisation and therefore recorded a lower temperature (~700 to 1100 °C). The cognate also records similar temperatures of ~900 to 1100 °C suggesting a similar thermal regime as that of the core.

11. In general the plagioclase compositions from the northern levee are more calcic and have higher temperature (~750 to 900 °C) in comparison to the southern levee (650 to 900 °C). The plagioclase from the lava tube core and cognate record significantly lower temperatures (650 to 750 °C).

12. Based on the oxide geothermometer (Lindsley, 1964), it can be concluded that magnetites form the core and cognates record a high temperature of 1500 to 1550 °C while the ilmenites form the core and cognates record slightly lower temperature of 1400 °C. Deuteric alteration of the magnetite to hematite occurred in the oxidised levee probably in the presence of magmatic water vapour at temperatures < 1000 °C.

13. In the present study, the Mg# for all basalts from the Gunjale tube varies from 40.01 to 43.85.Thus the lava forming the Gujale tube is not a primary magmas but a derived magmas that has undergone moderate degrees of fractionation (DI- 21.95 to 43.85).

14. Based on the calculated normative mineral compositions using SINCLAS program of (Verma et al., 2002), few samples are olivine normative (olivine, ol- 3.33–10.88 wt%) while few are quartz-normative (quartz, q- 1.21–1.74 wt%) subalkaline tholeiite basalt (hypersthene, hy- 3.21–22.85 wt%).

15. In the TAS diagram of LeBas et al. (1986), all the samples from the present study plot in the field of subalkaline basalt). In the AFM diagram the samples from the Gunjale tube plot in the tholeiite field of Kuno (1968) and Irvine and Baragar (1971).

16. They show moderate Fe-enrichment trends (FeO_T/MgO- 2.69 to 3.15) that are typical of tholeiitic basalts for the Deccan Traps of the Western Ghats (field of 624 samples from

Beane, 1988).

17. The variation in the oxide percentage vs. Mg# is similar for typical tholeiitic basalts from the Deccan Traps of the Western Ghats (field of 624 samples from Beane, 1988) indicating fractionation of olivine, pyroxene and possibly opaque oxides.

18. These above observations combined with section 3.4, we can build a cooling history of the system. It appears that the two leeve and the tube interior have different thermal regions and cooling histories.The tube formed initially as a preferred conduit within the lava flow field. Further investigation can clarify the emplacement and history further.

References

Ahmednagar- District. Groundwater Survey and Development Agency, Government of Maharashtra https://gsda.maharashtra.gov.in/en-ahmednagar-district/

Anastasiia Hevko, Polka dot grunge seamless vector pattern. Circle brushstrokes and empty rounded shapes. (Hand drawn abstract ink background) (2021) https://www.istockphoto.com/vector/polka-dot-grunge-seamless-vector-pattern-gm1295673178-389330227

Beane JE, Turner CA, Hooper PR, Subbarao KV, Walsh JN (1986) Stratigraphy, composition and form of Deccan basalts, Western Ghats, India. Bull Volcanol 48:61–83

Beane, J.E. (1988) Flow stratigraphy, chemical variation and petrogenesis of Deccan flood basalts from the Western Ghats, India. Ph.D. Diss., Washington State Univ., Pullman.

Blanford, W. T. (1867) Traps of Western and Central India. Mem. Geo. Sur. Ind.,,6, Pt. 2, p. 147.

Bondre, N.R., Dole, G., Phadnis, V.M., Duraiswami, R.A. and Kale, V.S. (2000) Inflated pāhoehoe lavas from western uplands of the Deccan Volcanic Province. *Curr. Sci.,* v. 78 (8), pp. 1004-1007.

Bondre, N.R., Duraiswami, R.A. and Dole, G. (2004) A brief comparison of lava flows from the Deccan Volcanic Province and the Columbia-Oregon Plateau Flood Basalts: Implications for models of flood basalt emplacement. In: Sheth, H.C., Pande, K. (Eds.), Magmatism in India through Time. *Proc. Indian Acad. Sci. (Earth Planet. Sci.)*, v. 113, no. 4, pp. 809-817.

Buddington, A.F., Lindsley, D.H. (1964) Iron titanium oxide minerals and synthetic equivalents. Jour. Petrol., v. 5, pp. 310-357.

Callegaro, S. (2023). Recurring volcanic winters during the latest cretaceous: sulfur and fluorine budgets of deccan traps lavas. Science Advances, 9(40). https://doi.org/10.1126/sciadv.adg8284

Courtillot VE, Bease J, Vandamme D, Montigny R, Jaeger JJ, Cappetta H (1986) The Deccan flood basalts at the Cretaceous–Tertiary boundary? Earth Planet Sci Lett 80: 361–374

Cox KG, Hawkesworth CJ (1985) Geochemical stratigraphy of the Deccan Traps at Mahabaleshwar, Western Ghats, India, with implications for open system magmatic processes. J Petrol 26:355–377

Cox, K.G. (1980) A Model for Flood Basalt Volcanism. Jour. Petrol., v. 21(4), pp. 629-650.

Deer, W. A., Howie, R. A., Zussman, J. (1992). *An Introduction to the Rock-Forming Minerals* (2nd ed.). London: Longman.

Deshmukh, S.S. (1988) Paleomagnetic Variations in Compound Flows of Deccan Traps and Their Significance. In: Subbarao, K.V., Ed., Deccan Flood Basalts, No. 10, Geological Society of India, Bangalore, 305-319.

Dole, G., Bondre, N.R., Duraiswami, R.A. and Kale, V.S. (2002) Discussion on: arterial system of lava tubes and channels within Deccan Volcanics of Western India by K.S. Misra. *Jour. Geol. Soc. India*, v. 60, pp. 597-600.

Dole, G., Bondre, N.R., Duraiswami, R.A. and Kale, V.S. (2002) Discussion on: arterial system of lava tubes and channels within Deccan Volcanics of Western India by K.S. Misra. Jour. Geol. Soc. India, v. 60, pp. 597-600.

Droop, G. T. R. (1987) A general equation for estimating Fe^{3+} concentrations in ferromagnesian silicates and oxides from microprobe analyses, using stoichiometric criteria. Mineralogical Magazine, 51 (361) 431-435 doi:10.1180/minmag.1987.051.361.10

Duraiswami, R.A., Bondre, N.R., and Dole, G. (2004) A Possible lava tube system in a hummocky lava flow at Daund, western Deccan Volcanic Province, India. In: Sheth, H.C., Pande, K. (Eds.), Magmatism in India through Time. *Proc. Indian Acad. Sci. (Earth Planet. Sci.)*, v. 113, no. 4, pp. 819-829.

Duraiswami, R.A., Bondre, N.R., Dole, G., Phadnis, V.M. (2002) Morphology and structure of Flow-lobe tumuli from the western Deccan Volcanic Province, India. *Jour. Geol. Soc. India*, v. 60, pp. 57-65.

Duraiswami, R.A., Bondre, N.R., Dole, G., Phadnis, V.M., and Kale, V.S. (2001) Tumuli and associated features from the western Deccan Volcanic Province, India. *Bull. Volcanol*., v. 63, no. 7, pp. 435-442.

Duraiswami, R.A., Bondre, N.R., Managave, S. (2008) Morphology of rubbly pāhoehoe (simple) flows from the Deccan Volcanic Province: implications for style of emplacement. *Jour. Volcanol. Geotherm. Res.,* v. 177, pp. 822-836.

Duraiswami, R.A., Dole, G., Bondre, N.R. (2005) The Songir Structure: Inflated Lava Flow Or Tube? *Jour. Geol. Soc. India,* v. 65, pp. 357-365.

Duraiswami, R.A., Dole, G., Bondre, N.R., (2003) Slabby pāhoehoe from the western Deccan Volcanic Province: evidence for incipient pāhoehoe-aa transitions. *Jour. Volcano. Geotherm. Res.,* v. 121, pp. 195-217.

Duraiswami, R.A., Purva Gadpallu, Tahira N. Shaikh and Neha Cardin (2014) pāhoehoe-a'a transitions in the lava flow fields of the western Deccan Traps, India- implications for emplacement dynamics, flood basalt architecture and volcanic stratigraphy. *Jour. Asian Earth Science*. 84, pp. 146–166

Duraiswami, R.A., Sheth, H.C., Gadpallu, P., Youbi, N., Chella, El. H. (2020) A simple recipe for red bole formation in continental flood basalt provinces: weathering of flow-top and flow-bottom breccias. Arabian Jour. Geosciences. v. 13, 953, pp.1-14 https://doi.org/10.1007/s12517-020-05973-9

Eric A.K. Middlemost, Iron oxidation ratios, norms and the classification of volcanic rocks, Chemical Geology, Volume 77, Issue 1, 1989, Pages 19-26, ISSN 0009-2541, https://doi.org/10.1016/0009-2541(89)90011-9.

Gadpallu, Purva (2021)Volcanic facies architecture of lava flows and associated interflow horizon from Pune-Daund section, western Deccan Traps, India. Unpublished Ph.D. thesis, Savitribai Phule Pune University

Glaze, L. S., Anderson, S. W., Stofan, E. R., Baloga, S. M., Smrekar, S. E. (2005). Statistical distribution of tumuli on pahoehoe flow surfaces: analysis of examples in hawaii and iceland and potential applications to lava flows on mars. Journal of Geophysical Research: Solid Earth, 110(B8). https://doi.org/10.1029/2004jb003564

Godbole SM, Rana RS, Natu SR (1996) Lava stratigraphy of Deccan basalts of western Maharashtra. Gondwana Geol Mag Spl 2:125–134

Graphic by Trista Thornberry-Ehrlich (Colorado State University) after USGS graphic by Bruce Rogers.Lava-Tube Formation; Petroglyph National Monument https://www.nps.gov/npgallery/GetAsset/E6C1ED32-C8EC-4226-806D-CB37D65E6729

H. Rollinson (1996) Using Geochemical Data. Addison Wesley Longman, Harlow, Essex, pg 352

Hoyer, Patrick & Haase, Karsten & Regelous, Marcel & Fluteau, Frédéric. (2023). Systematic and Temporal Geochemical Changes in the Upper Deccan Lavas: Implications for the Magma Plumbing System of Flood Basalt Provinces. Geochemistry Geophysics Geosystems. 24. 10.1029/2022GC010750.

Hurwitz, D.M., Head, J.W., Hiesinger, H., Lunar sinuous rilles: Distribution, characteristics, and implications for their origin (2013) Planetary and Space Science, 79-80 (80), pp. 1-38. , https://doi.org/10.1016/j.pss.2012.10.01

Irvine, T.N., Baragar W.R.A. (1971) A guide to the chemical classification of the common rocks. Can. J. Earth Sci., v. 8, p. 523-548.

Jay, A. and Widdowson, M. (2008). Stratigraphy, structure and volcanology of the SE Deccan continental flood basalt province: Implications for eruptive extent and volumes. Journal of the Geological Society. 165. 10.1144/0016-76492006-062.

Kale, V.S, Bodas M., Chatterjee, P., Pande, K. (2020) Emplacement history and evolution of the Deccan Volcanic Province, India. Episodes, v. 43 (1), pp. 278-299.

Keszthelyi, L. and Self, S. (1998). Some physical requirements for the emplacement of long basaltic lava flows. Journal of Geophysical Research 103: doi: 10.1029/98JB00606. issn: 0148-0227.

Krishnamurthy, P. (2020) The Deccan Volcanic Province (DVP), India: A Review (Part 1: Areal Extent and Distribution, Compositional Diversity, Flow Types and Sequences, Stratigraphic Correlations, Dyke Swarms and Sills, Petrography and Mineralogy). Journal of Geological Society of India, *96*(1), 9–35. https://doi.org/10.1007/s12594-020-1501-5

Krishnan, MS (1960) Geology of India & Burma. 6th Edition, 680 p.

Kumar, K. V., Laxman, M. B., Nagaraju, K. (2017) Mantle source heterogeneity in continental mafic large igneous provinces: insights from the panjal, rajmahal and deccan basalts, india. Geological Society, London, Special Publications, 463(1), 87-116. https://doi.org/10.1144/sp463.5

Kuno, H. (1968) Differentiation of basaltic magmas. In: Hess H.H., and Poldervaart A., eds., Basalts, New York, Wiley Interscience, v. 2, pp. 623-688.

LeBas, M.J., LeMaitre, R.V., Strekeisen, A., Zanettin, B. (1986) Himicheskaya klassifikaciya vulkanicheskih porod, osnovannaya na diagramme obshchego soder-zhaniya shchelochi i kremnezema (TAS). Chemical classification of volcanic rocks based on total alkali and silica (TAS) chart. Jour. Petrol, v. 27, pp. 745-750.

Lindsley, D.H. (1983) Pyroxene thermometry. Amer. Miner., v. 68, pp. 477-493.

Lindsley, D.H. (1991) Oxide mineralogy: Oxide Minerals: Petrologic and Magnetic Significance. Reviews in Mineralogy Series v. 25(xiv), pp. 509 Washington: Mineralogical Society of America.

Macdonald, G. A. and Katsura, J. (1964) Chemical Composition of Hawaiian lavas, Jour. Petrology v5, p 82-133

Misra, K.S. (2002) Arterial system of lava tubes and channels within Deccan volcanics of western India. Journal Geological Society of India, v.59, pp. 115−124

Mittal, Tushar & Richards, Mark & Fendley, Isabel. (2021). The Magmatic Architecture of Continental Flood Basalts I: Observations From the Deccan Traps. Journal of Geophysical Research: Solid Earth. 126. 10.1029/2021JB021808.

Monterio, A.J., Duraiswami, R.A., Mittal. T., Pujari, S.J., Low, U. and Absar, A. (2021) Cooling history and emplacement dynamics within rubbly lava flows, southern Deccan Traps: insights from textural variations and crystal size distributions. Bull. Volcanol., v. 83 (11), pp. 1- 23.

Monterio, A.J., Mittal. T., Duraiswami, R.A., Self, S. (2024) The crystallization of Continental Flood Basalt (CFB) lavas: insights from textural studies. Jour. Petrol., v.65(6), egae082.

Morgan JW (1972) Plate motions and deep mantle convection. Geol Soc Am Bull 132:7–22

Morimoto N., Fabries J., Ferguson A.K., Ginzburg I. V., Ross M., Seifert F.A., Zussman J., Aoki K., Gottardi D. (1988) Nomenclature of pyroxenes. American Mineralogist, v. 62, pp. 53-62.

Pakulla, J.J., Jansen M.W., Duraiswami, R.A., Gadpallu, Purva; Jentzsch, C., Tusch, J., Braukmüller, N., Wombacher, F.,Münker, C. (2023) Trace elements and Sr-Nd-Hf-Pb isotopes indicate a multi-magma chamber system beneath the Deccan Volcanic Province, India. Chemical Geology, v. 640, pp.121749.

Pakulla, J.J., Tusch, J., Hasenstab-Dübeler, E., Ravindran, A., Jansen M.W., Gadpallu, P., Duraiswami, R.A., Münker C. (2024) The spatio-temporal evolution of 182W and 142Nd in the Deccan-La Réunion plume. Earth Plat Sci. Lett., EPSL-D-24-01318 Compositional diversity of clinopyroxenes plotted in the Hess's triangle ($MgSiO_3$-$FeSiO_3$-$CaSiO_3$) for pyroxene (nomenclature after Morimoto, 1988). Also plotted are isotherms after Lindsley (1983).

Paul R. Renne *et al.* State shift in Deccan volcanism at the Cretaceous-Paleogene boundary, possibly induced by impact. *Science* 350,76-78(2015).DOI:10.1126/science.aac7549

Pawar, N., Katikar, A., Vaddadi, S., Shinde, S., Rajaguru, S. N., Joshi, S., … & Eksambekar, S. (2016). The genesis of a lava cave in the deccan volcanic province (Maharashtra, India). International Journal of Speleology, 45(1), 51-58. https://doi.org/10.5038/1827-806x.45.1.1935

Ragini Kumari, Jyotirmoy Mallik, Garima Shukla (2024) Tectonomagmatic evolution of Pune – Nasik Deccan Dykes: Insights from structure and dimension scaling. Tectonophysics, v. 891, 230539, ISSN 0040-1951, https://doi.org/10.1016/j.tecto.2024.230539

Saha, G., Kumar, Vivek, Chaubey, Dipak K. Rai, Shyam S. (2023) Cryptic Magma Chamber in the Deccan Traps Imaged Using Receiver Functions and Surface Wave Dispersion. Geophys. Res. Letter., v. 50 (23), e2023GL105359.

Schoene, B., Samperton, K. M., Eddy, M. P., Keller, G., Adatte, T., Bowring, S. A. & Gertsch, B. (2015). U-pb geochronology of the deccan traps and relation to the end-cretaceous mass extinction. Science, 347(6218), 182-184. https://doi.org/10.1126/science.aaa0118

Schoene,B.,Eddy,M.P.,Samperton,K.M.,Keller,C.B.,Keller,G.,Adatte,T.&Khadri,S.F.(2019).U-Pbconstraint sonpulsederup-tionoftheDeccantrapsacrosstheend-cretaceousmassextinc-tion.SummarizedProceedingsf orthePeriodFromandaDirectoryofMembersasof363,862–866.https://doi.org/10.1126/science.aau2422.

Schumacher, J. (1991) Empirical Ferric Iron Corrections: Necessity, Assumptions, and Effects on Selected Geothermobarometers. Mineralogical Magazine - MINER MAG. 55. 3-18. 10.1180/minmag.1991.055.378.02.

Sen, B., Sabale, AB,Sukumaran, PV (2012) Lava channel of Khedrai Dam, Northeast of Nasik in Western Deccan volcanic province: Detailed morphology and evidences of channel reactivation. Jour. Geol. Soc. India, v. 80(3), pp. 314-328.

Sen, G. (2001) Generation of Deccan Trap magmas. Proc. Indian Acad. Sci. (Earth Planet. Sci.), v. 110 (4), pp. 409–431

Sen, G. (2001). Generation of deccan trap magmas. Journal of Earth System Science, 110(4), 409-431. https://doi.org/10.1007/bf02702904

Sharma, R.K., and Vaddadi, S. (1996) Report on lava tubes/ channels from Deccan Volcanic Province. Gondwana Geological Society, Special Publication, v. 2, pp. 457–460.

Sheth, H. (2005). Were the deccan flood basalts derived in part from ancient oceanic crust within the indian continental lithosphere?. Gondwana Research, 8(2), 109-127. https://doi.org/10.1016/s1342-937x(05)71112-6

Sheth, H., Duraiswami, R.A., Vivek Ghule, Anmol Naik, Tarulata Das (2022) Flood basalt structures and textures as guides to cooling histories and palaeoclimates: the Deccan Traps of Saurashtra, western India. Geological Magazine, v. 159, pp. 1415–1436.

Sheth, H.C., Ray, J.S., Senthil Kumar, P., Duraiswami, R.A., Chatterjee, R.N., Gurav, T. (2011) Recycling of flow-top breccia crusts into molten interiors of flood basalt lava flows: Field and geochemical evidence from the Deccan Traps. In: Ray, J., Sen, G., Ghosh, B. (Editors), *Topics in Igneous Petrology*, pp.161-180. Springer.

Sheth, H.C., Mahoney, J.J., Chandrasekharam, D. 2004) Geochemical stratigraphy of Deccan flood basalts of the Bijasan Ghat section, Satpura Range, India, Journal of Asian Earth Sciences, Volume 23, Issue 1, Pages 127-139, ISSN 1367-9120,

Sisolekar, S., Duraiswami, R.A., Monterio, A. (2021) A Rheological, Mathematical, and Statistical Comparison of Lunar Rilles and Terrestrial Lava Tubes. 52nd Lunar and Planetary Science Conference, 2021

Sprain, C. J., Renne, P. R., Vanderkluysen, L., Pande, K., Self, S., & Mittal, T. (2019). The eruptive tempo of deccan volcanism in relation to the cretaceous-paleogene boundary. Science, 363(6429), 866-870. https://doi.org/10.1126/science.aav1446

Subbarao K V and Hooper P R 1988 Reconnaissance map of the Deccan Basalt Group in the Western Ghats, India;Mem. Geol. Soc. India 10 321–332

Taylor, R.W. (1964) Phase equilibria in the system FeO-Fe2O3-TiO2 at 1300°C. Amer. Mineral., v. 49, pp. 1016-1030.

Thorat P.K. (1996) Occurrence of lava channels and tubes in the western part of Deccan Volcanic Province. In: Deshmukh, S.S., and Nair, K.K.K. (Eds) Deccan Basalts, Gondwana Geological Society, Special Publication, v. 2, pp. 449−456.

Vanderkluysen, L., Mahoney, JJ., Hooper, PR., Sheth, HC. (2011) The feeder system of the Deccan Traps (India): insights from dike geochemistry. Journal of Petrology, v. 52 (2), pp. 315-343.

Vanderkluysen,L., Mahoney, J.J., Peter R Hooper, Hetu C Sheth, Ranjini Ray (2011) The feeder system of the Deccan Traps (India): insights from dike geochemistry. Journal of Petrology, v. 52(2), pp. 315-343.

Verma, S.P., Torres-Alvarado, I.S., Sotelo-Rodríguez, Z.T. (2002) SINCLAS: standard igneous norm and volcanic rock classification system, Comp. Geosci., v. 28 (5), pp. 711-715.

Walker GPL (1987) Pipe vesicles in Hawaiian basalt lavas: their origin and potential as paleoslope indicators. Geolog33

Supplementary

Table 1: Mineral chemistry (wt%), stoichiometry (8 oxygens) and composition of plagioclases.

GUN 6 Plagioclase														
	1	2	3	4	5	6	7	8	15	16	17	23	24	26
SiO2	52.01	48.09	51.42	51.85	55.43	60.06	63.48	59.08	55.12	56.53	54.15	58.49	62.17	51.45
TiO2	0.06	0.07	0.09	0.06	0.1	0	0	0.02	0.09	0.14	0.1	0.07	0.08	0.06
Al2O3	29.7	27.48	29.37	29.67	27.28	15.13	17.04	12.98	27.41	26.73	28.33	25.21	16.08	29.71
V2O3	0	0	0	0	0	0	0	0	0	0	0	0	0	0
Cr2O3	0.05	0	0.03	0	0	0.03	0.01	0	0.03	0	0	0.03	0	0.03
Fe2O3	0	0	0	0	0	0	0	0	0	0	0	0	0	0
FeO	0.6	0.57	0.49	0.48	0.86	0.06	0.02	0.01	0.76	0.86	0.76	1.03	0.56	0.57
NiO	0.06	0.04	0.02	0.07	0	0	0.03	0	0	0	0	0	0	0.02
MgO	0.16	0.14	0.17	0.07	0.05	0.08	0.12	0.07	0.08	0.09	0.09	0.06	0.1	0.17
CaO	13.81	13.5	14.01	13.57	11.03	7.8	8.23	7.24	10.8	10.25	12.21	8.51	7.6	13.97
MnO	0.01	0.06	0.11	0	0	0	0.05	0	0.01	0	0	0	0.01	0
Na2O	3.68	3.32	3.72	3.71	5.17	0.13	0.52	0.04	5.12	5.81	4.62	6.39	1.48	3.72
K2O	0.18	0.18	0.24	0.29	0.47	0.28	0.55	0.1	0.52	0.61	0.41	0.81	0.66	0.18
P2O5	0	0.02	0.01	0	0.07	0	0	0.03	0.01	0	0	0.02	0.08	0
ZnO	0	0	0.01	0	0	0.03	0.17	0	0	0	0.11	0	0.11	0
CoO	0	0	0	0	0	0	0	0	0	0	0	0	0	0
BaO	0.04	0.01	0	0.05	0	0	0	0.02	0.01	0.01	0	0.01	0	0
Si	2.363	2.347	2.349	2.367	2.498	3.449	3.359	3.581	2.495	2.523	2.439	2.616	3.314	2.345
Ti	0.002	0.003	0.003	0.002	0.003	0	0	0.001	0.003	0.005	0.003	0.002	0.003	0.002
Al(IV)	0	0	0	0	0	0	0	0	0	0	0	0	0	0
Al(VI)	1.59	1.581	1.581	1.596	1.449	1.024	1.063	0.927	1.462	1.406	1.504	1.329	1.01	1.596
V	0	0	0	0	0	0	0	0	0	0	0	0	0	0
Cr	0.002	0	0.001	0	0	0.001	0	0	0.001	0	0	0.001	0	0.001
Fe3	0.014	0.023	0.019	0.012	0.019	0	0	0	0.018	0.032	0.029	0.031	0	0.022
Fe2	0.009	0	0	0.006	0.013	0.003	0.001	0.001	0.01	0	0	0.007	0.025	0
Ni	0.002	0.002	0.001	0.003	0	0	0.001	0	0	0	0	0	0	0.001
Mg	0.011	0.01	0.012	0.005	0.003	0.007	0.009	0.006	0.005	0.006	0.006	0.004	0.008	0.012
Ca	0.672	0.706	0.686	0.664	0.533	0.48	0.467	0.47	0.524	0.49	0.589	0.408	0.434	0.682
Mn	0	0.002	0.004	0	0	0	0.002	0	0	0	0	0	0	0
Na	0.324	0.314	0.33	0.328	0.452	0.014	0.053	0.005	0.449	0.503	0.403	0.554	0.153	0.329
K	0.01	0.011	0.014	0.017	0.027	0.021	0.037	0.008	0.03	0.035	0.024	0.046	0.045	0.01
P	0	0.001	0	0	0.003	0	0	0.002	0	0	0	0.001	0.004	0
Zn	0	0	0	0	0	0.001	0.007	0	0	0	0.004	0	0.004	0
Co	0	0	0	0	0	0	0	0	0	0	0	0	0	0
Ba	0.001	0	0	0.001	0	0	0	0	0	0	0	0	0	0
O_calc	7.993	7.978	7.972	7.994	7.99	8.944	8.846	9.041	7.991	7.962	7.98	7.984	8.728	7.976
Mg#	53.862	100	100	42.697	20.208	70.386	91.45	92.581	34.115	100	100	35.569	24.146	100
An	66.767	68.45	66.627	65.781	52.661	93.205	83.758	97.424	52.213	47.696	57.981	40.451	68.691	66.791
Ab	32.196	30.463	32.014	32.545	44.667	2.811	9.577	0.974	44.794	48.924	39.701	54.965	24.207	32.185

Or	1.036	1.087	1.359	1.674	2.672	3.984	6.665	1.602	2.993	3.38	2.318	4.584	7.103	1.025

GUN 6 Plagioclase (contd.)									
	27	28	42	43	44	45	46	47	48
SiO2	52.02	55.06	57.05	55.42	53.83	54.49	50.4	54.66	55.15
TiO2	0.06	0.08	0.04	0.14	0.08	0.08	0.11	0.06	0.09
Al2O3	29.49	27.73	26.42	27.51	28.89	27.7	25.84	27.5	27.5
V2O3	0	0	0	0	0	0	0	0	0
Cr2O3	0.02	0	0	0	0	0.06	0	0.04	0
Fe2O3	0	0	0	0	0	0	0	0	0
FeO	0.61	0.72	0.6	0.72	0.79	0.84	0.83	0.9	0.82
NiO	0	0	0.01	0.13	0	0	0.02	0	0
MgO	0.16	0.09	0.02	0.09	0.12	0.1	0.09	0.06	0.12
CaO	13.49	11.55	9.75	10.72	11.76	11.33	11.36	11.34	10.91
MnO	0.02	0.08	0	0.07	0	0	0.06	0.03	0
Na2O	3.9	4.93	6.08	5.44	4.52	5.12	4.32	5.11	5.26
K2O	0.22	0.43	0.56	0.52	0.58	0.49	0.43	0.46	0.55
P2O5	0	0.01	0	0	0.04	0	0.02	0	0
ZnO	0	0	0	0.01	0.01	0	0	0.11	0
CoO	0	0	0	0	0	0	0	0	0
BaO	0	0	0	0	0.01	0	0.01	0	0
Si	2.367	2.478	2.554	2.484	2.426	2.459	2.448	2.468	2.482
Ti	0.002	0.003	0.001	0.005	0.003	0.003	0.004	0.002	0.003
Al(IV)	0	0	0	0	0	0	0	0	0
Al(VI)	1.581	1.471	1.394	1.453	1.535	1.473	1.479	1.463	1.459
V	0	0	0	0	0	0	0	0	0
Cr	0.001	0	0	0	0	0.002	0	0.001	0
Fe3	0.023	0.021	0.022	0.027	0.03	0.032	0.034	0.034	0.031
Fe2	0	0.006	0	0	0	0	0	0	0
Ni	0	0	0	0.005	0	0	0.001	0	0
Mg	0.011	0.006	0.001	0.006	0.008	0.007	0.007	0.004	0.008
Ca	0.658	0.557	0.468	0.515	0.568	0.548	0.591	0.549	0.526
Mn	0.001	0.003	0	0.003	0	0	0.002	0.001	0
Na	0.344	0.43	0.528	0.473	0.395	0.448	0.407	0.447	0.459
K	0.013	0.025	0.032	0.03	0.033	0.028	0.027	0.026	0.032
P	0	0	0	0	0.002	0	0.001	0	0
Zn	0	0	0	0	0	0	0	0.004	0
Co	0	0	0	0	0	0	0	0	0
Ba	0	0	0	0	0	0	0	0	0
O_calc	7.981	7.989	7.972	7.964	7.985	7.962	7.976	7.965	7.97
Mg#	100	51.424	100	100	100	100	100	100	100
An	64.826	55.043	45.52	50.605	57.004	53.497	57.695	53.655	51.747

Ab	33.915	42.517	51.367	46.472	39.648	43.748	39.704	43.753	45.147	
Or	1.259	2.44	3.113	2.923	3.348	2.755	2.6	2.592	3.106	

Table 2: Mineral chemistry (wt%), stoichiometry (8 oxygens) and composition of plagioclases.

GUN 1.1 Plagioclase														
	1	2	3	4	5	6	7	8	9	10	11	22	23	24
SiO2	56.14	53.53	53.54	54.77	53.52	58.15	57.55	63.35	61.49	60.56	61.19	54.07	54.41	55.33
TiO2	0.08	0.11	0.09	0.09	0.09	0	0	0	0	0	0	0.06	0.06	0.05
Al2O3	26.9	27.76	28.01	28.21	28.17	16.29	15.85	16.05	13.05	12.75	13.73	27.87	27.93	28.06
V2O3	0	0	0	0	0	0	0	0	0	0	0	0	0	0
Cr2O3	0	0	0.04	0	0	0	0.04	0	0.01	0	0.05	0	0.03	0
Fe2O3	0	0	0	0	0	0	0	0	0	0	0	0	0	0
FeO	0.63	0.75	0.57	0.69	0.82	0.09	0	0.15	0	0	0.02	0.68	0.78	0.73
NiO	0.09	0.06	0	0.02	0	0.05	0	0.01	0	0.04	0.01	0	0.01	0
MgO	0.06	0.14	0.12	0.14	0.1	0	0.02	0.13	0.03	0	0.04	0.12	0.1	0.1
CaO	10.75	12.44	12.33	12.05	12.47	7.6	7.82	7.96	6.82	7.01	7.53	11.78	11.82	11.45
MnO	0.04	0	0	0.02	0.01	0.01	0	0.02	0	0.04	0	0.01	0	0
Na2O	5.46	4.58	4.56	4.84	4.6	0.39	0.42	0.36	0.3	0.26	0.23	4.95	4.95	5.17
K2O	0.41	0.32	0.33	0.26	0.32	0.45	0.35	0.43	0.12	0.12	0.13	0.26	0.35	0.35
P2O5	0.02	0	0.02	0	0.01	0.01	0.02	0	0.01	0	0.02	0.03	0.01	0
ZnO	0	0.01	0	0	0	0	0.04	0.15	0	0	0	0	0	0
CoO	0	0	0	0	0	0	0	0	0	0	0	0	0	0
BaO	0	0	0	0	0	0.19	0.21	0	0.03	0.03	0	0	0	0.01
Si	2.523	2.437	2.438	2.455	2.426	3.341	3.344	3.424	3.618	3.612	3.55	2.451	2.453	2.471
Ti	0.003	0.004	0.003	0.003	0.003	0	0	0	0	0	0	0.002	0.002	0.002
Al(IV)	0	0	0	0	0	0	0	0	0	0	0	0	0	0
Al(VI)	1.425	1.489	1.503	1.491	1.505	1.103	1.085	1.023	0.905	0.896	0.939	1.489	1.484	1.477
V	0	0	0	0	0	0	0	0	0	0	0	0	0	0
Cr	0	0	0.001	0	0	0	0.002	0	0	0	0.002	0	0.001	0
Fe3	0.022	0.029	0.022	0.026	0.031	0	0	0	0	0	0	0.026	0.029	0.027
Fe2	0.002	0	0	0	0	0.004	0	0.007	0	0	0.001	0	0	0
Ni	0.003	0.002	0	0.001	0	0.002	0	0	0	0.002	0	0	0	0
Mg	0.004	0.01	0.008	0.009	0.007	0	0.002	0.01	0.003	0	0.003	0.008	0.007	0.007
Ca	0.518	0.607	0.602	0.579	0.605	0.468	0.487	0.461	0.43	0.448	0.468	0.572	0.571	0.548
Mn	0.002	0	0	0.001	0	0	0	0.001	0	0.002	0	0	0	0
Na	0.476	0.404	0.403	0.421	0.404	0.043	0.047	0.038	0.034	0.03	0.026	0.435	0.433	0.448
K	0.024	0.019	0.019	0.015	0.019	0.033	0.026	0.03	0.009	0.009	0.01	0.015	0.02	0.02
P	0.001	0	0.001	0	0	0	0.001	0	0	0	0.001	0.001	0	0
Zn	0	0	0	0	0	0	0.002	0.006	0	0	0	0	0	0
Co	0	0	0	0	0	0	0	0	0	0	0	0	0	0
Ba	0	0	0	0	0	0.004	0.005	0	0.001	0.001	0	0	0	0
O_calc	7.989	7.974	7.984	7.986	7.97	8.855	8.852	8.902	9.05	9.04	9.004	7.974	7.971	7.978
Mg#	65.03	100	100	100	100	0	100	60.706	100	0	78.095	100	100	100

An	50.903	58.932	58.785	57.06	58.889	85.958	86.92	87.248	90.863	91.954	92.951	55.969	55.769	53.952
Ab	46.786	39.263	39.342	41.474	39.311	7.982	8.448	7.141	7.233	6.172	5.138	42.56	42.264	44.084
Or	2.312	1.805	1.873	1.466	1.799	6.06	4.632	5.612	1.904	1.874	1.911	1.471	1.966	1.964

GUN 1.1 Plagioclase (contd.)					
	25	26	27	28	29
SiO2	56.55	62.61	64.29	66.62	63.4
TiO2	0.09	0	0	0	0.01
Al2O3	26.71	16.46	13.53	13.62	13.97
V2O3	0	0	0	0	0
Cr2O3	0.03	0	0	0.01	0
Fe2O3	0	0	0	0	0
FeO	0.77	0.07	0	0.01	0.08
NiO	0	0	0	0.05	0
MgO	0.07	0	0.06	0	0.21
CaO	10.39	7.76	5.89	6.93	6.54
MnO	0	0	0	0	0
Na2O	5.53	0.81	0.34	0.38	0.24
K2O	0.74	0.12	1.55	0.12	1.12
P2O5	0.03	0	0	0.03	0
ZnO	0	0	0	0	0
CoO	0	0	0	0	0
BaO	0	0.01	0.02	0.01	0.1
Si	2.531	3.399	3.6	3.658	3.554
Ti	0.003	0	0	0	0
Al(IV)	0	0	0	0	0
Al(VI)	1.409	1.053	0.893	0.881	0.923
V	0	0	0	0	0
Cr	0.001	0	0	0	0
Fe3	0.029	0	0	0	0
Fe2	0	0.003	0	0	0.004
Ni	0	0	0	0.002	0
Mg	0.005	0	0.005	0	0.018
Ca	0.498	0.451	0.353	0.408	0.393
Mn	0	0	0	0	0
Na	0.48	0.085	0.037	0.04	0.026
K	0.042	0.008	0.111	0.008	0.08
P	0.001	0	0	0.001	0
Zn	0	0	0	0	0
Co	0	0	0	0	0
Ba	0	0	0	0	0.002
O_calc	7.98	8.878	8.973	9.076	8.963

Mg#	100	0	100	0	82.392
An	48.829	82.829	70.532	89.298	78.72
Ab	47.03	15.646	7.368	8.861	5.228
Or	4.141	1.525	22.101	1.841	16.052

Table 3: Mineral chemistry (wt%), stoichiometry (8 oxygens) and composition of plagioclases.

GUN 2 Plagioclase														
	1	2	3	4	5	6	7	8	9	10	18	19	20	31
SiO2	53.69	51.35	53.31	51.63	53.64	51.77	51.48	50.44	52.14	52.56	54.17	51.48	52.82	50.88
TiO2	0.23	0.06	0.06	0.06	0.1	0.08	0.05	0.09	0.1	0.08	0.09	0.08	0.08	0.05
Al2O3	27.43	29.77	28.31	29.69	27.25	29.87	28.91	28.13	28.36	28.28	27.51	25.61	27.29	30.3
V2O3	0	0	0	0	0	0	0	0	0	0	0	0	0	0
Cr2O3	0	0	0	0.03	0	0	0	0	0	0.01	0.03	0	0	0
Fe2O3	0	0	0	0	0	0	0	0	0	0	0	0	0	0
FeO	2.25	0.89	1.41	0.6	1.51	0.58	1.03	1.17	1.8	1.59	1.87	1.86	1.52	0.55
NiO	0	0	0	0.07	0.01	0.01	0.02	0	0	0	0	0.06	0	0
MgO	0.11	0.12	0.22	0.17	0.13	0.15	0.13	0.13	0.11	0.11	0.16	0.17	0.11	0.17
CaO	11.89	13.73	12.83	13.61	11.86	13.66	13.26	12.73	12.82	12.5	11.7	11.17	11.76	14.39
MnO	0	0	0.01	0.05	0	0	0.02	0.08	0	0	0	0.02	0.02	0.02
Na2O	4.91	4.09	4.3	3.88	4.88	3.96	4.06	4.24	4.42	4.53	5.05	4.88	4.87	3.51
K2O	0.28	0.15	0.29	0.14	0.27	0.12	0.19	0.21	0.23	0.25	0.27	0.3	0.27	0.11
P2O5	0	0.01	0	0	0	0	0.01	0.02	0	0	0	0	0.01	0
ZnO	0	0.03	0	0	0	0.02	0	0.04	0	0	0.09	0	0.03	0.12
CoO	0	0	0	0	0	0	0	0	0	0	0	0	0	0
BaO	0	0	0.06	0	0	0.03	0	0.04	0.02	0	0.04	0	0	0
Si	2.422	2.328	2.408	2.35	2.442	2.348	2.361	2.355	2.372	2.39	2.435	2.442	2.425	2.317
Ti	0.008	0.002	0.002	0.002	0.003	0.003	0.002	0.003	0.003	0.003	0.003	0.003	0.003	0.002
Al(IV)	0	0	0	0	0	0	0	0	0	0	0	0	0	0
Al(VI)	1.458	1.591	1.507	1.593	1.462	1.597	1.563	1.548	1.52	1.516	1.457	1.432	1.477	1.626
V	0	0	0	0	0	0	0	0	0	0	0	0	0	0
Cr	0	0	0	0.001	0	0	0	0	0	0	0.001	0	0	0
Fe3	0.085	0.034	0.053	0.023	0.057	0.022	0.04	0.046	0.068	0.06	0.07	0.074	0.058	0.021
Fe2	0	0	0	0	0	0	0	0	0	0	0	0	0	0
Ni	0	0	0	0.003	0	0	0.001	0	0	0	0	0.002	0	0
Mg	0.007	0.008	0.015	0.012	0.009	0.01	0.009	0.009	0.007	0.007	0.011	0.012	0.008	0.012
Ca	0.575	0.667	0.621	0.664	0.579	0.664	0.652	0.637	0.625	0.609	0.563	0.568	0.578	0.702
Mn	0	0	0	0.002	0	0	0.001	0.003	0	0	0	0.001	0.001	0.001
Na	0.429	0.36	0.377	0.342	0.431	0.348	0.361	0.384	0.39	0.399	0.44	0.449	0.433	0.31
K	0.016	0.009	0.017	0.008	0.016	0.007	0.011	0.013	0.013	0.015	0.015	0.018	0.016	0.006
P	0	0	0	0	0	0	0	0.001	0	0	0	0	0	0
Zn	0	0.001	0	0	0	0.001	0	0.001	0	0	0.003	0	0.001	0.004
Co	0	0	0	0	0	0	0	0	0	0	0	0	0	0
Ba	0	0	0.001	0	0	0.001	0	0.001	0	0	0.001	0	0	0

O_calc	7.936	7.942	7.966	7.974	7.954	7.971	7.959	7.935	7.934	7.944	7.939	7.927	7.942	7.973
Mg#	100	100	100	100	100	100	100	100	100	100	100	100	100	100
An	56.328	64.43	61.221	65.439	56.443	65.144	63.648	61.638	60.78	59.537	55.293	54.867	56.283	68.941
Ab	42.093	34.732	37.131	33.76	42.027	34.175	35.266	37.151	37.921	39.045	43.188	43.378	42.178	30.431
Or	1.579	0.838	1.648	0.802	1.53	0.681	1.086	1.211	1.298	1.418	1.519	1.755	1.539	0.628

GUN 2 Plagioclase (contd.)					
	32	33	35	38	40
SiO2	54.39	51.72	52.14	52.9	53.93
TiO2	0.1	0.08	0.06	0.09	0.05
Al2O3	27.28	29.53	29.07	28.44	27.61
V2O3	0	0	0	0	0
Cr2O3	0	0	0.01	0.05	0
Fe2O3	0	0	0	0	0
FeO	1.46	0.8	1.01	1.45	1.74
NiO	0	0	0.03	0	0
MgO	0.12	0.08	0.11	0.11	0.15
CaO	11.41	13.48	13.13	12.57	11.91
MnO	0.02	0.09	0	0	0.02
Na2O	5.18	4.1	4.22	4.62	4.45
K2O	0.27	0.15	0.18	0.24	0.74
P2O5	0	0	0.04	0	0.01
ZnO	0	0	0.16	0	0
CoO	0	0	0	0	0
BaO	0	0	0	0	0
Si	2.458	2.35	2.367	2.391	2.439
Ti	0.003	0.003	0.002	0.003	0.002
Al(IV)	0	0	0	0	0
Al(VI)	1.453	1.582	1.556	1.515	1.472
V	0	0	0	0	0
Cr	0	0	0	0.002	0
Fe3	0.055	0.03	0.038	0.055	0.066
Fe2	0	0	0	0	0
Ni	0	0	0.001	0	0
Mg	0.008	0.005	0.007	0.007	0.01
Ca	0.552	0.656	0.639	0.609	0.577
Mn	0.001	0.003	0	0	0.001
Na	0.454	0.361	0.372	0.405	0.39
K	0.016	0.009	0.01	0.014	0.043
P	0	0	0.002	0	0
Zn	0	0	0.005	0	0
Co	0	0	0	0	0

Ba	0	0	0	0	0
O_calc	7.953	7.959	7.959	7.943	7.961
Mg#	100	100	100	100	100
An	54.062	63.953	62.581	59.247	57.139
Ab	44.415	35.2	36.398	39.406	38.634
Or	1.523	0.847	1.022	1.347	4.227

Table 4: Mineral chemistry (wt%), stoichiometry (8 oxygens) and composition of plagioclases.

GUN C1 Plagioclase (Cognate)										
	8	9	10	11	30	32	33	45	46	52
SiO2	52.89	51.08	52.58	52.85	53.2	52.85	53.41	52.55	56.22	50.88
TiO2	0.07	0.07	0.09	0.08	0.09	0.1	0.08	0.1	0.05	0.07
Al2O3	29.05	28.47	29.05	28.58	28.37	28.46	29.01	28.69	26.86	28.16
V2O3	0	0	0	0	0	0	0	0	0	0
Cr2O3	0	0.02	0	0	0.01	0	0	0.01	0	0
Fe2O3	0	0	0	0	0	0	0	0	0	0
FeO	0.81	0.76	0.71	0.81	0.68	0.69	0.82	1.06	0.72	0.63
NiO	0.02	0	0	0	0.01	0.07	0	0	0.02	0
MgO	0.12	0.13	0.12	0.13	0.11	0.15	0.1	0.33	0.06	0.17
CaO	13.14	12.98	12.95	12.61	12.54	12.52	12.71	12.69	10.21	13.08
MnO	0	0	0	0.01	0	0	0.02	0.02	0	0.03
Na2O	4.19	4	4.22	4.36	4.46	4.46	4.56	4.24	5.83	4.01
K2O	0.19	0.18	0.17	0.2	0.23	0.21	0.2	0.19	0.32	0.24
P2O5	0.01	0	0	0.01	0	0	0	0	0.05	0
ZnO	0.02	0.08	0	0.01	0	0	0.09	0	0	0
CoO	0	0	0	0	0	0	0	0	0	0
BaO	0	0	0.04	0	0	0	0	0	0.02	0
Si	2.393	2.376	2.391	2.409	2.422	2.41	2.4	2.391	2.525	2.377
Ti	0.002	0.002	0.003	0.003	0.003	0.003	0.003	0.003	0.002	0.002
Al(IV)	0	0	0	0	0	0	0	0	0	0
Al(VI)	1.549	1.561	1.557	1.535	1.522	1.529	1.536	1.538	1.422	1.551
V	0	0	0	0	0	0	0	0	0	0
Cr	0	0.001	0	0	0	0	0	0	0	0
Fe3	0.031	0.03	0.027	0.031	0.026	0.026	0.031	0.04	0.027	0.025
Fe2	0	0	0	0	0	0	0	0	0	0
Ni	0.001	0	0	0	0	0.003	0	0	0.001	0
Mg	0.008	0.009	0.008	0.009	0.007	0.01	0.007	0.022	0.004	0.012
Ca	0.637	0.647	0.631	0.616	0.612	0.612	0.612	0.619	0.491	0.655
Mn	0	0	0	0	0	0	0.001	0.001	0	0.001
Na	0.368	0.361	0.372	0.385	0.394	0.394	0.397	0.374	0.508	0.363
K	0.011	0.011	0.01	0.012	0.013	0.012	0.011	0.011	0.018	0.014
P	0	0	0	0	0	0	0	0	0.002	0
Zn	0.001	0.003	0	0	0	0	0.003	0	0	0

Co	0	0	0	0	0	0	0	0	0	0
Ba	0	0	0.001	0	0	0	0	0	0	0
O_calc	7.981	7.974	7.982	7.981	7.983	7.975	7.966	7.971	7.978	7.966
Mg#	100	100	100	100	100	100	100	100	100	100
An	62.725	63.525	62.292	60.806	60.044	60.074	59.953	61.635	48.294	63.426
Ab	36.195	35.426	36.734	38.046	38.645	38.726	38.924	37.267	49.903	35.188
Or	1.08	1.049	0.974	1.148	1.311	1.2	1.123	1.099	1.802	1.386

Table 5: Mineral chemistry (wt%), stoichiometry (8 oxygens) and composition of plagioclases.

GUN C1 Plagioclase (Matrix)								
	16	17	18	19	38	50	60	61
SiO2	52.96	53.71	51.9	51.11	52.56	52.91	52.53	57.01
TiO2	0.09	0.1	0.08	0.1	0.05	0.14	0.08	0.09
Al2O3	27.67	27.63	28.62	26.86	28.71	28.37	28.4	26.37
V2O3	0	0	0	0	0	0	0	0
Cr2O3	0	0	0	0.03	0	0.05	0	0
Fe2O3	0	0	0	0	0	0	0	0
FeO	0.77	1.05	1.5	0.88	0.74	1.31	0.85	0.73
NiO	0.03	0	0	0	0.01	0	0.06	0
MgO	0.09	0.06	0.76	0.1	0.09	0.06	0.07	0.05
CaO	11.96	11.74	12.68	11.82	12.72	12.23	12.26	9.48
MnO	0.03	0	0	0	0	0	0	0
Na2O	4.51	4.82	4.1	4.75	4.49	4.68	4.5	6.11
K2O	0.29	0.31	0.22	0.28	0.22	0.25	0.28	0.51
P2O5	0.03	0	0	0	0	0	0	0.04
ZnO	0	0.07	0.08	0.16	0.02	0	0.13	0
CoO	0	0	0	0	0	0	0	0
BaO	0	0	0	0.02	0	0	0	0
Si	2.442	2.448	2.36	2.408	2.393	2.401	2.404	2.556
Ti	0.003	0.003	0.003	0.004	0.002	0.005	0.003	0.003
Al(IV)	0	0	0	0	0	0	0	0
Al(VI)	1.504	1.484	1.534	1.492	1.54	1.517	1.532	1.393
V	0	0	0	0	0	0	0	0
Cr	0	0	0	0.001	0	0.002	0	0
Fe3	0.022	0.04	0.057	0.035	0.028	0.05	0.033	0.027
Fe2	0.008	0	0	0	0	0	0	0
Ni	0.001	0	0	0	0	0	0.002	0
Mg	0.006	0.004	0.052	0.007	0.006	0.004	0.005	0.003
Ca	0.591	0.573	0.618	0.597	0.62	0.595	0.601	0.455
Mn	0.001	0	0	0	0	0	0	0
Na	0.403	0.426	0.361	0.434	0.396	0.412	0.399	0.531
K	0.017	0.018	0.013	0.017	0.013	0.014	0.016	0.029
P	0.001	0	0	0	0	0	0	0.002

Zn	0	0.002	0.003	0.006	0.001	0	0.004	0
Co	0	0	0	0	0	0	0	0
Ba	0	0	0	0	0	0	0	0
O_calc	7.989	7.972	7.943	7.933	7.96	7.953	7.965	7.978
Mg#	44.376	100	100	100	100	100	100	100
An	58.436	56.357	62.275	56.966	60.264	58.247	59.122	44.835
Ab	39.877	41.871	36.439	41.427	38.495	40.335	39.27	52.293
Or	1.687	1.772	1.287	1.607	1.241	1.418	1.608	2.872

Table 6: Mineral chemistry (wt%), stoichiometry (on the basis 6 oxygens) and composition of pyroxenes

GUN 6 Pyroxene															
	10	11	18	19	20	21	25	35	36	40	49	50	51	52	54
SiO2	30.01	49.01	48.43	46.46	49.51	48.54	42.55	50.75	48.63	41.95	42.85	48.86	47.78	32.37	44.38
TiO2	3	0.91	1.38	1.25	1.12	1.47	3.43	1.26	0.99	11.48	1.16	1.22	1.34	1.53	2.6
Al2O3	10.8	3.67	2.84	2.25	2.27	2.4	13.47	3.11	2.87	16.99	4.61	1.99	3.4	4.22	11.36
V2O3	0	0	0	0	0	0	0	0	0	0	0	0	0	0	0
Cr2O3	0.03	0	0	0.02	0.03	0	0	0.15	0	0	0	0	0	0.23	0
Fe2O3	0	0	0	0	0	0	0	0	0	0	0	0	0	0	0
FeO	21.52	10.23	13	17.15	10.99	13.08	20.54	10.49	11.4	14.85	21.36	14.9	13.98	22.98	23.05
NiO	0	0.08	0	0.06	0.07	0	0	0	0	0	0	0	0	0.05	0.09
MgO	8.23	14.91	13.06	13.54	15.1	13.93	1.03	14.28	14.33	1.67	11.6	13.21	13.88	11.17	0.63
CaO	14.02	18.95	18	17.16	19.19	18.61	2.95	18.2	17.99	3.97	15.12	17.15	18.21	12.89	5.19
MnO	0.35	0.41	0.42	0.44	0.53	0.43	0.92	0.38	0.44	0.14	0.43	0.46	0.43	0.4	0.24
Na2O	0.29	0.52	0.66	0.55	0.57	0.55	3.04	0.64	0.6	5.78	0.61	0.54	0.57	0.39	0.44
K2O	0.03	0.04	0.04	0.07	0.06	0.05	3.73	0.1	0.07	1.19	0.1	0.03	0.03	0.07	1.37
P2O5	0.04	0	0.06	0.02	0	0	0	0.02	0.03	0	0	0.02	0	0	0.01
ZnO	0	0.05	0.01	0	0	0.09	0	0.08	0	0.05	0.15	0	0.03	0	0.02
CoO	0	0	0	0	0	0	0	0	0	0	0	0	0	0	0
BaO	0.01	0	0.01	0	0.02	0	0.04	0	0	0.02	0	0	0	0.05	0
Si	1.316	1.839	1.859	1.777	1.851	1.837	1.804	1.901	1.86	1.635	1.676	1.877	1.799	1.445	2.008
Ti	0.099	0.026	0.04	0.036	0.031	0.042	0.109	0.035	0.028	0.337	0.034	0.035	0.038	0.051	0.089
Al(IV)	0.558	0.161	0.129	0.101	0.1	0.107	0.196	0.099	0.129	0.365	0.212	0.09	0.151	0.222	0
Al(VI)	0	0.001	0	0	0	0	0.478	0.038	0	0.415	0	0	0	0	0.606
V	0	0	0	0	0	0	0	0	0	0	0	0	0	0	0
Cr	0.001	0	0	0.001	0.001	0	0	0.004	0	0	0	0	0	0.008	0
Fe3	0.634	0.149	0.118	0.314	0.179	0.177	0	0.035	0.139	0	0.42	0.126	0.218	0.815	0
Fe2	0.155	0.172	0.299	0.235	0.165	0.237	0.728	0.293	0.226	0.484	0.279	0.353	0.223	0.043	0.872
Ni	0	0.002	0	0.002	0.002	0	0	0	0	0	0	0	0	0.002	0.003
Mg	0.538	0.834	0.747	0.772	0.841	0.786	0.065	0.797	0.817	0.097	0.676	0.756	0.779	0.743	0.042
Ca	0.659	0.762	0.74	0.703	0.769	0.755	0.134	0.73	0.737	0.166	0.633	0.706	0.735	0.617	0.252
Mn	0.013	0.013	0.014	0.014	0.017	0.014	0.033	0.012	0.014	0.005	0.014	0.015	0.014	0.015	0.009
Na	0.025	0.038	0.049	0.041	0.041	0.04	0.25	0.046	0.044	0.437	0.046	0.04	0.042	0.034	0.039
K	0.002	0.002	0.002	0.003	0.003	0.002	0.202	0.005	0.003	0.059	0.005	0.001	0.001	0.004	0.079

P	0.001	0	0.002	0.001	0	0	0	0.001	0.001	0	0	0.001	0	0	0
Zn	0	0.001	0	0	0	0.003	0	0.002	0	0.001	0.004	0	0.001	0	0.001
Co	0	0	0	0	0	0	0	0	0	0	0	0	0	0	0
Ba	0	0	0	0	0	0	0.001	0	0	0	0	0	0	0.001	0
O_calc	5.683	5.926	5.941	5.843	5.911	5.911	6.025	5.982	5.931	6.113	5.79	5.937	5.891	5.593	6.341
Mg#	77.593	82.863	71.432	76.701	83.633	76.867	8.206	73.119	78.329	16.699	70.793	68.197	77.776	94.5	4.646
Wo	48.718	43.082	41.437	41.129	43.307	42.464	14.45	40.111	41.409	22.198	39.874	38.887	42.308	43.939	21.573
En	39.791	47.164	41.832	45.154	47.414	44.226	7.02	43.79	45.894	12.992	42.565	41.677	44.87	52.978	3.644
Fs	11.491	9.754	16.73	13.717	9.279	13.31	78.53	16.099	12.697	64.81	17.561	19.436	12.822	3.083	74.784

Table 7: Mineral chemistry (wt%), stoichiometry (on the basis 6 oxygens) and composition of pyroxenes

GUN 1.1 Pyroxene															
	12	13	14	15	16	17	30	31	32	33	36	37	38	39	46
SiO2	48.51	46.15	49.43	43.46	51.87	40.82	52.12	52.51	52.27	51.71	49.33	57.68	66.85	54.93	52.55
TiO2	1.05	1.07	0.94	1.03	0.74	0.77	0.79	0.68	0.65	0.89	0.11	0.05	0.01	0.09	0.75
Al2O3	1.86	1.88	1.96	1.77	1.46	1.3	1.24	1.62	1.41	2.39	0.67	0.84	1.62	1.17	1.77
V2O3	0	0	0	0	0	0	0	0	0	0	0	0	0	0	0
Cr2O3	0	0	0.13	0.05	0.1	0	0	0.33	0.23	0.27	0	0	0.01	0	0.33
Fe2O3	0	0	0	0	0	0	0	0	0	0	0	0	0	0	0
FeO	13.2	14.26	13.22	19.17	11.58	18.77	14.63	8.99	9.74	9.19	38.33	33.66	19.89	37.92	10.34
NiO	0.03	0	0	0.07	0.07	0	0.03	0.17	0	0	0	0.03	0.19	0.02	0.02
MgO	13.38	13.72	15.21	13.31	15.2	12.47	14.59	15.84	16.14	15.06	0.02	0.07	0.12	0.16	16.16
CaO	17.62	16.9	17.21	17.59	17	15.67	14.16	18.72	17.83	18.7	0.1	0.15	0.23	0.19	16.89
MnO	0.47	0.51	0.31	0.39	0.27	0.38	0.23	0.25	0.22	0.27	0	0.24	0.38	0.12	0.23
Na2O	0.74	0.88	0.12	0.49	0.18	0.72	0.16	0.2	0.19	0.21	0.05	0.04	0.06	0.05	0.2
K2O	0	0.02	0	0	0	0.01	0	0	0.01	0	0.03	0.04	0.03	0	0
P2O5	0.02	0.03	0	0	0.01	0.02	0	0	0	0.05	0	0	0.01	0	0
ZnO	0.05	0.04	0.01	0.18	0	0	0.15	0	0	0	0.09	0.24	0.02	0	0
CoO	0	0	0	0	0	0	0	0	0	0	0	0	0	0	0
BaO	0.01	0	0	0	0	0.01	0	0.01	0	0	0	0.02	0.04	0	0
Si	1.879	1.812	1.879	1.695	1.968	1.705	2.005	1.961	1.964	1.947	2.389	2.632	3.091	2.476	1.966
Ti	0.031	0.032	0.027	0.03	0.021	0.024	0.023	0.019	0.018	0.025	0.004	0.002	0	0.003	0.021
Al(IV)	0.085	0.087	0.088	0.081	0.032	0.064	0	0.039	0.036	0.053	0	0	0	0	0.034
Al(VI)	0	0	0	0	0.033	0	0.056	0.032	0.026	0.053	0.038	0.045	0.088	0.062	0.044
V	0	0	0	0	0	0	0	0	0	0	0	0	0	0	0
Cr	0	0	0.004	0.002	0.003	0	0	0.01	0.007	0.008	0	0	0	0	0.01
Fe3	0.15	0.291	0.105	0.503	0	0.534	0	0	0	0	0	0	0	0	0
Fe2	0.278	0.177	0.315	0.122	0.367	0.122	0.471	0.281	0.306	0.289	1.552	1.284	0.769	1.429	0.324
Ni	0.001	0	0	0.002	0.002	0	0.001	0.005	0	0	0	0.001	0.007	0.001	0.001
Mg	0.773	0.803	0.862	0.774	0.86	0.777	0.837	0.882	0.904	0.845	0.001	0.005	0.008	0.011	0.901
Ca	0.731	0.711	0.701	0.735	0.691	0.701	0.584	0.749	0.718	0.754	0.005	0.007	0.011	0.009	0.677
Mn	0.015	0.017	0.01	0.013	0.009	0.013	0.007	0.008	0.007	0.009	0	0.009	0.015	0.005	0.007
Na	0.056	0.067	0.009	0.037	0.013	0.058	0.012	0.014	0.014	0.015	0.005	0.004	0.005	0.004	0.015

K	0	0.001	0	0	0	0.001	0	0	0	0	0.002	0.002	0.002	0	0
P	0.001	0.001	0	0	0	0.001	0	0	0	0.002	0	0	0	0	0
Zn	0.001	0.001	0	0.005	0	0	0.004	0	0	0	0.003	0.008	0.001	0	0
Co	0	0	0	0	0	0	0	0	0	0	0	0	0	0	0
Ba	0	0	0	0	0	0	0	0	0	0	0	0	0.001	0	0
O_calc	5.925	5.855	5.947	5.748	6.017	5.733	6.05	6.013	6.009	6.024	6.409	6.653	7.133	6.508	6.024
Mg#	73.541	81.898	73.231	86.386	70.059	86.461	63.999	75.85	74.709	74.498	0.093	0.369	1.064	0.747	73.587
Wo	41.039	42.03	37.325	45.07	36.026	43.847	30.863	39.182	37.231	39.934	0.333	0.566	1.445	0.633	35.599
En	43.361	47.476	45.898	47.452	44.819	48.55	44.247	46.131	46.894	44.748	0.093	0.367	1.049	0.742	47.391
Fs	15.601	10.493	16.777	7.478	19.155	7.603	24.89	14.687	15.875	15.318	99.575	99.067	97.507	98.625	17.011

GUN 1.1 Pyroxene (contd.)

	47	48	49	50
SiO2	38.43	54.03	51.37	41.85
TiO2	0.56	0.56	1.02	0.68
Al2O3	1.46	0.99	1.63	1.63
V2O3	0	0	0	0
Cr2O3	0	0.02	0	0
Fe2O3	0	0	0	0
FeO	22.7	20.91	16.21	22.61
NiO	0.08	0.04	0.05	0
MgO	17.61	16.53	14.56	19.87
CaO	5.55	3.88	13.34	5.29
MnO	0.37	0.46	0.38	0.5
Na2O	0.46	0.16	0.16	0.19
K2O	0	0.05	0	0
P2O5	0	0	0	0.03
ZnO	0.04	0.01	0	0.22
CoO	0	0	0	0
BaO	0	0	0.03	0.02
Si	1.652	2.104	1.97	1.683
Ti	0.018	0.016	0.029	0.021
Al(IV)	0.074	0	0.03	0.077
Al(VI)	0	0.045	0.044	0
V	0	0	0	0
Cr	0	0.001	0	0
Fe3	0.624	0	0	0.527
Fe2	0.192	0.681	0.52	0.233
Ni	0.003	0.001	0.002	0
Mg	1.128	0.96	0.832	1.191
Ca	0.256	0.162	0.548	0.228
Mn	0.013	0.015	0.012	0.017

Na	0.038	0.012	0.012	0.015
K	0	0.002	0	0
P	0	0	0	0.001
Zn	0.001	0	0	0.007
Co	0	0	0	0
Ba	0	0	0	0
O_calc	5.688	6.136	6.03	5.736
Mg#	85.474	58.492	61.555	83.643
Wo	16.22	8.981	28.842	13.796
En	71.61	53.239	43.801	72.104
Fs	12.17	37.78	27.356	14.1

Table 8: Mineral chemistry (wt%), stoichiometry (on the basis 6 oxygens) and composition of pyroxenes

GUN 2 Pyroxene											
	11	12	13	14	21	22	23	34	51	52	53
SiO2	53.2	49.89	49.9	51.71	51.19	53.46	51.76	51.58	48.33	50.96	51.09
TiO2	1.09	1.79	0.96	0.61	0.64	1.01	0.67	0.69	1.48	0.6	0.72
Al2O3	3.18	3.52	2.35	2.71	2.57	2.21	2.95	2.58	2.56	2.63	2.45
V2O3	0	0	0	0	0	0	0	0	0	0	0
Cr2O3	0.11	0.04	0.12	0	0.11	0.22	0.01	0	0.06	0.02	0.24
Fe2O3	0	0	0	0	0	0	0	0	0	0	0
FeO	8.68	11.54	8.41	5.27	5.34	8.96	5.31	5.69	10.4	5.26	6.64
NiO	0	0	0	0	0	0	0	0	0.04	0.08	0
MgO	15.15	14.1	16.43	17.15	17.04	15.73	17.08	16.94	16.68	17.03	16.23
CaO	16.6	16.57	20.07	21.64	21.39	18.47	21.73	21.2	19.7	21.43	20.47
MnO	0.41	0.42	0.45	0.42	0.4	0.41	0.46	0.52	0.4	0.45	0.48
Na2O	0.53	0.79	0.56	0.45	0.5	0.5	0.48	0.52	0.57	0.43	0.52
K2O	0.12	0.36	0	0	0.01	0	0	0	0.01	0	0
P2O5	0.01	0.09	0	0.06	0.05	0	0.01	0.02	0	0.03	0.04
ZnO	0	0	0	0	0	0.04	0	0.08	0	0	0
CoO	0	0	0	0	0	0	0	0	0	0	0
BaO	0.02	0.02	0	0.01	0	0.05	0.05	0	0	0	0
Si	1.988	1.878	1.848	1.884	1.88	1.96	1.877	1.886	1.779	1.877	1.895
Ti	0.031	0.051	0.027	0.017	0.018	0.028	0.018	0.019	0.041	0.017	0.02
Al(IV)	0.012	0.122	0.103	0.116	0.111	0.04	0.123	0.111	0.111	0.114	0.105
Al(VI)	0.128	0.034	0	0	0	0.056	0.003	0	0	0	0.002
V	0	0	0	0	0	0	0	0	0	0	0
Cr	0.003	0.001	0.004	0	0.003	0.006	0	0	0.002	0.001	0.007
Fe3	0	0.052	0.184	0.109	0.122	0	0.115	0.114	0.288	0.125	0.089
Fe2	0.271	0.311	0.077	0.052	0.042	0.275	0.046	0.06	0.032	0.037	0.117
Ni	0	0	0	0	0	0	0	0	0.001	0.002	0
Mg	0.844	0.791	0.907	0.931	0.933	0.86	0.924	0.923	0.915	0.935	0.897
Ca	0.665	0.668	0.797	0.845	0.842	0.726	0.844	0.831	0.777	0.846	0.814

Mn	0.013	0.013	0.014	0.013	0.012	0.013	0.014	0.016	0.012	0.014	0.015
Na	0.038	0.058	0.04	0.032	0.036	0.036	0.034	0.037	0.041	0.031	0.037
K	0.006	0.017	0	0	0	0	0	0	0	0	0
P	0	0.003	0	0.002	0.002	0	0	0.001	0	0.001	0.001
Zn	0	0	0	0	0	0.001	0	0.002	0	0	0
Co	0	0	0	0	0	0	0	0	0	0	0
Ba	0	0	0	0	0	0.001	0.001	0	0	0	0
O_calc	6.069	5.974	5.908	5.945	5.939	6.021	5.942	5.943	5.856	5.937	5.955
Mg#	75.677	71.764	92.197	94.76	95.731	75.784	95.262	93.869	96.643	96.206	88.482
Wo	37.341	37.738	44.734	46.218	46.342	39.007	46.554	45.779	45.065	46.526	44.508
En	47.418	44.682	50.954	50.964	51.367	46.223	50.914	50.897	53.091	51.445	49.101
Fs	15.241	17.58	4.313	2.818	2.291	14.77	2.532	3.325	1.844	2.029	6.391

Table 9: Mineral chemistry (wt%), stoichiometry (on the basis 6 oxygens) and composition of pyroxenes

GUN C1 Pyroxene (Cognate)													
	1	2	4	14	15	28	29	31	34	35	43	51	3
SiO2	51.64	51.93	51.62	50.52	51.86	51.41	50.81	52.88	51.38	51.06	51.76	51.49	51.57
TiO2	0.89	0.88	0.9	0.92	0.9	0.75	1.11	0.75	0.92	0.8	0.77	0.84	0.52
Al2O3	2.23	2.06	2.37	2.18	2.53	1.6	1.33	1.72	2.11	1.83	1.68	2.03	0.59
V2O3	0	0	0	0	0	0	0	0	0	0	0	0	0
Cr2O3	0.18	0.21	0.25	0.11	0.14	0.09	0	0.15	0.25	0.26	0.15	0.17	0
Fe2O3	0	0	0	0	0	0	0	0	0	0	0	0	0
FeO	9.9	10.64	10.52	10.22	10.36	11.67	15.26	10.33	10.23	10.74	10.16	10.09	24.89
NiO	0.03	0.02	0.05	0.05	0.02	0	0	0.03	0.08	0.14	0.02	0.05	0.07
MgO	15.01	15.76	15.44	14.82	15.5	14.88	13.26	16.15	15.58	14.99	15.83	15.57	15.82
CaO	18.76	17.37	17.73	18.09	17.9	17.88	16.31	18.29	18.01	17.48	18.21	18.52	5.11
MnO	0.22	0.11	0.25	0.24	0.16	0.24	0.33	0.26	0.19	0.28	0.2	0.19	0.47
Na2O	0.25	0.21	0.26	0.22	0.26	0.22	0.28	0.21	0.26	0.21	0.24	0.24	0.05
K2O	0	0.01	0	0.01	0	0	0.01	0	0.02	0	0	0	0.01
P2O5	0.01	0	0	0.01	0.05	0	0	0	0	0	0.03	0	0
ZnO	0	0	0.09	0	0.09	0	0.04	0	0.09	0	0	0.02	0
CoO	0	0	0	0	0	0	0	0	0	0	0	0	0
BaO	0	0.03	0	0	0	0	0	0	0	0	0	0	0
Si	1.939	1.946	1.931	1.932	1.932	1.946	1.953	1.949	1.927	1.948	1.94	1.928	2.001
Ti	0.025	0.025	0.025	0.026	0.025	0.021	0.032	0.021	0.026	0.023	0.022	0.024	0.015
Al(IV)	0.061	0.054	0.069	0.068	0.068	0.054	0.047	0.051	0.073	0.052	0.06	0.072	0
Al(VI)	0.037	0.037	0.036	0.031	0.044	0.018	0.013	0.023	0.02	0.03	0.014	0.018	0.027
V	0	0	0	0	0	0	0	0	0	0	0	0	0
Cr	0.005	0.006	0.007	0.003	0.004	0.003	0	0.004	0.007	0.008	0.004	0.005	0
Fe3	0	0	0	0	0	0.007	0	0	0.013	0	0.012	0.019	0
Fe2	0.311	0.333	0.329	0.327	0.323	0.363	0.49	0.318	0.307	0.343	0.306	0.297	0.808
Ni	0.001	0.001	0.002	0.002	0.001	0	0	0.001	0.002	0.004	0.001	0.002	0.002
Mg	0.84	0.881	0.861	0.845	0.861	0.84	0.76	0.887	0.871	0.853	0.885	0.869	0.915

Ca	0.755	0.697	0.711	0.741	0.715	0.725	0.672	0.722	0.724	0.715	0.731	0.743	0.212
Mn	0.007	0.003	0.008	0.008	0.005	0.008	0.011	0.008	0.006	0.009	0.006	0.006	0.015
Na	0.018	0.015	0.019	0.016	0.019	0.016	0.021	0.015	0.019	0.016	0.017	0.017	0.004
K	0	0	0	0	0	0	0	0	0.001	0	0	0	0
P	0	0	0	0	0.002	0	0	0	0	0	0.001	0	0
Zn	0	0	0.002	0	0.002	0	0.001	0	0.002	0	0	0.001	0
Co	0	0	0	0	0	0	0	0	0	0	0	0	0
Ba	0	0	0	0	0	0	0	0	0	0	0	0	0
O_calc	6.007	6.012	6.003	6.002	6.008	5.997	6.004	6.001	5.993	6.008	5.994	5.99	6.027
Mg#	72.993	72.53	72.347	72.106	72.73	69.842	60.768	73.593	73.91	71.33	74.295	74.555	53.118
Wo	39.601	36.489	37.386	38.747	37.642	37.623	34.947	37.461	38.044	37.414	38.051	38.926	10.978
En	44.087	46.065	45.3	44.167	45.353	43.565	39.532	46.025	45.792	44.643	46.025	45.534	47.287
Fs	16.312	17.446	17.315	17.086	17.005	18.811	25.521	16.514	16.165	17.943	15.924	15.54	41.736

Table 10: Mineral chemistry (wt%), stoichiometry (on the basis 6 oxygens) and composition of pyroxenes

GUN C1 Pyroxene (Matrix)								
	6	7	12	13	36	58	59	62
SiO2	51.32	51.65	51.71	50.33	51.3	51.26	50.57	45.93
TiO2	0.83	0.82	0.67	0.81	0.74	0.89	0.83	0.03
Al2O3	2.09	1.27	1.6	1.2	1.27	2.68	1.1	6.11
V2O3	0	0	0	0	0	0	0	0
Cr2O3	0.18	0	0.23	0.01	0.06	0.48	0.05	0
Fe2O3	0	0	0	0	0	0	0	0
FeO	10.73	18.28	10.51	18.08	16.8	9.4	21.1	19.64
NiO	0.05	0.09	0.03	0	0.05	0	0.02	0
MgO	15.24	12.74	15.28	12.01	13.12	14.88	10.22	16.35
CaO	17.71	15.27	18.1	16.08	15.65	19.33	15.76	1.95
MnO	0.2	0.36	0.26	0.38	0.41	0.27	0.4	0
Na2O	0.15	0.25	0.16	0.22	0.19	0.26	0.16	0.24
K2O	0.01	0	0	0.01	0	0.02	0	0.49
P2O5	0	0.04	0	0.03	0.06	0	0	0.03
ZnO	0	0.1	0	0.05	0	0	0.25	0.05
CoO	0	0	0	0	0	0	0	0
BaO	0.01	0	0	0.02	0	0.02	0.02	0
Si	1.941	1.961	1.955	1.946	1.962	1.916	1.961	1.89
Ti	0.024	0.023	0.019	0.024	0.021	0.025	0.024	0.001
Al(IV)	0.059	0.039	0.045	0.054	0.038	0.084	0.039	0.11
Al(VI)	0.035	0.017	0.026	0.001	0.019	0.035	0.011	0.187
V	0	0	0	0	0	0	0	0
Cr	0.005	0	0.007	0	0.002	0.014	0.002	0
Fe3	0	0	0	0.02	0	0.004	0	0
Fe2	0.339	0.58	0.332	0.565	0.537	0.289	0.684	0.676
Ni	0.002	0.003	0.001	0	0.002	0	0.001	0

Mg	0.859	0.721	0.861	0.692	0.748	0.829	0.591	1.003
Ca	0.718	0.621	0.733	0.666	0.641	0.774	0.655	0.086
Mn	0.006	0.012	0.008	0.012	0.013	0.009	0.013	0
Na	0.011	0.018	0.012	0.016	0.014	0.019	0.012	0.019
K	0	0	0	0	0	0.001	0	0.026
P	0	0.001	0	0.001	0.002	0	0	0.001
Zn	0	0.003	0	0.001	0	0	0.007	0.002
Co	0	0	0	0	0	0	0	0
Ba	0	0	0	0	0	0	0	0
O_calc	6.009	6.005	6.007	5.99	6.009	5.998	6.005	6.018
Mg#	71.686	55.404	72.157	55.061	58.196	74.131	46.335	59.742
Wo	37.45	32.307	38.054	34.633	33.285	40.902	33.929	4.871
En	44.84	37.504	44.699	35.992	38.826	43.81	30.614	56.832
Fs	17.71	30.188	17.247	29.375	27.89	15.288	35.457	38.297

Table 11: Mineral chemistry (wt%), stoichiometry (6 oxygens) and composition of Spinel

Spinel (All Samples)										
	GUN1.1_19	GUN1.1_21	GUN1.1_41	GUN2_15	GUN2_16	GUN2_17	GUN2_27	GUN2_29	GUN2_41	GUN2_42
SiO2	0.03	0.04	0.01	0.01	0.07	0.02	0.01	0.02	0	0.06
TiO2	5.36	4.43	4.1	9.78	8.24	10.33	10.01	10.63	10.05	10.05
Al2O3	0.74	0.62	0.66	0.59	0.93	0.99	0.58	0.91	0.69	0.65
V2O3	0	0	0	0	0	0	0	0	0	0
Cr2O3	0.02	0	0	0	0.07	0.04	0	0	0	0.02
Fe2O3	0	0	0	0	0	0	0	0	0	0
FeO	81.1	81.98	80.89	73.96	77.39	73.67	74.96	73.26	74.02	74.62
NiO	0.04	0.13	0.04	0.05	0	0.1	0.09	0	0.04	0
MgO	1.97	2.11	2.01	4.01	3.36	4.46	4.16	4.18	4.18	4.03
CaO	0.07	0.05	0.04	0.08	0.05	0.05	0.07	0.52	0.03	0.02
MnO	0.37	0.31	0.79	0.54	0.34	0.43	0.5	0.49	0.51	0.59
Na2O	0.02	0	0	0.03	0.03	0.05	0	0	0	0.01
K2O	0	0	0	0	0.01	0	0	0.01	0	0
P2O5	0	0	0.02	0	0	0	0.01	0.38	0.01	0
ZnO	0	0	0	0.18	0	0	0.11	0	0.05	0
CoO	0	0	0	0	0	0	0	0	0	0
BaO	0	0	0	0	0.02	0	0	0	0	0
Si	0.009	0.013	0.003	0.003	0.022	0.006	0.003	0.006	0	0.019
Ti	1.271	1.049	0.983	2.303	1.918	2.396	2.324	2.464	2.355	2.346
Al	0.275	0.23	0.248	0.218	0.339	0.36	0.211	0.33	0.253	0.238

V	0	0	0	0	0	0	0	0	0	0
Cr	0.005	0	0	0	0.017	0.01	0	0	0	0.005
Fe3	13.172	13.646	13.763	11.188	11.786	10.856	11.127	10.436	11.029	11.035
Fe2	8.198	7.939	7.805	8.174	8.238	8.139	8.217	8.441	8.253	8.327
Ni	0.01	0.033	0.01	0.013	0	0.025	0.022	0	0.01	0
Mg	0.925	0.99	0.955	1.871	1.55	2.05	1.914	1.92	1.941	1.864
Ca	0.024	0.017	0.014	0.027	0.017	0.017	0.023	0.172	0.01	0.007
Mn	0.099	0.083	0.213	0.143	0.089	0.112	0.131	0.128	0.135	0.155
Na	0.012	0	0	0.018	0.018	0.03	0	0	0	0.006
K	0	0	0	0	0.004	0	0	0.004	0	0
P	0	0	0.005	0	0	0	0.003	0.099	0.003	0
Zn	0	0	0	0.042	0	0	0.025	0	0.011	0
Co	0	0	0	0	0	0	0	0	0	0
Ba	0	0	0	0	0.002	0	0	0	0	0
O_calc	25.414	25.177	25.119	26.406	26.107	26.572	26.436	26.782	26.486	26.483
Mg#	10.143	11.091	10.905	18.628	15.834	20.119	18.89	18.531	19.04	18.291

Spinel (All Samples) (contd.)								
	GUN2_44	GUN6_14	GUN6_22	GUN6_41	GUN6_56	GUNC1_20	GUNC1_23	GUNC1_55
SiO2	0.05	0.05	8.7	0.1	0.04	0.12	0.44	0.25
TiO2	8	5.64	3.86	5.19	13.83	8.37	8.77	0.16
Al2O3	1.05	0.64	3.06	0.63	0.79	2.31	1.78	0.07
V2O3	0	0	0	0	0	0	0	0
Cr2O3	0.03	0	0.03	0.03	0	0.03	0	0.02
Fe2O3	0	0	0	0	0	0	0	0
FeO	76.99	78.72	69.02	79.48	71.87	80.42	79.76	87.95
NiO	0.09	0.2	0.04	0.05	0.02	0.05	0.05	0.18
MgO	3.59	2.66	1.33	2.3	2.1	0.21	0.29	0.03
CaO	0.17	0.07	0.97	0.66	0.18	0.04	0.04	0.07
MnO	0.39	0.6	0.48	0.57	0.49	0.17	0.24	0
Na2O	0	0.02	0.1	0.06	0	0.02	0	0
K2O	0.02	0	0.07	0	0	0	0	0.01
P2O5	0	0	0.02	0.25	0	0	0.05	0

ZnO	0.06	0	0.04	0	0.02	0.16	0.17	0.08
CoO	0	0	0	0	0	0	0	0
BaO	0	0	0	0	0	0	0	0
Si	0.015	0.016	2.721	0.031	0.013	0.037	0.138	0.081
Ti	1.858	1.346	0.908	1.229	3.318	1.96	2.064	0.039
Al	0.382	0.239	1.128	0.234	0.297	0.847	0.656	0.027
V	0	0	0	0	0	0	0	0
Cr	0.007	0	0.007	0.007	0	0.007	0	0.005
Fe3	11.871	13.048	7.68	13.074	9.041	11.163	10.901	15.733
Fe2	8.011	7.843	10.371	7.854	10.129	9.768	9.964	8.007
Ni	0.022	0.051	0.01	0.013	0.005	0.013	0.013	0.047
Mg	1.653	1.258	0.62	1.08	0.998	0.097	0.135	0.014
Ca	0.056	0.024	0.325	0.223	0.062	0.013	0.013	0.024
Mn	0.102	0.161	0.127	0.152	0.132	0.045	0.064	0
Na	0	0.012	0.061	0.037	0	0.012	0	0
K	0.008	0	0.028	0	0	0	0	0.004
P	0	0	0.005	0.067	0	0	0.013	0
Zn	0.014	0	0.009	0	0.005	0.037	0.039	0.019
Co	0	0	0	0	0	0	0	0
Ba	0	0	0	0	0	0	0	0
O_calc	26.065	25.476	28.16	25.463	27.48	26.418	26.549	24.133
Mg#	17.101	13.826	5.641	12.084	8.973	0.988	1.339	0.18

Table 12: Mineral chemistry (wt%), stoichiometry (6 oxygens) and composition of ilmenites

Ilmenite (All Samples)											
DataSet/Point	GUN2_28	GUN2_30	GUN2_43	GUN2_45	GUN2_46	GUN6_9	GUN6_38	GUN6_39	GUN6_38	GUN6_39	GUN6_53
SiO2	0.1	0.05	0.15	0.09	0.13	0	0.1	0.39	0.1	0.39	0.1
TiO2	37.86	38.96	37.96	37.92	38.01	36.91	16.99	37.82	16.99	37.82	34.91
Al2O3	1.09	1.33	1.18	1.26	1.29	1.22	1.57	1.14	1.57	1.14	1.28
MgO	2.7	2.66	2.71	2.67	2.51	2.31	2.05	2.45	2.05	2.45	2.49
CaO	0.1	0.11	0.14	0.05	0.09	0.07	0.06	0.24	0.06	0.24	0.07
FeO	49.21	49.1	48.66	48.81	48.82	49.96	68.05	48.56	68.05	48.56	52.13
MnO	0.21	0.17	0.11	0.16	0.2	0.44	0.42	0.29	0.42	0.29	0.49

Na2O	0	0	0.01	0	0.04	0	0.04	0	0.04	0	0
K2O	0.06	0	0	0.06	0.04	0	0	0	0	0	0.02
P2O5	0	0.03	0.04	0.01	0.03	0	0	0	0	0	0
NiO	0	0	0.03	0	0.02	0.03	0	0	0	0	0.04
Cr2O3	0.03	0	0	0	0	0	0.05	0.08	0.05	0.08	0
V2O3	0	0	0	0	0	0	0	0	0	0	0
Total	91.36	92.41	90.99	91.03	91.18	90.94	89.33	90.97	89.33	90.97	91.53
Si	0.002642	0.001307	0.003978	0.002386	0.003443	0	0.002649	0.010363	0.002649	0.010363	0.002632
Ti	0.755013	0.768687	0.759814	0.758774	0.759821	0.741263	0.339678	0.758416	0.339678	0.758416	0.693455
Al	0.034068	0.041127	0.037018	0.039515	0.040416	0.0384	0.049195	0.035829	0.049195	0.035829	0.03985
Mg	0.106753	0.104053	0.107546	0.105925	0.099478	0.091978	0.081259	0.097408	0.081259	0.097408	0.098064
Ca	0.002841	0.003092	0.003993	0.001425	0.002563	0.002003	0.001709	0.006857	0.001709	0.006857	0.001981
Fe	1.091307	1.077289	1.083112	1.086107	1.085254	1.115759	1.51294	1.082891	1.51294	1.082891	1.151532
Mn	0.004717	0.003778	0.00248	0.003606	0.004503	0.009953	0.009458	0.00655	0.009458	0.00655	0.010963
Na	0	0	0.000516	0	0.002062	0	0.002062	0	0.002062	0	0
K	0.00203	0	0	0.002037	0.001356	0	0	0	0	0	0.000674
P	0	0.000666	0.000901	0.000225	0.000675	0	0	0	0	0	0
Ni	0	0	0.000642	0	0.000428	0.000644	0	0	0	0	0.00085
Cr	0.000629	0	0	0	0	0	0.001051	0.001687	0.001051	0.001687	0
V	0	0	0	0	0	0	0	0	0	0	0
Total(S)	2	2	2	2	2	2	2	2	2	2	2
Fe3+ : 2X (1-T/S)	0.452022	0.416885	0.432693	0.439526	0.432386	0.479074	1.2651	0.424927	1.2651	0.424927	0.568651
Fe2+ : nomalized FeO- Fe3+	0.639285	0.660404	0.650419	0.646581	0.652868	0.636685	0.24784	0.657964	0.24784	0.657964	0.582881
Fe2+ + Fe 3+	1.091307	1.077289	1.083112	1.086107	1.085254	1.115759	1.51294	1.082891	1.51294	1.082891	1.151532
FeO+FE2O3+TiO2	89.33862	90.17476	88.78358	88.92845	88.99488	89.25753	91.37325	88.50082	91.37325	88.50082	89.90518

FEO%	32.26721	33.37906	32.91239	32.67521	33.00099	31.93977	12.19996	33.33872	12.19996	33.33872	29.34994
Fe2O3	25.3547	23.41594	24.33196	24.68377	24.28869	26.70798	69.20598	23.92721	69.20598	23.92721	31.82027
TiO2%	42.37809	43.205	42.75565	42.64102	42.71032	41.35225	18.59406	42.73407	18.59406	42.73407	38.8298

Ilmenite (All Samples) (contd.)											
DataSet/Point	GUN6_55.	GUN6_57	GUN6_58	GUN6_59	GUNC1_21	GUNC1_22	GUNC1_27	GUNC1_40	GUNC1_48	GUNC1_54	GUNC1_56
SiO2	0.18	6.51	0.04	0.16	0.04	0	0.04	0.06	0.01	0.15	0
TiO2	34.95	35.27	37.26	37.15	49.71	49.66	48.41	50.16	49.33	49.47	48.89
Al2O3	1.29	2.59	1.02	1.25	0.09	0.1	0.1	0.02	0.03	0.06	0.05
MgO	2.22	2.63	2.46	2.32	0.99	0.61	1.82	0.89	0.7	2.67	
CaO	0.1	0.31	0.1	0.07	0	0.09	0.13	0.02	0.06	0.11	
FeO	50.58	44.61	49.98	50.19	46.06	46.17	44.38	46.2	46.64	43.14	45.88
MnO	0.37	0.26	0.29	0.45	0.53	0.66	0.41	0.67	0.45	0.45	0.46
Na2O	0	0.22	0.05	0	0.06	0	0	0	0	0	0.04
K2O	0.01	0.75	0.04	0.04	0	0.01	0	0	0	0.03	0.01
P2O5	0	0	0	0	0	0.02	0	0.02	0.01	0	0.03
NiO	0.07	0.05	0	0	0.08	0.01	0.11	0.06	0	0	0.08
Cr2O3	0	0	0	0.02	0.06	0	0.07	0	0	0.15	0
V2O3	0	0	0	0	0	0	0	0	0	0	0
Total	89.77	93.2	91.24	91.65	97.62	97.33	95.47	98.1	97.23	96.23	95.44
Si	0.004842	0.163674	0.00106	0.004222	0.001019	0	0.001035	0.001525	0.000257	0.003826	0
Ti	0.709575	0.669227	0.744943	0.739822	0.956075	0.961558	0.945336	0.962012	0.955571	0.952244	0.970557
Al	0.041048	0.077022	0.031962	0.039014	0.002713	0.003035	0.003061	0.000601	0.000911	0.00181	0.001556
Mg	0.089361	0.098939	0.097512	0.091601	0.037751	0.023417	0.070463	0.033842	0.026884	0.101897	0
Ca	0.002893	0.00838	0.002849	0.001986	0	0.002483	0.003617	0.000547	0.001656	0.003017	0
Fe	1.141957	0.941283	1.111211	1.111491	0.985127	0.994142	0.963736	0.985338	1.004686	0.923435	1.012849
Mn	0.008461	0.005556	0.00653	0.010093	0.011481	0.014394	0.009018	0.014473	0.009818	0.009756	0.010285
Na	0	0.010763	0.002577	0	0.002975	0	0	0	0	0	0.002047

K	0.000344	0.024141	0.001357	0.001351	0	0.000328	0	0	0	0.00098	0.000337
P	0	0	0	0	0	0.000436	0	0.000432	0.000218	0	0.00067
Ni	0.00152	0.001015	0	0	0.001646	0.000207	0.002297	0.001231	0	0	0.001698
Cr	0	0	0	0.000419	0.001213	0	0.001437	0	0	0.003036	0
V	0	0	0	0	0	0	0	0	0	0	0
Total(S)	2	2	2	2	2	2	2	2	2	2	2
Fe3+ : 2X (1-T/S)	0.530463	0.281317	0.477389	0.473829	0.081885	0.072871	0.102761	0.071029	0.08678	0.083994	0.055655
Fe2+ : nomalized FeO- Fe3+	0.611494	0.659966	0.633822	0.637662	0.903242	0.921272	0.860975	0.914309	0.917906	0.839441	0.957194
Fe2+ + Fe 3+	1.141957	0.941283	1.111211	1.111491	0.985127	0.994142	0.963736	0.985338	1.004686	0.923435	1.012849
FeO+FE2O3+TiO2	88.14504	81.3639	89.62983	89.72138	96.19612	96.20667	93.31669	96.73067	96.41838	93.04673	95.05059
FEO%	30.72725	38.44163	31.80637	32.09266	43.90139	44.47274	42.48743	44.31855	44.19433	42.14663	45.61669
Fe2O3	29.6222	18.20991	26.62265	26.50138	4.422924	3.909213	5.635457	3.826123	4.643221	4.686538	2.947541
TiO2%	39.65056	43.34847	41.57098	41.40596	51.67568	51.61804	51.87711	51.85532	51.16245	53.16683	51.43576

Table 13: Major oxide (wt%) and CIPW norms of the samples from Gunjale lava tube.

XRF						
Sample	GUN-01 IG	GUN-02 IG	GUN-04 IG	GUN-05 IG	GUN-06 IG	GUN-01
Rock type	B, subal	B, subal	B, subal	B, subal	B, subal	B, subal
SiO2	45.783	47.684	48.98	48.414	46.283	46.103
TiO2	2.18	2.289	2.384	2.374	2.41	2.195
Al2O3	12.311	13.794	13.506	13.361	14.811	12.425
FeOT	14.484	14.465	14.657	14.696	14.984	14.731
MnO	0.288	0.215	0.202	0.21	0.222	0.3
MgO	5.378	5.169	5.182	5.23	4.751	5.416
CaO	11.204	9.225	9.045	9.166	11.567	11.317
Na2O	2.111	2.143	2.196	2.163	2.437	2.099
K2O	0.541	0.918	1.183	1.147	0.711	0.545
P2O5	0.208	0.215	0.243	0.232	0.241	0.213
Total	100.004	98.685	100.205	100.602	100.048	96.889
SiO2adj	48.328	49.484	50.068	49.787	46.906	48.228

TiO2adj	2.301	2.375	2.437	2.441	2.442	2.296
Al2O3adj	12.995	14.315	13.806	13.74	15.01	12.998
Fe2O3adj	2.591	2.544	2.54	2.562	2.574	2.612
FeOadj	12.957	12.722	12.698	12.808	12.87	13.06
MnOadj	0.304	0.223	0.206	0.216	0.225	0.314
MgOadj	5.677	5.364	5.297	5.378	4.815	5.666
CaOadj	11.827	9.573	9.246	9.426	11.723	11.838
Na2Oadj	2.228	2.224	2.245	2.224	2.47	2.196
K2Oadj	0.571	0.953	1.209	1.18	0.72	0.57
P2O5adj	0.22	0.223	0.248	0.238	0.244	0.223
Q	-	1.206	1.736	1.272	-	-
Or	3.374	5.632	7.145	6.973	4.255	3.368
Ab	18.853	18.819	18.996	18.819	20.9	18.582
An	23.77	26.262	24.022	24.022	27.742	23.925
C	-	-	-	-	-	-
Di	27.938	16.518	16.899	17.697	24.172	27.849
Hy	14.098	22.847	22.315	22.315	3.12	14.206
Ol	3.329	-	-	-	10.875	3.405
Mt	3.756	3.688	3.682	3.714	3.732	3.787
Il	4.37	4.511	4.629	4.636	4.638	4.361
Ap	0.51	0.517	0.574	0.551	0.565	0.517
Mg#	43.852	42.909	42.647	42.807	40.008	43.609
FeOT/MgO	2.693	2.798	2.829	2.81	3.154	2.72
Salic	45.997	51.919	51.899	51.086	52.897	45.875
Femic	38.637	38.7	38.445	38.871	32.873	38.713
CI	57.651	49.648	47.594	48.444	55.399	57.548
DI	22.227	25.657	27.877	27.064	25.155	21.95
SI	23.63	22.531	22.081	22.267	20.534	23.506
AR	1.254	1.307	1.352	1.344	1.271	1.251